Design, Comparison and Experimental Evaluation of Non-Overlap Winding Radial Flux Permanent Magnet Hub Drives for Electric Vehicles

by

Arnold Johan Rix

Dissertation presented for the degree of Doctor of Philosophy in the Faculty of Engineering at Stellenbosch University

Promotor: Prof. M.J. Kamper

Department of Electrical & Electronic Engineering

March 2011

DECLARATION

By submitting this dissertation electronically, I declare that the entirety of the work contained therein is my own, original work, that I am the sole author thereof (save to the extent explicitly otherwise stated), that reproduction and publication thereof by Stellenbosch University will not infringe any third party rights and that I have not previously in its entirety or in part submitted it for obtaining any qualification.

Date: March 2011

ABSTRACT

The focus of this thesis is on the optimal design, control and evaluation of 3-phase permanent magnet radial flux synchronous machines with non-overlapping, concentrated-coil, double layer stator windings for EV hub drive applications.

A simple analytical method is developed that can be used as a first design tool. The method uses and predicts the MMF harmonic content for a certain pole-slot combination as well as the harmonic content for the air gap permeance function. These harmonics are then used to calculate the torque and torque ripple of machines with large stator slot openings and surface mounted permanent magnets.

A different approach to calculate the iron, stator copper eddy current and magnet losses is presented. This method specifically looks at the machine during field weakening operation when the flux paths are changing in the machine. Flux density information throughout the machine is extracted from a series of static FE solutions, to calculate the losses and to combine this with an empirical formula.

Some machine topology choices are compared for use as hub drives in small electric vehicles. The parameters that influence the machine design are discussed and evaluated after a multidimensional design optimization is done and an efficient control algorithm is implemented. The algorithm works through the entire operating speed range and make use of, automatically generated, 2D look up tables to determine the correct current reference.

A stator lamination design is proposed, that combines the use of rectangular preformed coils and semi-closed stator slots. Two prototype machines, one with a good winding factor and the other with a low winding factor, are built and compared. The manufacturing and testing of the two prototype machines are described and shown in detail.

UITTREKSEL

Die fokus van hierdie tesis is op die optimale ontwerp, beheer en evaluasie van 3-fase permanent magneet radiale vloed sinchroon masjiene met nie-oorvleuelende, gekonsentreerde, dubbel laag stator wikkelinge vir EV hub motor toepassings.

'n Eenvoudige analitiese metode is ontwikkel wat as 'n eerste ontwerp gereedskap stuk gebruik kan word. Die metode gebruik en voorspel die MMF se frekwensie inhoud vir 'n sekere pool-gleuf kombinasie sowel as die frekwensie inhoud vir die lug spleet permeansie funksie. Hierdie frekwensie inhoud word dan gebruik om die draaimoment en draaimoment riffel van masjiene met groot stator gleuf openinge en oppervlak magnete te voorspel.

'n Ander benadering om yster, stator koper werwel stroom en magneet verliese te bepaal word voorgestel. Hierdie metode kyk spesifiek na masjiene onder veld verswakking beheer wanneer die vloed paaie verander vanaf die normale. Die vloeddigtheid, regdeur die masjien, word verkry deur om van 'n reeks statiese eindige element oplossings gebruik te maak en dit te kombineer met 'n empiriese verliesberekening.

Die parameters wat die masjienontwerp beïnvloed, word bespreek en geëvalueer na 'n multidimensionele ontwerp optimering gedoen is en 'n effektiewe beheer algoritme geïmplimenteer is. Die algoritme werk vir enige spoed en is gebaseer op die outomaties gegenereerde 2D opsoek tabelle wat die korrekte stroomverwysing gee.

'n Stator laminasie ontwerp word voorgestel wat die gebruik van vooraf vervaardigde spoele en gedeeltelik toe stator gleuwe moontlik maak. Twee prototipe masjiene, een met 'n goeie windingsfaktor en een met 'n swakker windingsfaktor is gebou en vergelyk. Die vervaardiging en toetsing van die twee prototipe masjiene word in detail beskryf en gewys.

ACKNOWLEDGMENTS

I would like to express my sincere appreciation to:

- My promoter Prof. M.J. Kamper for his supervision and constant encouragement and his efforts to ensure the availability of financial resources.
- Dr. R-J Wang for his assistance and willingness to listen while sharing an office with me.
- Dr. H.W. de Kock who worked with me on the torque control algorithm.
- SANERI for providing financial assistance.
- All the people of the electrical workshop for the help assembling and setting up the prototypes for testing.
- My family for their interest by always inquiring how the work is progressing
- My wife, Christa, for her understanding and encouragement the past 10 years.
- The Lord, for blessing me with this wonderful opportunity.

LIST OF PUBLICATIONS

National conference

- Rix, A., Kamper, M. and Wang, R.-J.: Torque ripple and flux density variation due to stator slot openning of a concentrated coil permanent magnet machine. In: *Southern African Universities Power Engineering Conference (SAUPEC)*, Cape Town. 2007.

International conference

- Rix, A., Kamper, M. andWang, R.-J.: Design and performance evaluation of concentrated coil permanent magnet machines for in-wheel drives. In: *IEEE International Electric Machines Drives Conference*, vol. 1, pp. 770-775, Turkey, May 2007.
- Kamper, M., Rix, A., Wills, D. and Wang, R.-J.: Formulation, finite-element modeling and winding factors of non-overlap winding permanent magnet machines. In: *Proceedings of the XVIII International Conference on Electrical Machines (ICEM2008)*, p. 5, Vilamoura, September 2008.
- de Kock, H., Rix, A. and Kamper, M.: Optimal torque control of interior permanent magnet synchronous machines in the full speed range. In: *Proceedings of the XVIII International Conference on Electrical Machines (ICEM2008)*, p. 6, Vilamoura, September 2008.
- Rix, A. and Kamper, M.: Comparison of non-overlap winding radial flux PM hub drives for EVs. In: *Proceedings of the XIX International Conference on Electrical Machines (ICEM2010)*, p. 6, Rome, September 2010.

Journal

- De Kock, H., Rix, A. and Kamper, M.: Optimal torque control of synchronous machines based on finite-element analysis. *Industrial Electronics, IEEE Transactions on*, vol. 57, no. 1, pp. 413-419, January 2010.

DEDICATIONS

To my wife Christa and my son Edrich

CONTENTS

LIST OF FIGURES

LIST OF TABLES

NOMENCLATURE

Abbreviations

ABS	Anti-lock Braking System
CPSR	Constant Power Speed Range
DSP	Digital Signal Processor
EV	Electric Vehicle
FE	Finite Element
FPGA	Field-programmable Gate Array
GCD	Greatest Common Divisor
HEV	Hybrid Electric Vehicle
HM1	Hub Motor 1
HM2	Hub Motor 2
ICE	Internal Combustion Engine
IPMSM	Interior Permanent Magnet Synchronous Machine
LCM	Lowest Common Multiple
MMF	Magnetomotive Force
PM	Permanent Magnet
PMSM	Permanent Magnet Synchronous Machine
RSM	Reluctance Synchronous Machine
SA	South Africa

Roman Symbols

b	instantaneous flux density	[Wb/m^2]
b_m	magnet width	[m]
d	conductor diameter	[m]
e	instantaneous voltage	[V]
e_{abc}	instantaneous voltage of the phase windings	[V]
e_{mn}	instantaneous voltage of the magnet coils	[V]
e_t	instantaneous voltage of the magnet coils due to the airgap permeance	[V]

f	stator phase current frequency	[Hz]
f_{mn}	MMF of a single magnet coil	[At]
g	air gap length	[m]
h_m	magnet height	[m]
i_{abc}	instantaneous phase current	[A]
k_{dmn}	n^{th} order harmonic magnet distribution factor	
k_{dsn}	n^{th} order harmonic coil distribution factor	
k_{exc}	excess or anomalous loss constant	
k_{pmn}	n^{th} order harmonic magnet pitch factor	
k_{psn}	n^{th} order harmonic coil pitch factor	
k_{ptn}	n^{th} order harmonic slot pitch factor	
k_{wmn}	n^{th} order harmonic magnet winding factor	
k_{wsn}	n^{th} order harmonic coil winding factor	
k_c	Carter factor	
k_e	eddy current loss constant	
k_h	hysteresis loss constant	
l	active length	[m]
l_e	end-winding active length	[m]
m	number of phases	
m_r	mass of iron region	[kg]
n_a	number of parallel circuits	
n_c	number of stator conductors in a region	
n_r	magnet coil MMF harmonic order	
n_s	stator coil MMF harmonic order	
n_t	slot permeance harmonic order	
p	number of poles in a machine section	
p_{exc}	spesific iron loss excess or anomalous component	[W/kg]
p_{mn}	instantaneous power of magnet coils	[W]
p_c	spesific iron loss	[W/kg]
p_e	spesific iron loss eddy current component	[W/kg]
p_h	spesific iron loss hysteresis component	[W/kg]

p_m	magnet average loss density	[W/m^3]
p_p	number of pole pairs in a machine	
r_s	winding resistance	[Ω]
r	radius	[m]
u	number of coils distributed in a coil phase group	
w_s	lamination thickness	[m]
z	number of conductors in a slot	
A	magnetic vector potential	[Wb/m]
A_{cu}	copper area of a slot	[m^2]
A_n	n^{th} order machine constant	
B	flux density amplitude	[Wb/m^2]
B_r	radial flux density amplitude	[Wb/m^2]
B_θ	tangential flux density amplitude	[Wb/m^2]
E	voltage amplitude	[V]
E_{mn}	induced voltage amplitude of the magnet coils	[V]
E_{sn}	induced voltage amplitude of the stator windings	[V]
F_{ph}	phase group MMF	[At]
F_{sn}	n_s^{th} order 3-phase winding MMF space harmonic	[At]
F_c	stator coil MMF	[At]
F_{cn}	n^{th} order stator coil MMF	[At]
F_{mn}	n^{th} order rotor MMF	[At]
F_{rn}	n^{th} order rotor MMF	[At]
H_c	coercivity of magnet material	[A/m]
H_{ns}	n^{th} order stator coil MMF amplitude	[At]
I	peak phase current	[A]
I_m	magnet coil current	[A]
J	current density	[A/m^2]
L_e	end winding inductance	[H]
L	inductance	[μH]
M_s	number of machine sections	
N	number of turns in series per phase	

N_{sn}	mechanical speed of the n^{th} order stator MMF harmonic	[r/min]
N_L	number of coil layers	
N_r	mechanical rotor speed	[r/min]
N_s	number of stator slots	
P_{cu}	copper losses	[W]
P_c	iron losses	[W]
P_f	frequency losses	[W]
P_s	conductor eddy current losses	[W]
P_m	permanent magnet losses	[W]
Q	number of stator coils	
S	number of stator slots per machine section	
T_{inst}	instantaneous torque	[Nm]
T_{ave}	average torque	[Nm]
T_{rip}	ripple torque	[Nm]
T_{max}	maximum torque	[Nm]
T_{min}	minimum torque	[Nm]
T_{mn}	torque due to the stator MMF	[Nm]
T_{sn}	torque due to the rotor MMF	[Nm]
T_{tn}	torque due to the stator slots	[Nm]
Vol	volume of a region	[m^3]
W_s	number of winding sections	

Greek Symbols

δ_{ns}	displacement angle	[rad]
Δ	peak to peak air gap permeance	[Wb/At]
ϵ	penalty function	
γ	mass density	[kg/m^3]
λ	flux linkage	[Wb]
λ_l	leakage flux linkage	[Wb]
λ_e	air gap flux linkage	[Wb]
λ_{PM}	flux linkage due to the permanent magnet	[Wb]

Λ_s	air gap permeance referred to the stator	[Wb/At]
Λ_r	air gap permeance referred to the rotor	[Wb/At]
$\Lambda_{s(ave)}$	average air gap permeance	[Wb/At]
ω	angular velocity of the stator current space phasor	[rad/s]
ω_r	rotor MMF electrical angular velocity	[rad/s]
ω_{rn}	relative angular velocity of the stator MMF harmonics with regards to the rotor	[rad/s]
ω_s	relative angular velocity of the rotor MMF with regards to the stator	[rad/s]
ω_{sn}	angular velocity of the stator MMF harmonics	[rad/s]
ϕ	current angle	[rad]
ρ	resistivity	[Ωm]
σ	material conductivity	[S/m]
σ_c	ratio of coil width to slot width	
σ_m	p.u. magnet pitch angle	
τ	periodicity indicator	
θ_c	electrical coil pitch angle	[rad]
θ_w	electrical coil width angle	[rad]
θ_g	electrical slot width angle	[rad]
θ_m	electrical magnet pitch angle	[rad]
θ_p	electrical pole pitch angle	[rad]
θ_r	electrical rotor angle	[rad]
θ_s	average electrical slot pitch angle	[rad]
θ_t	stator slot teeth width angle	[rad]
ξ_{sn}	n_s^{th} order harmonic coil width factor	

Constants

μ_0	permeability of free space $(4\pi \times 10^{-7})$	[H/m]

Phasors, vectors and matrices

$\mathbf{i}_{abc}$	3-phase stator current vector
$\mathbf{i}_{dq0}$	stator current vector in the $dq0$ reference frame

$\mathbf{I}_{dq0}$	steady state stator current vector in the $dq0$ reference frame
$\mathbf{I}_s$	stator current space phasor
$\mathbf{v}_{abc}$	3-phase stator voltage vector
$\mathbf{v}_{dq0}$	stator voltage vector in the $dq0$ reference frame
$\mathbf{V}_{dq0}$	steady state stator voltage vector in the $dq0$ reference frame
$\mathbf{V}_s$	stator voltage space phasor
$\boldsymbol{\lambda}_{abc}$	3-phase stator winding airgap flux linkage vector
$\boldsymbol{\lambda}_{dqo}$	stator winding airgap flux linkage vector in the $dq0$ reference frame
$\boldsymbol{\lambda}_s$	stator flux linkage space phasor
$\mathbf{k}_p$	Park's transformation matrix

Subscripts

0	0-axis in the $dq0$ reference frame
d	d-axis in the $dq0$ reference frame
m	magnet
n	harmonic order
q	q-axis in the $dq0$ reference frame
r	rotor
s	stator coil
t	stator slot
w	winding

CHAPTER 1

INTRODUCTION

There is some confusion as to who invented the first battery electric car. Either Thomas Davenport or Robert Anderson can lay claim to the invention of a crude electric carriage, using non-rechargeable batteries, at around 1834. In any case, electric vehicles (EVs) held all vehicle land speed records until about 1900 [1].

By the turn of the century America was prosperous, and cars then available in steam, electric, or gasoline versions, were becoming more popular. The years 1899 and 1900 were the high point of electric cars in America, as they outsold all other types of cars. EVs had many advantages over their competitors in the early 1900s. They did not have the vibration, smell, and noise associated with gasoline cars. Changing gears on gasoline cars was the most difficult part of driving, while electric vehicles did not require gear changes [2].

Today the internal combustion engine (ICE) is the dominant propulsion method for automobiles, but electric power has remained commonplace in other vehicle types, such as trains and smaller vehicles such as golf cars and fork lifts. During the last few decades, increased concern over the environmental impact of the petroleum-based transportation infrastructure has led to renewed interest in an electric transportation infrastructure. EVs differ from fossil fuel-powered vehicles in that the electric energy they consume can be generated from a wide range of sources, including fossil fuels, nuclear power and renewable sources such as tidal power, solar power and wind power or any combination of these [3].

The developments in power electronics and micro-processors, together with new developments in analysis, design and materials for high-power density electrical machines, are important in making the EV technically and economically more viable today [4]. EVs can be classified in three categories. The first is EVs that are powered from two power sources in a series (Fig. 1.1c) or parallel mode (Fig. 1.1a and 1.1b), called hybrid electric vehicles (HEVs). The second is those that are powered from an engine-generator system, generally called diesel-electric or engine-electric vehicles. The third category is those EVs that are powered from only one power source such as batteries or fuel cells as shown in Fig. 1.1d. Although the drive configuration for these types of vehicles is different, one configuration is of special interest due to the unconventional location of the electric machine, namely those that use in-wheel motors.

For a little more than a decade, many car manufacturers and tire companies have been wor-

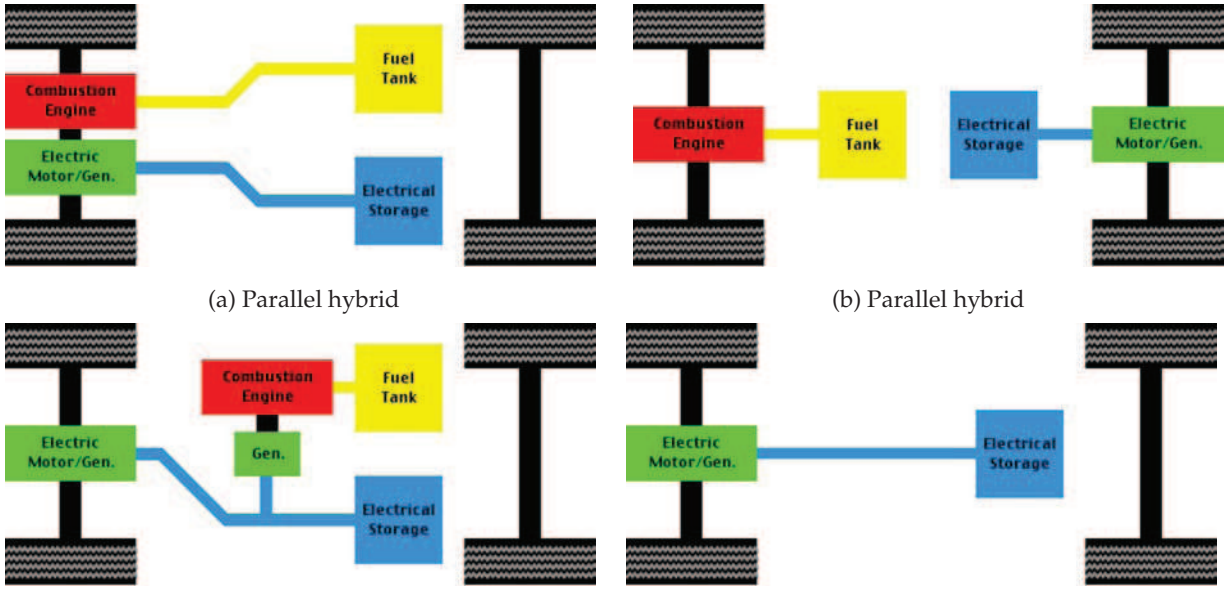

(a) Parallel hybrid

(b) Parallel hybrid

(c) Series hybrid

(d) Battery electric

Figure 1.1: Different EV drive-train options.

king hard to change how automobile owners think about and use their tires. More specifically, they want to take the vehicle's engine, as well as many other integral parts of a functioning automobile, and place it all inside the wheel.

The basic principle behind a vehicle equipped with in-wheel electric motors is simple. The ICE, normally found under the hood, is replaced with two (or more) in-wheel motors, a converter and a battery pack.

1.1 History of the hub or in-wheel motor

The concept of the first in-wheel motor, also known as a hub motor, was conceived by Wellington Adams of St. Louis, Missouri in 1884. Wellington registered a patent for an electric motor built directly in the vehicle wheel, although it was attached via some complicated gearing [5]. The concept of his design is shown in Fig. 1.2.

After Adams' design Albert Parcelle of Boston, MA developed the first fully incorporated wheel hub motor in his "Electro-Motor Traction-Wheel" and patented it in 1890 [6]. Also patented in 1890 was the first high torque low speed wheel motor that was incorporated into the wheel without gearing by Edward Parkhurst of Woburn, MA [7].

An early wheel hub electric motor was invented by Frenchman Charles Theryc and patented in 1896 as the US patent entitled "Wheel with Electric Motor hub for Vehicles". In the patent he explained all the advantages including no transmission losses because of the absence of classic transmission rods from engines to wheels [8].

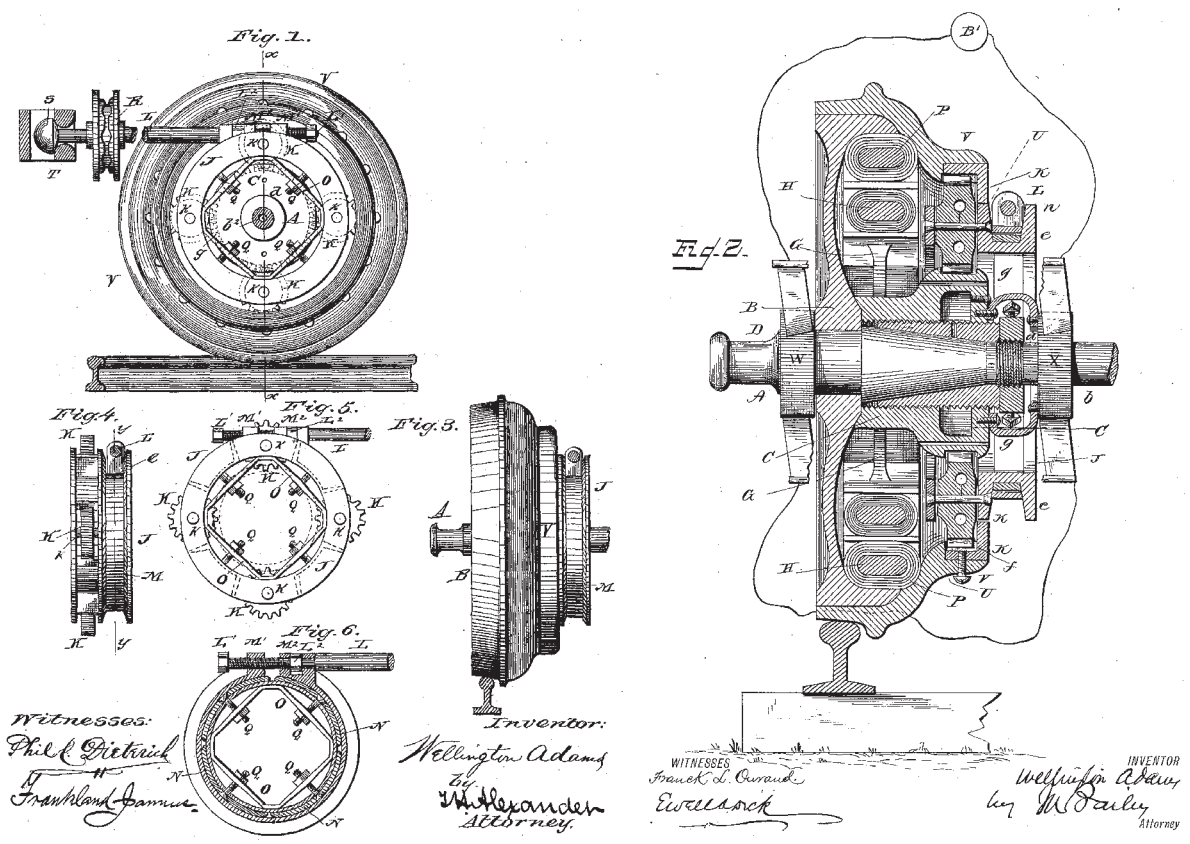

(a) (b)

Figure 1.2: Wellington Adams' patent figures of 1884.

An electric car, with wheel hub motors, was first raced by engineer Ferdinand Porsche in 1897 in Vienna, Austria. Porsche's first engineering training was electrical, not internal combustion based. As a result he developed his first cars as electric cars with electric wheel hub motors that ran on batteries. The Lohner Porsche, shown in Fig. 1.3a, was fitted with wheel motors in the front wheels and appeared at the World Exhibition in Paris in 1900. In the following years, 300 Lohner Porsches were made and sold to wealthy buyers [9].

Porsche recognized the efficiencies of power transmission of the electric wheel hub motor over a central engine driving the wheels through a transmission. In an effort to overcome the low battery capacities of the day, he developed an electrical wheel hub motor car that got its electric power from a gasoline driven generator in the car, effectively inventing the HEV. He set many speed records of the day in this gasoline powered generator car with front wheel electric hub motors. Eventually the growth in power of the gasoline engine overtook the power of the electric wheel hub motors and this made up for any losses through a transmission. As a result vehicles moved to gas engines with transmissions.

Today several concept cars have been developed using in-wheel motors. In 2006, PML

Flightlink demonstrated the Hi-Pa Drive in a series-hybrid car at the British Motor Show in London, using a Mini dubbed the "Mini QED", Fig. 1.3b, with in-wheel motors at all four wheels [10]. The Peugeot BB1, Fig. 1.3c, is a full-electric concept car presented more recently by Peugeot in September 2009 at the Frankfurt Motor Show [11]. It incorporates rear in-wheel motors, designed by Michelin, each with a maximum power output of 7.5 kW and torque on each wheel of 320 Nm.

A conventional vehicle uses mechanical means to transmit power from a centrally mounted engine/motor to the wheels. With an ICE vehicle this mechanical transmission must have multiple gear ratios to compensate for an ICE having no usable power at low engine speeds. An electric motor mounted directly inside a wheel without any mechanical transmission should minimize such losses.

Cars with electronic control of brakes and acceleration provide more opportunities for computerized vehicle dynamics such as:

- Active cruise control, where the vehicle can actively keep a set distance to a vehicle ahead
- Collision avoidance, where the vehicle can automatically brake to avoid a collision with another object
- Emergency brake assist, where the vehicle can sense an emergency stop and apply maximum braking effort
- Active software differentials, where individual wheel speed is adjusted in response to other inputs
- Active brake bias, where individual wheel brake effort is adjusted in real time to maintain vehicle stability
- Brake steer, where individual wheel brake bias is adjusted to assist steering (similar to a tracked vehicle like a Bulldozer)

As wheel motors brake and accelerate a vehicle with a single solid state power converter, many of the above features can be added as software upgrades rather than requiring additional hardware (like with ABS etc.) to be installed. This should result in cheaper active dynamic safety systems for wheel motor equipped road vehicles.

Although the concept is relatively simple in theory, a number of questions about performance and function in in-wheel motors can be posed.

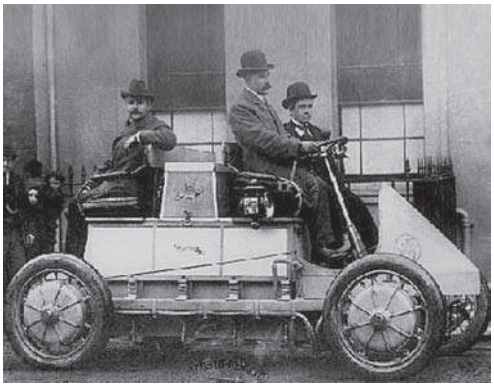

(a) Ferdinand Porsche's Lohner of 1897

(b) PML Flightlink's Mini QED of 2006

(c) Peugeot's BB1 of 2009

(d) SA's concept EV, the Joule

Figure 1.3: EVs of yesterday and today.

1.2 A South African EV initiative

In 2005 an initiative was started in South Africa (SA) to develop a first battery powered EV in SA. The SA EV is now known as the Joule, shown in Fig. 1.3d and was revealed at the 2008 Paris Automotive show. As part of the initiative, Stellenbosch University was approached to design a prototype in-wheel drive system. This is when the author became involved in the design and control of an in-wheel motor drive system for this car.

1.3 Hub-motor drive project description

At the start of the project there were no specifications for the machine drive system and the responsibility was put on the author to do research and determine preliminary specifications. This research included fundamental vehicle modelling to determine the power and torque requirements of a small utility vehicle. The only parameters that were given at the time were: a vehicle drag coefficient, the frontal area of the vehicle and the loaded vehicle mass. The vehicle modelling is described in Appendix B, and was used to determine the preliminary drive

specifications.

It was decided that four electrical motors, one in each wheel, would be used to drive the electrical vehicle. These motors would not have any gears and should therefore be low speed, high torque machines. Each machine had to meet the specifications given in Table 1.1. A radial flux topology was chosen due to the restriction on the machine's outer diameter. The rotor would be of the outside type, to optimize the air gap radius, and connected directly to the wheel. The stator would have non-overlap, double layer, concentrated windings to minimize the end winding length and reduce the torque ripple.

The torque requirement in Table 1.1 is based on low speed driving, whereas the power requirement is based on a top speed of 130 km/h, which roughly translates to a wheel speed of 1200 r/min.

1.3.1 1^{st} Prototype machine

A pole-slot choice of 40/30 was used for the first machine design. A suggestion was made to use open slots and preformed coils for the stator rather than a normally wound stator. This open slot preformed coil machine has the benefit of having lower cost and possibly better cooling options. After some discussion on the magnets' mechanical properties it was proposed that the magnets be totally enclosed in the iron of the rotor to protect them against shock and vibration forces during normal operation.

When the allowed outer dimensions of the active machine parts had been fixed, the electrical design was started and various topologies were modelled with a non-commercial, finite element program. Up to this point in time the FE package had only been used to model machine sections with negative boundary conditions. To correctly solve for the magnetic vector potential in the model the FE package had to be adapted to use positive boundary conditions. After the implementation of the positive boundary conditions on the modelled machine section an optimization was performed. Being able to perform optimizations as part of this FE

Table 1.1: In-wheel, hub-motor specifications

Type	Permanent-Magnet
Rated Power	9 kW
Rated Torque	220 Nm
Max speed	1200 r/min
Dimensions	Must fit inside a 15" wheel rim i.e. 280mm diameter

modelling package is one of the main reasons it is used instead of a commercial package.

A pole slot combination of 40/30 was chosen because it has fewer coils than e.g. a 40 pole 39 slot double layer machine. The 40 pole 30 slot double layer combination results in a machine that is cheaper to manufacture. It was also planned to compare the performance of a optimally designed machine with a pole slot combination having a low winding factor and an optimally designed machine having a high winding factor.

The manufacturing of the first hub motor was successfully completed and is discussed in Chapter 7. Tests were done to see if the prototype worked and results were given comparable to the FE predicted results. This motor had to reach top speeds beyond the motor's base speed, during operation in the vehicle, so a control algorithm that included active field weakening had to be implemented. The control algorithm developed, incorporates maximum torque per ampere and efficient field weakening control.

1.3.2 2^{nd} Prototype machine

The focus of the second prototype was on using two hub motors for the rear wheels together with another type of drive for the front wheels. The author's focus stayed on the hub motors and development continued.

A motor had to be designed to fit certain dimensions while giving the best possible performance. The machine would have 30 poles instead of 40 and the number of slots was chosen based on the working harmonic winding factor given by literature. A slot number of 27 gave a good winding factor and 3 magnetically symmetrical machine slices, so only $\frac{1}{3}^{rd}$ of the machine had to be modelled in the FE program.

The non-commercial FE program was then used to model the 3 phase machine with non-overlapping double layer windings in semi-closed stator slots with embedded magnets on the outer rotor. The optimization performed on the machine design resulted in the parameters given in Table 1.2.

Table 1.2: Performance parameters of HM2

Type	Permanent-Magnet
Rated Power	16 kW
Rated Torque	340 Nm
Max speed	1200 r/min
Dimensions (Active area)	270 mm diameter 100 mm long

Two of these prototype hub motors (HM2) had to be built for integration in a first prototype vehicle. After the complete assembly process the motors were mounted on the test bench one at a time for testing. The same testing procedure, as for HM1, was followed for HM2. A prototype DSP control system and inverter were developed that would also have had to be incorporated in the vehicle prototype. The thermal analysis and temperature testing of both the 1^{st} and 2^{nd} prototype machines was done by mechanical engineers working on the project and is not part of this thesis. It is believed that the cooling design that is based on a total machine efficiency, is sufficient and will enable the machine to work indefinitely at normal operating conditions.

1.4 Problem statement and PhD study

The focus of study in this thesis is on the design, comparison and evaluation of radial flux hub motors for use in a small utility vehicles, such as the Joule. A low speed, high torque permanent magnet synchronous machine (PMSM) is chosen to be used for the hub motor. This decision is based on the fact that higher efficiency and torque density are possible using permanent magnets, compared to copper excited machines.

With regard to the PMSM drive it is important to mention some aspects that are prominent (or lacking) in literature. These are the following:

(i) The MMF's harmonic content and the winding factors of three phase PM machines have been mathematically described by various authors in the past, amongst others [12–15]. These mathematical descriptions of a machine's MMF and the calculation of the winding factors are normally quite complex and are presented in literature for only the stator phase windings.

(ii) Torque ripple, especially cogging torque, is modelled in literature by FE methods and/or analytical methods. The FE method, although accurate, is time consuming, whereas the analytical methods are fast but rather complicated and not as accurate [16–19]. Torque quality is important for most applications, and the minimization of the cogging and load torque ripple is an important aspect when designing PM machines [20–25].

(iii) Iron losses in electrical machines have been, and still are, an important topic for electrical machine design. For the designer it is important to have an accurate iron loss estimation to compare designs. The estimation of iron losses in PM machines has received a lot of attention, especially looking at machines with field weakening ability [26–39].

(iv) Literature shows a lot of work published on the design of axial flux machines for automotive applications [40–49]. Compared to the axial flux machine, the radial flux machine, for

EV applications, has received little attention in literature [50–53]. Although the radial flux type of machine is widely used, there is only some information online where it is used for an EV [54–56].

(v) Direct drives that are used for in-wheel operation, operate through a wide speed range. Optimum designed in-wheel motors should be able to supply the required power and torque at high speed operation while not being oversized for low speed operation. To give an indication of the machine's torque performance versus speed, the constant power speed range (CPSR) of the machine is considered. The importance of the CPSR can be seen from the amount of work dedicated in literature to this topic [57–63]. To operate PMSMs beyond their base speed, requires a specialized torque control scheme that incorporates field weakening [64–67].

In the light of the abovementioned literature and in the light of the focus on PM hub motor drives, the following is considered in this thesis:

(i) The development of a simple analytical method to identify MMF harmonics and to calculate torque ripple of surface-mounted PM machines. The aim is to use this model in a first design approach of the PM hub motor.

(ii) A method for calculating the high frequency losses in PM machines by making use of a number of static FE solutions. The aim here is to use this method in the design optimization of the PM hub motor.

(iii) A design optimization procedure using FE solutions and an optimization algorithm. The aim is to optimize the design and do a detail performance comparison of PM hub motors with different types of PM rotors.

(iv) An optimum control method for PM hub motors over the entire speed range of the drive. What is important here is to ensure high efficiency performance of the drive over the entire speed range.

(v) The practical implementation, testing and evaluation of two different hub motor drives. The difference in the hub motors lies in the fact that the one hub motor has an expected low manufacturing cost, but apparently with not-as-good performance, while the other hub motor with a differently manufactured stator has an expected good performance.

1.5 Thesis layout

The layout of the remainder of this thesis is as follows:

Chapter 2: The harmonics present in the concentrated-coil PM machine are mathematically explained, and equations for various proposed winding factors are derived in this chapter. The equations for the analytical calculation of torque and torque ripple, resulting from the air gap MMF's are presented.

Chapter 3: The equivalent circuits and equations, that describe the PMSM, are explained. The parameters of the circuit models are determined from the FE field solution.

Chapter 4: The focus of this chapter is on frequency loss models that are given by literature, and how these models are combined with FE analysis to predict these machine losses.

Chapter 5: Various aspects that influence the performance of a PM machine design are investigated. Design optimizations are done on various machines to determine the effect of the different design choices.

Chapter 6: Considering the EV application, an optimal control algorithm for PM hub drives is presented. This torque control algorithm is applied through the whole speed range of the drive, with little on-board computing required.

Chapter 7: The design aspects and optimization method discussed in Chapter 5 are used to design two prototype in-wheel motors. The construction and testing of these in-wheel motors are discussed in detail in this chapter, with accompanying pictures.

Chapter 8: In this chapter a summary with conclusions are given and recommendations are made for future research.

CHAPTER 2

HARMONIC ANALYSIS

The MMF's harmonic content and winding factors of three phase machines have been described by various authors in the past [12–15, 68]. These mathematical descriptions of a machine's MMF and the calculation of the winding factors are normally complex and only presented for the stator phase windings.

In this Chapter the stator coil MMF of a 3-phase machine is described using simple *sin* and *cos* terms. From this description a simple formula to calculate the winding factor is obtained [69]. By representing the rotor magnets with thin sheet coils in air, the same model as for the 3-phase windings is used to describe the harmonic content of the rotor MMF and to define a magnet winding factor. The air gap permeance function is modelled in a similar way and used to describe the harmonic content of the interaction between the stator slots and the rotor magnets.

Torque, torque ripple and cogging torque are then calculated from the power induced in the stator windings and magnet coils. Torque quality is important for certain applications and the minimization of the torque ripple is an important factor when designing PM machines [20–25].

In literature, instantaneous torque is calculated by either finite element methods or analytical methods from computing the magnetic fields. The finite element method, although accurate, is time consuming, while analytical methods are fast but rather complicated [16–19]. The aim in this Chapter is to present a simple analytical method to identify MMF harmonics and to calculate torque ripple for surface-mounted PM machines using non-overlap windings and to use this method in a first design approach of the PM hub motor.

2.1 Winding parameters

Before the MMF harmonics are studied, it is important first to define some machine and winding parameters that are used in the analysis for non-overlap windings. With N_s the number of stator slots and N_L the number of coil layers in a slot ($N_L = 1$ for single and $N_L = 2$ for double layer windings), the number of stator coils is given by $Q = N_L N_s/2$. The number of machine sections, M_s, that repeat within the machine can be determined by taking the greatest common divisor (gcd) of the number of pole pairs, p_p, and the number of stator coils, Q, of the machine,

that is

$$M_s = gcd(p_p, Q) \,. \tag{2.1}$$

The number of winding sections, W_s, that repeats itself (with negative or positive periodicity) can be determined by taking the greatest common divisor (gcd) of the number of poles, $2p_p$, and the number of coils, Q, of the machine, that is

$$W_s = gcd(2p_p, Q) \,. \tag{2.2}$$

W_s is used to determine if negative or positive periodicity is occurring in a machine section; the parameter that gives the indication of periodicity, τ, is simply given by

$$\tau = \frac{W_s}{M_s} \,. \tag{2.3}$$

τ is either $\tau = 1$ indicating positive periodicity, or $\tau = 2$ indicating negative periodicity. With negative periodicity a coil phase group repeats itself (but negatively) within a machine section; the latter information is required to determine the total MMF of the positive and negative phase groups in a machine section where negative periodicity is occurring.

The number of coils, u, distributed in a coil phase group, can be determined by

$$u = \frac{Q}{mW_s} \,, \tag{2.4}$$

where $m = 3$ for three phases. The u-coil flux linkage and induced voltage space phasors of the n_s^{th} order harmonic are phase-displaced by the electric angle, δ_{ns}, (only for integral windings[1]) as

$$\delta_{ns} = \left\{ \begin{array}{cc} 2\theta_s & N_L = 1 \\ \theta_s + \dfrac{\pi}{|n_s|} & N_L = 2 \end{array} \right\} , \tag{2.5}$$

where θ_s is the average electrical slot pitch angle given by

$$\theta_s = \frac{2\pi}{S} \tag{2.6}$$

and S the number of stator slots per machine section, that is $S = \frac{N_s}{M_s}$.

2.2 Stator MMF harmonics

The change in the MMF of a stator coil is assumed to be represented by the waveform of Fig. 2.1. This waveform allows for the fact that the MMF does not change abruptly at each coil side and

[1] In integral non-overlap winding layouts the coils of a coil phase group are all grouped together, but in fractional layouts the coils of a coil phase group are distributed unevenly in a more complex way in the winding section [69].

is assumed to be a feasible approximation of the unknown curve. The waveform is taken over a winding section that spans $\frac{2\pi}{\tau}$ electrical radians for the fundamental[2] MMF harmonic. The other parameters defined in Fig. 2.1 are the coil pitch angle, θ_c, the magnet pitch angle, θ_m, the pole pitch angle, θ_p, and the coil width angle, θ_w, all in fundamental electrical radians. The number of poles and the number of slots in a machine section are respectively given by p and S. The pole pitch angle, for example, is given by $\theta_p = \frac{2\pi}{p}$. Finally N is the number turns of the coil and i the turn current.

The windings of a double layer topology will affect the coil pitch, θ_c, and for this analysis it is assumed that windings are either placed next to each other or on top of each other in a slot. The slot width is given by θ_g, as shown in Fig. 2.2b. An indicator, σ_c in Fig. 2.2, is given by $\sigma_c = \frac{\theta_w}{\theta_g}$ and is used to calculate the correct coil pitch as given by (2.7).

$$\theta_c = \theta_s - \theta_w \left(\frac{1}{\sigma_c - 1} \right). \tag{2.7}$$

From Fig. 2.1 it is clear that $F_c(-\theta) = F_c(\theta)$ so that *sine* terms do not appear in the Fourier series of the waveform, but only *cosine* terms. Hence, real analysis is easily used. From Fig. 2.1 and

[2]The average of the working harmonic is referred to, in the text, as the fundamental harmonic.

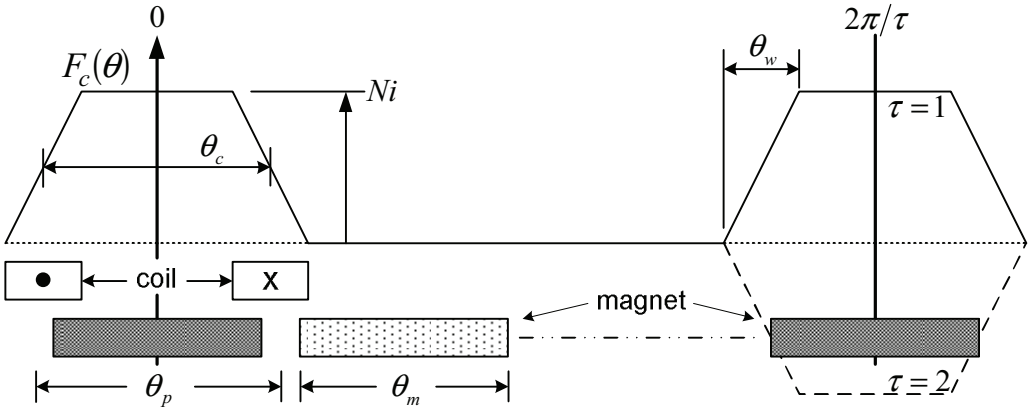

Figure 2.1: MMF generated by a coil in a winding section.

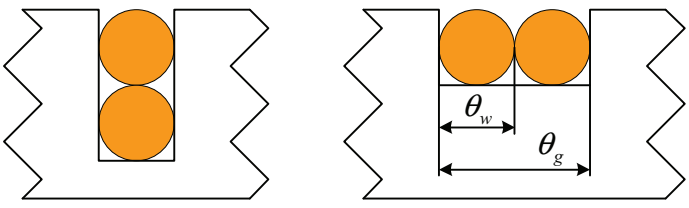

(a) $\sigma_c = 1$ (b) $\sigma_c = 0.5$

Figure 2.2: Placement of double layer windings in a slot.

after some mathematical executions, the n_s^{th} order coil MMF space harmonic is expressed as

$$F_{cn} = H_{ns} i \cos(n_s \theta), \tag{2.8}$$

and

$$H_{ns} = \frac{2N}{\pi |n_s|} k_{psn} \xi_{sn}, \tag{2.9}$$

where k_{psn} is the n_s^{th} order harmonic coil pitch factor and ξ_{sn} the n_s^{th} harmonic coil width factor respectively given by

$$k_{psn} = \sin\left(\frac{|n_s|\theta_c}{2}\right) \qquad \text{and} \tag{2.10}$$

$$\xi_{sn} = \frac{\sin(|n_s|\theta_w/2)}{|n_s|\theta_w/2}. \tag{2.11}$$

The n_s^{th} order MMF space harmonic of a phase group u coils and τ winding sections can be expressed as

$$\begin{aligned} F_{ph} &= \tau \sum_{j=1}^{u} H_{ns} i \cos n_s[\theta - (j-1)\delta_{ns}] \\ &= \tau u H_{ns} k_{dsn} i \cos n_s(\theta - \alpha_{ns}) \\ &= A_n i \cos n_s(\theta - \alpha_{ns}), \end{aligned} \tag{2.12}$$

where

$$\alpha_{ns} = (u-1)\frac{\delta_{ns}}{2}. \tag{2.13}$$

The n_s^{th} order distribution factor, k_{dsn}, in (2.12) is given by

$$k_{dsn} = \frac{\sin(|n_s| u \delta_{ns}/2)}{u \sin(u\delta_{ns}/2)}. \tag{2.14}$$

A_n in (2.12) is a n_s^{th} order machine constant given by

$$A_n = \frac{2\tau u N}{\pi |n_s|} k_{wsn} \tag{2.15}$$

where k_{wsn} is the n_s^{th} order winding factor given by

$$k_{wsn} = k_{psn} k_{dsn} \xi_{sn}. \tag{2.16}$$

From the analysis it is seen that for negative periodic phase windings F_{ph} equates to zero for all even harmonic orders, while for the positive periodic phase windings this is not the case. The possible harmonic order is as follows

$$|n_s| = \left\{ \begin{array}{llllll} 1, & 2, & 3, & 4, & 5, \ldots & \tau = 1 \\ 1, & & 3, & & 5, \ldots & \tau = 2 \end{array} \right\}. \tag{2.17}$$

From (2.12) the n_s^{th} order 3-phase winding MMF space harmonic is given by

$$F_{sn} = A_n \left[i_a \cos n_s(\theta - \alpha_{ns}) + i_b \cos n_s(\theta - \alpha_{ns} - \frac{2\pi}{3}) + i_c \cos n_s(\theta - \alpha_{ns} + \frac{2\pi}{3}) \right]. \tag{2.18}$$

If the phase currents are

$$[i_{abc}] = \begin{bmatrix} I\sin(\omega t) \\ I\sin(\omega t - \frac{2\pi}{3}) \\ I\sin(\omega t + \frac{2\pi}{3}) \end{bmatrix}, \tag{2.19}$$

with I the peak of the phase current, then F_{sn} can be expressed as

$$F_{sn} = \frac{3A_n I}{2a} \sin[\omega t + n_s(\theta - \alpha_{ns})] \tag{2.20}$$

with a the number of parallel circuits and

$$n_s = \left\{ \begin{array}{cccccccccc} -1, & 2, & -4, & 5, & -7, & 8, & -10, & 11, \ldots & \tau = 1 \\ -1, & & & 5, & -7, & & & 11, \ldots & \tau = 2 \end{array} \right\}, \tag{2.21}$$

where the sign of the harmonic indicates the direction of the travelling wave. From the results above the order of MMF harmonics present in negative and positive periodicity machines are given by

$$n_s = 3\tau k - 1, \quad k \in \mathbb{Z}. \tag{2.22}$$

The results of the above described MMF show that:

- multiples of 3^{rd} stator MMF harmonics do not exist in 3-phase machines,
- even stator MMF harmonics do not exist when negative periodicity is occurring,
- some stator MMF harmonics travel in the backward and some in the forward direction,
- the stator MMF harmonics travel at speeds proportional to the reciprocal of their orders.

2.2.1 Case studies

For a first case study a 12-slot, 10-pole non-overlap winding machine is chosen, and the per unit MMF harmonic content is calculated and shown in Fig. 2.3[3]. Both the single- (Fig. 2.3a) and double- (Fig. 2.3b) layer cases have negative periodicity and no even order harmonics are present. The single layer machine has a large sub harmonic, $n_s = 1$, as shown in Fig. 2.3a with the working harmonic, $n_s = 5$, equal to 1 p.u.

The harmonic content of an 18-slot, 14-pole machine with both single- and double-layer non-overlap windings is shown in Fig. 2.4. This combination with a working harmonic of $n_s =$

[3]The MMF of the working harmonic is taken as the base value for the per unit calculation.

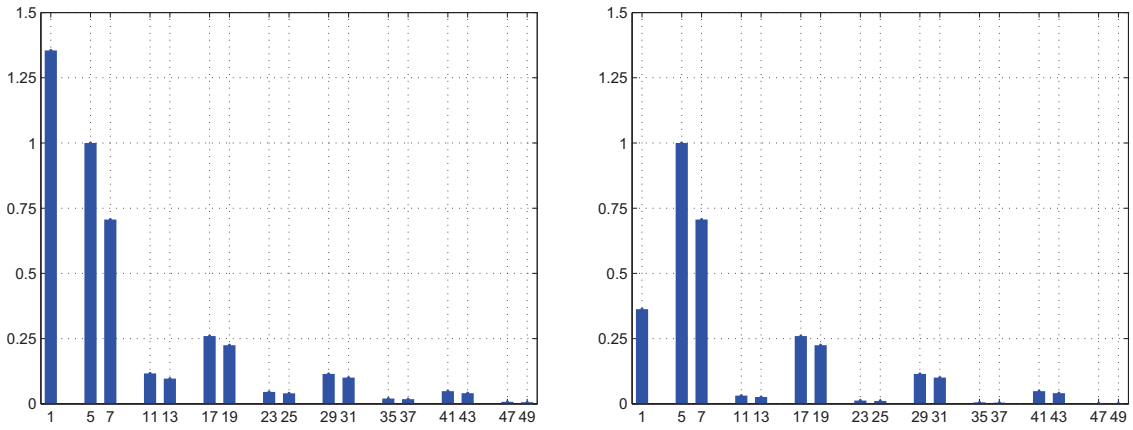

(a) Single Layer (b) Double Layer

Figure 2.3: Per unit stator MMF harmonic content of a 12-slot, 10-pole non-overlap winding PM machine.

7 has a negative periodicity for the double-layer winding (Fig. 2.4b) and a positive periodicity for the single-layer winding (Fig. 2.4a). The even order harmonics are not present in the double-layer winding, while they appear in the harmonic content of the single-layer winding.

2.3 Rotor MMF harmonics

By modelling the PMs as current sheets around material with a certain permeability (this permeability is close to that of air for high energy density magnets), the change of the MMF of a magnet coil can be represented by the waveform of Fig. 2.5. The single turn magnet coil current I_m, which is also the peak to peak change in MMF, is given by

$$I_m = H_c h_m, \tag{2.23}$$

where H_c is the coercivity of the magnet material and h_m is the height of the magnet. From Fig. 2.5 the n_r^{th} order MMF of a single magnet coil can be expressed similar to (2.8) as

$$f_{mn} = \frac{2 I_m k_{pmn}}{n_r \pi} \cos(n_r \theta), \tag{2.24}$$

where k_{pmn} is the n_r^{th} order magnet coil pitch factor similar to (2.10) given by

$$k_{pmn} = \sin\left(\frac{n_r \theta_m}{2}\right). \tag{2.25}$$

The total magnet MMF of all the magnet coils in a machine section, shown in Fig. 2.6, is given by

$$F_{mn} = \frac{2 p I_m k_{pmn} k_{dmn}}{n_r \pi} \cos(n_r \theta), \tag{2.26}$$

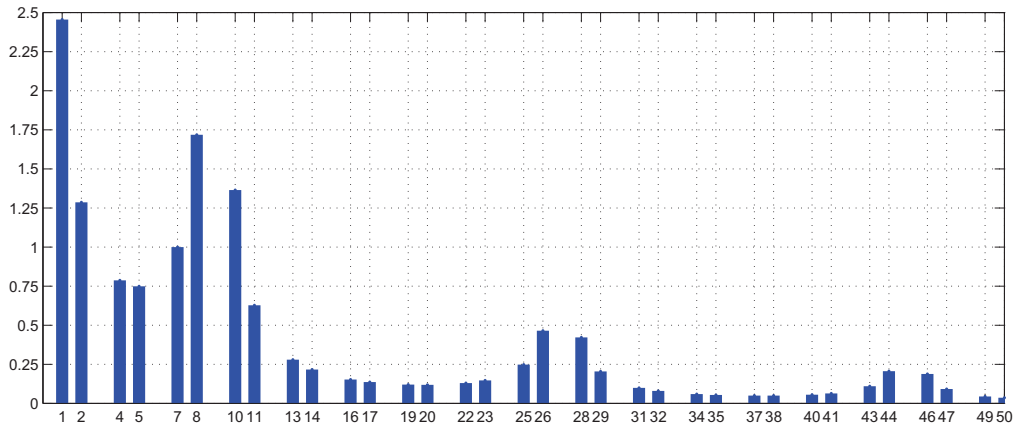

(a) Single Layer

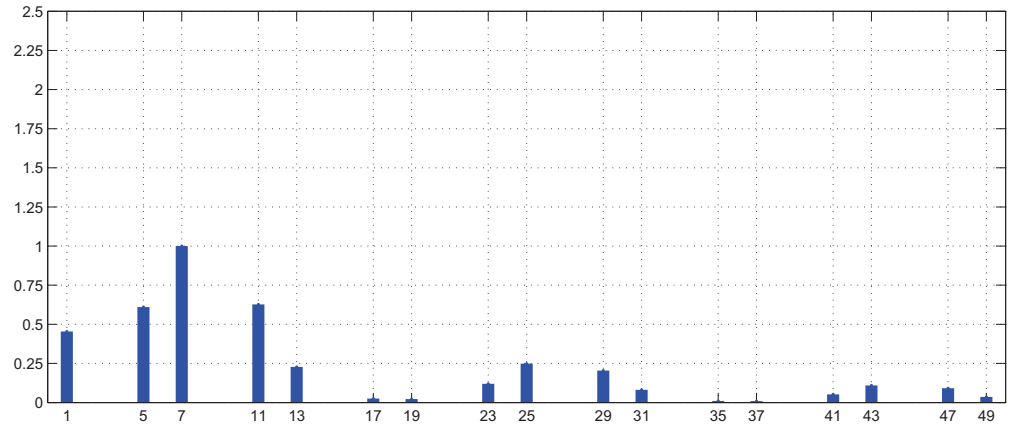

(b) Double Layer

Figure 2.4: Per unit stator MMF harmonic content of a 18-slot, 14-pole non-overlap winding PM machine.

where $p = \frac{2p_p}{M_s}$ is the number of poles per machine section and k_{dmn} is the n_r^{th} order magnet distribution factor given by [note that the phase difference between magnet coil voltages $= \frac{2\pi n_r}{p} + \pi$]

$$k_{dmn} = \left\{ \begin{array}{ll} 1 & n_r = \frac{(1+2j)p}{2} \\ & \\ 0 & n_r \neq \frac{(1+2j)p}{2} \end{array} \right\} \text{ with } j \in \mathbb{N}_0. \tag{2.27}$$

A winding factor, k_{wmn}, similar to (2.16) for the stator coils, can now also be defined for the magnets as

$$k_{wmn} = k_{dmn} k_{pmn}. \tag{2.28}$$

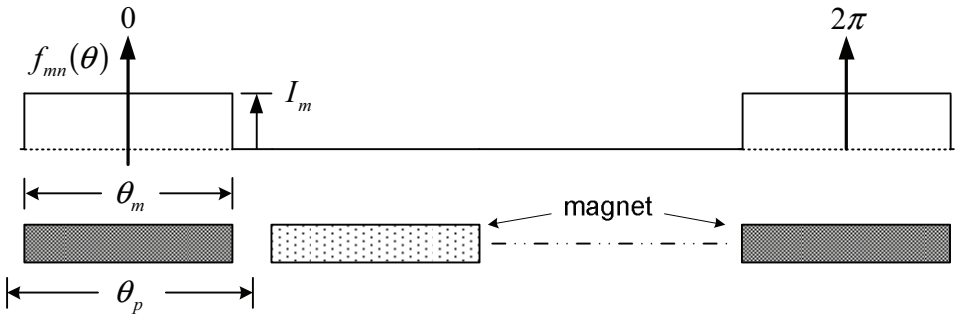

Figure 2.5: MMF generated by a magnet coil in a machine section.

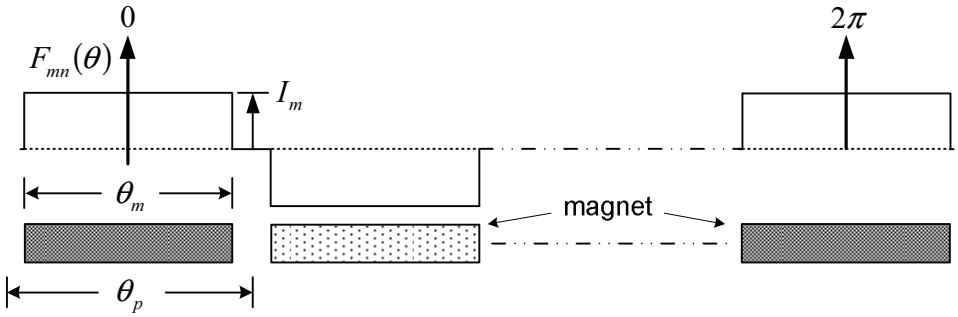

Figure 2.6: MMF generated by multiple magnet coils in a machine section.

2.3.1 Case Studies

The rotor MMF of the 18-slot, 14-pole PM machine, studied in Fig. 2.4, is analysed to find the rotor PM MMF harmonics, and to see what the influence is on these harmonics when the magnet pitch (θ_m) is adjusted. The magnet pitch is defined as a p.u. value, σ_m, using the pole pitch, θ_p, as the base value as

$$\sigma_m = \frac{\theta_m}{\theta_p}. \tag{2.29}$$

Substituting (2.29) into (2.25), k_{pmn} becomes

$$k_{pmn} = \sin\left(\frac{n_r \sigma_m \theta_p}{2}\right). \tag{2.30}$$

From (2.30) it is evident that certain rotor MMF harmonics can be eliminated by changing the value of σ_m, resulting in k_{pmn} being zero. It is found that to eliminate a certain harmonic n_r, σ_m needs to be set equal to $1 - \frac{p}{2n_r}$.

In Fig. 2.7 the magnet pitch is set equal to the pole pitch, $\sigma_m = 1$, and all harmonics denoted by n_r are present. The magnet pitch is then varied to $\sigma_m = \frac{6}{7}$, $\frac{4}{5}$ and $\frac{2}{3}$ p.u. in Figs. 2.8, 2.9 and 2.10 respectively. From the harmonic analysis of these MMF wave forms it can be seen that certain harmonics do not exist when the magnet pitch is adjusted appropriately. Note further

the effect of σ_m on the amplitude of the working harmonic MMF. A slight reduction in the working harmonic amplitude is noted when the magnet pitch is decreased.

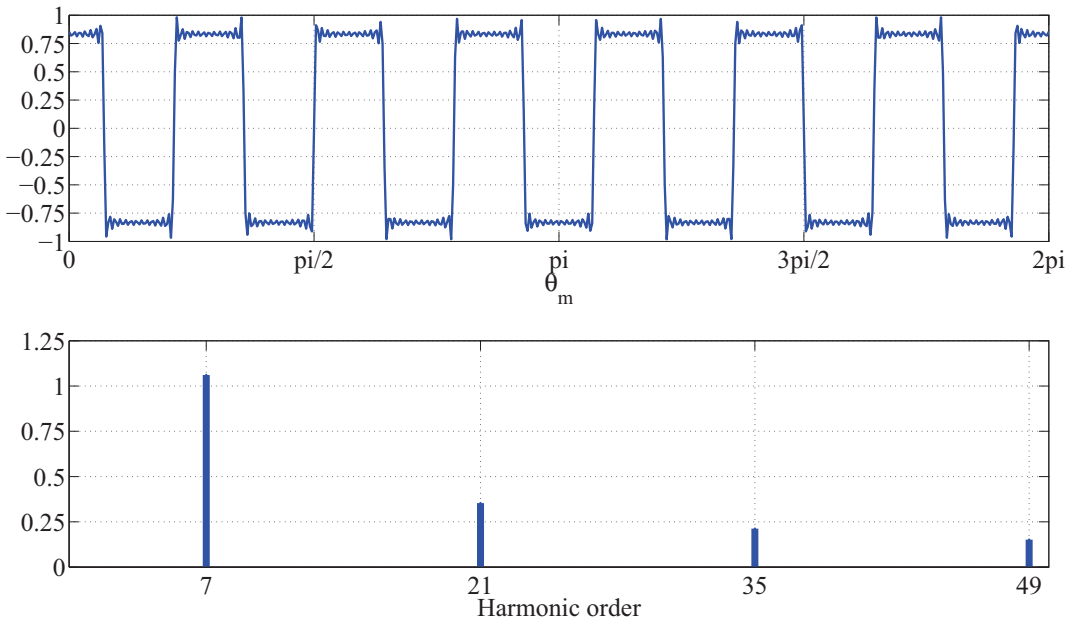

Figure 2.7: Per unit magnet MMF waveform and harmonic content of a 18-slot, 14-pole PM machine with $\sigma_m = 1$.

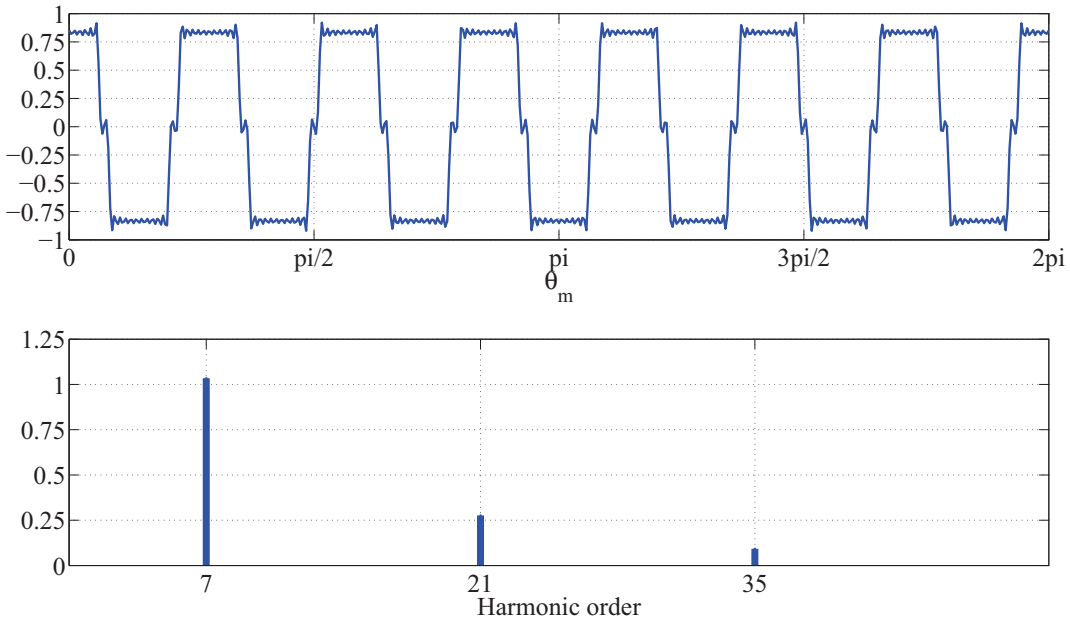

Figure 2.8: Per unit magnet MMF waveform and harmonic content of a 18-slot, 14-pole PM machine with $\sigma_m = \frac{6}{7} = 0.857$.

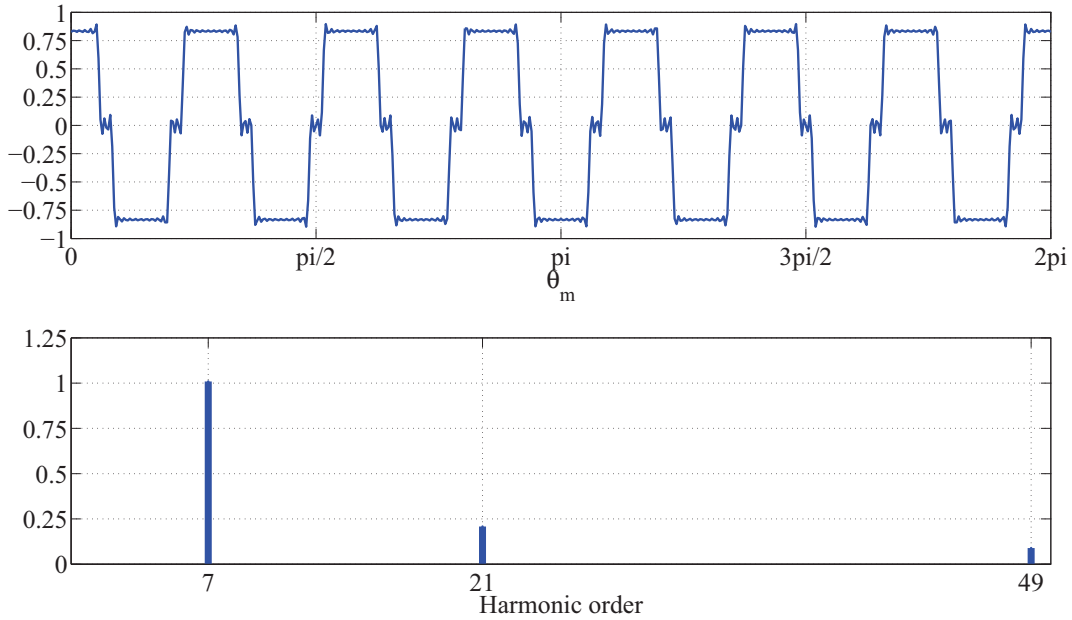

Figure 2.9: Per unit magnet MMF waveform and harmonic order of a 18-slot, 14-pole PM machine with $\sigma_m = \frac{4}{5} = 0.8$.

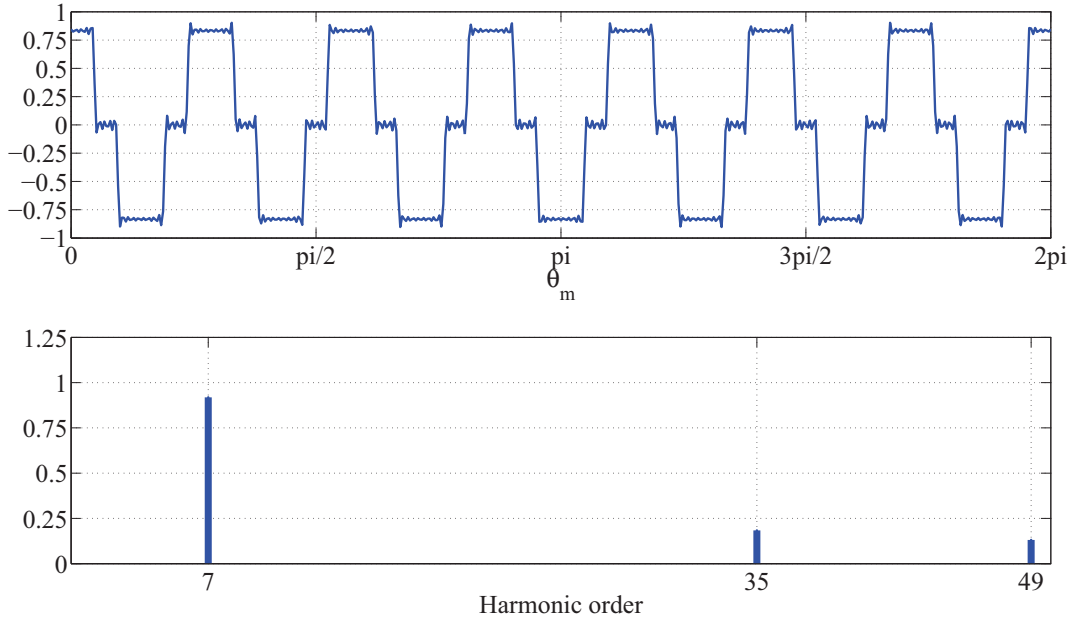

Figure 2.10: Per unit magnet MMF waveform and harmonic content of a 18-slot, 14-pole PM machine with $\sigma_m = \frac{2}{3} = 0.667$.

2.4 Travelling MMF harmonics

The velocity at which the stator MMF harmonics travel relative to the magnet coils is required to calculate the voltage induced in these coils. Similarly, the velocity at which the rotor MMF harmonics travel relative to the stator is required to calculate the voltage induced in the stator windings. These induced voltages will be the basis of the torque calculation explained in the

sections to follow.

The electrical angular velocity in rad/s of the rotor MMF harmonics, with respect to the stator, is ω_r, and all the harmonics travel in the same direction and at the same velocity in the air gap. The rotor MMF harmonic's angular velocity ω_r is expressed as

$$\omega_r = \frac{2\omega}{pM_s}, \tag{2.31}$$

with ω being the electrical angular velocity of the stator current space phasor. The angular velocity of the stator MMF harmonics in rad/s in the air gap is given by

$$\omega_{sn} = \frac{\omega}{n_s M_s} \qquad n_s = 3\tau k - 1, \quad k \in \mathbb{Z}\,. \tag{2.32}$$

In (2.32) τ is an indication of whether the machine has positive or negative periodicity and the sign of n_s indicates the direction of the travelling wave.

2.5 Relative MMF velocity

Each MMF air gap harmonic causes a harmonic flux density that travels in the air gap, which induces voltages in both the stator and fictitious rotor magnet windings. In this section expressions for the angular velocity[4] of these harmonics relative to the stator or rotor are given, to be used in Sections 2.6 - 2.8.

2.5.1 Rotating stator MMF

All stator MMF harmonics travel at an electrical angular velocity of ω_{sn} relative to the stator current space phasor. The stator MMF harmonics also travel at an electrical angular velocity ω_{rn} relative to the rotor magnet windings, which is given by

$$\begin{aligned}\omega_{rn} &= \left(\frac{\omega_{sn} - \omega_r}{\omega_{sn}}\right)\omega \\ &= \left(1 - \frac{2n_s}{p}\right)\omega\,.\end{aligned} \tag{2.33}$$

2.5.2 Rotating rotor MMF

The rotor MMF harmonics given by (2.26) travels at an electrical angular velocity ω_r. The position of the MMF waveform now changes with $n_r(\omega_r t + \theta)$ instead of just $n_r\theta$. Substituting ω_r with (2.31), (2.26) becomes

$$F_{rn} = \frac{2I_m p k_{wmn}}{n_r \pi} \cos\left[n_r\left(\frac{2\omega t}{M_s p} + \theta\right)\right]. \tag{2.34}$$

[4]The relative angular velocity of the MMF's associated air gap flux density, induces a voltage that has an angular frequency equal to the velocity of the specific MMF.

This implies that the velocities of the rotor MMF harmonics relative to the stationary stator will be

$$\omega_s = \frac{2n_r}{M_s p}\omega \ . \tag{2.35}$$

2.6 Torque harmonics due to the stator MMF

A method to calculate the instantaneous torque due to the stator MMF is presented in this section. The induced voltage in the magnet coils is calculated and used to determine the AC power which is used in turn to calculate the pulsating torque.

The stator MMF generates the n_s^{th} harmonic air gap flux density from (2.20) as

$$b_{sn} = \frac{\mu_0 F_{sn}}{g k_c} \ , \tag{2.36}$$

where the Carter factor, k_c, is used with the air gap dimension, g, to obtain the effective air gap dimension. The air gap flux density with respect to the stationary stator is then,

$$b_{sn} = \frac{3\tau u N I}{\pi |n_s|}\frac{\mu_0}{g k_c} k_{wsn} \sin(\omega t + n_s\theta) \ . \tag{2.37}$$

With respect to the rotor the flux density is

$$b_{rn} = \frac{3\tau u N I}{\pi |n_s|}\frac{\mu_0}{g k_c} k_{wsn} \sin(\omega_{rn} t + n_s\theta) \ , \tag{2.38}$$

with θ now referring to the rotor. The frequency ω_{rn} is given by (2.33). Equation (2.38) can be simplified as

$$b_{rn} = B_{rn} \sin(\omega_{rn} t + n_s\theta) \ , \tag{2.39}$$

with

$$B_{rn} = \frac{3\tau u N I}{\pi |n_s|}\frac{\mu_0}{g k_c} k_{wsn} \ . \tag{2.40}$$

Now consider all the magnet coils as a series connected single phase winding (like a phase group non-overlap winding) as shown in Fig. 2.11. The amplitude of the n_s^{th} order induced magnet coil voltage of all the coils in series in a machine section, is calculated in A.1 and is given by

$$E_{mn} = \frac{3\tau u \mu_0 p l d_g N I}{\pi n_s^2 M_s g k_c} k_{wsn} k_{pmn} k_{dmn} |\omega_{rn}| \ , \tag{2.41}$$

where the distribution factor k_{dmn} is given by (2.27) for n_r^{th} harmonic order. In this case, however, the n_s^{th} harmonic order is used instead, to get the value for k_{dmn}. The distribution factor k_{dmn} now only has a non-zero value when $n_r = n_s$.

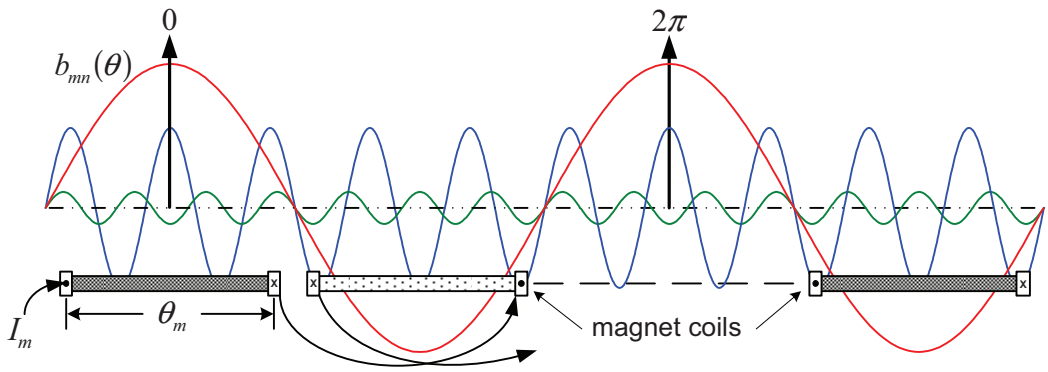

Figure 2.11: Magnet coils in a harmonic magnet field

The induced voltage in a magnet coil section, due to the n_s^{th} order stator flux density harmonic, is given by

$$e_{mn} = E_{mn}\cos(\omega_{rn}t). \tag{2.42}$$

The instantaneous power of the machine due to the interaction of the n_s^{th} order stator flux density harmonic and the magnet coil currents is given by

$$p_{mn} = e_{mn}I_m M_s, \tag{2.43}$$

while the torque at a rotor speed of ω_r is

$$\begin{aligned} T_{mn} &= \frac{e_{mn}I_m M_s}{\omega_r} && (2.44)\\ &= \frac{pe_{mn}I_m M_s^2}{2\omega} && (2.45)\\ &= \frac{3\tau u\mu_0 pld_g NII_m M_s}{2\pi n_s^2 g k_c}k_{wsn}k_{wmn}|\omega_{rn}|\cos(\omega_{rn}t) && (2.46)\\ &= \frac{3\tau u\mu_0 pld_g NII_m M_s}{2\pi n_s^2 g k_c}k_{wsn}k_{wmn}|p-2n_s|\cos\left[\omega t\left(\frac{p-2n_s}{p}\right)\right]. && (2.47) \end{aligned}$$

This results in torque pulsations with frequencies of multiples of 6 times the stator current frequency. Note that the working MMF stator harmonic ($n_s = p/2$) generates no torque as the induced voltage in the magnet coils is zero.

2.7 Torque harmonics due to the rotor MMF

Similar to what was done in Section 2.6 the induced voltage in the stator windings due to the rotor MMF is calculated. The induced voltage is then used to calculate the torque of the machine.

Similar to what was calculated (2.36) the rotor MMF given by (2.26) generates the n_r^{th} harmonic air gap flux density as

$$b_{rn} = \frac{\mu_0 F_{mn}(\theta)}{g k_c} . \tag{2.48}$$

While the rotor is turning at an angular velocity of ω_r, the air gap flux density with respect to the stationary stator is given by (2.49) (similar to (2.34), ω_r is substituted with (2.31)).

$$b_{sn} = \frac{2\mu_0 p I_m k_{wmn}}{n_r \pi g k_c} \cos\left(\frac{2n_r \omega t}{M_s p} + n_r \theta\right) , \tag{2.49}$$

with θ now referring to the stator. The flux density can then be written as

$$b_{sn} = B_{sn} \cos\left(\frac{2n_r \omega t}{M_s p} + n_r \theta\right), \tag{2.50}$$

with the amplitude B_{sn} given in (2.51).

$$B_{sn} = \frac{2\mu_0 p I_m k_{pmn} k_{dmn}}{n_r \pi g k_c}. \tag{2.51}$$

The amplitude E_{sn} of the induced phase voltage in the stator winding due to the rotor flux density as calculated in A.2, is given by

$$E_{sn} = -k_{dsn} k_{psn} \frac{16 u \omega N l d_g B_{sn}}{n_r p M_s}. \tag{2.52}$$

Assuming a three-phase machine and only q-axis current, i.e. the phase currents are in phase with the phase voltages, we have the following expressions for the phase currents and phase voltages:

$$[e_{abc(n)}] = \begin{bmatrix} E_{sn} \sin\left(\frac{2n_r}{M_s p}\omega t\right) \\ E_{sn} \sin\left(\frac{2n_r}{M_s p}\omega t - \frac{2\pi}{3}\right) \\ E_{sn} \sin\left(\frac{2n_r}{M_s p}\omega t + \frac{2\pi}{3}\right) \end{bmatrix}, \tag{2.53}$$

$$[i_{abc}] = \begin{bmatrix} I \sin(\omega t) \\ I \sin(\omega t - \frac{2\pi}{3}) \\ I \sin(\omega t + \frac{2\pi}{3}) \end{bmatrix}, \tag{2.54}$$

where I is the peak value of the phase currents.

Assuming a sinusoidal phase current and harmonic induced voltage given by $e_{abc(n)}$, the instantaneous developed torque T_s can be expressed from the instantaneous developed power as

$$T_s = \frac{p M_s}{2\omega} \sum_{n_r} [i_{abc}]^T [e_{abc(n)}]. \tag{2.55}$$

Substituting $[i_{abc}]$ and $[e_{abc(n)}]$ in T_s and considering $n_r = 3\tau i \pm 1$ with $i \in \mathbb{N}_0$, results in[5]

$$T_s = \frac{3pMs}{2\omega} I E_{s(p/2)} + \sum_j I\left(E_{s(j+1)p/2} + E_{s(j-1)p/2}\right)\cos(j\omega t) \quad \text{with } j = 6, 12, 18, ... \tag{2.56}$$

From (2.52) the torque equation of (2.56) can then be expressed in terms of winding factors as

$$T_s = CI\left[k_{ws[p/2]}k_{wm[p/2]} + \sum_j \left(\frac{k_{ws[(j+1)p/2]}k_{wm[(j+1)p/2]}}{j+1} + \frac{k_{ws[(j-1)p/2]}k_{wm[(j-1)p/2]}}{j-1}\right)\cos(j\omega t)\right], \tag{2.57}$$

with

$$C = \frac{-48uNld_g\mu_0 pI_m}{\pi g k_c}\,, \tag{2.58}$$

where k_{wsn} and k_{wmn} of (2.16) and (2.28) are the respective winding factors of the stator and magnet coils. Equation (2.57) reduces to an equation for the average torque when only the working harmonic of the rotor flux density is considered. The average torque is then expressed as

$$T_{ave} = CIk_{ws[p/2]}k_{wm[p/2]}\,. \tag{2.59}$$

2.8 Torque harmonics taking stator slotting into account

The cogging torque in a PM machine due to the stator slots is modelled in this section. The modelling is based on calculating the AC power induced in the fictitious magnet coils.

2.8.1 Permeance harmonics due to stator slotting

The slotted stator causes a change in permeance in the air gap of the machine, which in turn causes a ripple in the air gap flux density of the machine. The change in the air gap permeance, for regularly spaced slots, can be represented by the square-shaped waveform of Fig. 2.12. In Fig. 2.12, Δ[6] is the change in the stator side air gap permeance due to the stator slotting. This permeance waveform is stationary in the air gap and is the cause of AC induced voltages in the rotating secondary permanent magnet coils. With constant current in the magnet coils, this implies that pulsation power is transferred to and from the rotor, specifically to and from the magnet coil current source. At a constant rotor speed this implies that pulsation torques will be generated, which represent the cogging torque of the machine.

[5]The average torque component is generated when $\frac{2n_r}{M_s p} = 1$. This happens when n_r is equal to the working harmonic of the machine.

[6]Δ is calculated based on the work done in [16]. Only the maximum change in permeance of the work done in [16] is considered and shown as Δ in Fig. 2.12.

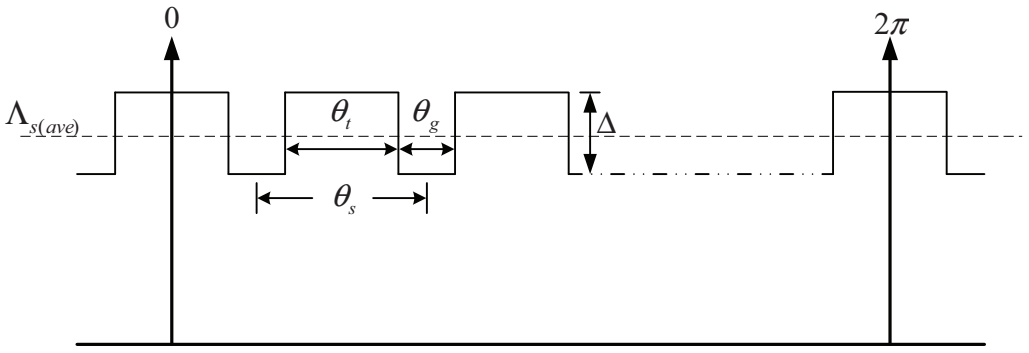

Figure 2.12: Air gap permeance distribution due to stator slotting.

To investigate and understand the cogging harmonic torques of the machine, the harmonics of the permeance waveform of Fig. 2.12 must be described. The waveform is repeated in every machine section having $S = \frac{N_s}{M_s}$ number of slots and teeth with respective widths of θ_g and θ_t. From Fourier series analysis , these slot permeance harmonics can be expressed as

$$\Lambda_s = \Lambda_{s(avg)} + \sum_{n_t} \frac{2\Delta S}{\pi n_t} k_{ptn} \cos(n_t \theta) \qquad n_t = vS, \quad v \in \mathbb{N}_1 \tag{2.60}$$

where k_{ptn} is a slot pitch factor of the n_t^{th} slot harmonic and given by

$$k_{ptn} = \sin\left(\frac{n_t \theta_t}{2}\right). \tag{2.61}$$

The saturation of the stator teeth along the machine section will vary and so will the tooth permeance. This will affect the permeance waveform of Fig. 2.12 and the flux density slotting harmonics. Hence, it can be expected that other slotting harmonics additional to the harmonics described will exist.

2.8.2 Torque harmonics due to stator slotting

The n_t^{th} air gap permeance harmonic due to the stator slots is given by (2.60), with respect to the stationary stator. Equation (2.60) can be referred to the rotor side as

$$\Lambda_r = \Lambda_{s(avg)} + \sum_{n_t} \frac{2\Delta S}{\pi n_t} k_{ptn_t} \cos\left(\frac{2n_t \omega t}{pM_s} + n_t \theta\right) \qquad n_t = vS, \quad v \in \mathbb{N}_1 \tag{2.62}$$

The flux density in the air gap due to the magnet MMF and the stator slots is given by

$$B_g = F_m \Lambda_r \ , \tag{2.63}$$

which from (2.26) and (2.62) becomes

$$B_g = F_m \Lambda_r \tag{2.64}$$

$$= \sum_{n_r} \frac{2pI_m k_{wmn_r}}{n_r \pi} \cos(n_r \theta) \left[\Lambda_{s(avg)} + \sum_{n_t} \frac{2\Delta S}{\pi n_t} k_{ptn_t} \cos\left(\frac{2n_t \omega t}{pM_s} + n_t \theta \right) \right] \tag{2.65}$$

$$= \frac{2pI_m}{\pi} \Lambda_{s(avg)} \sum_{n_r} \frac{k_{wmn_r}}{n_r} \cos(n_r \theta)$$

$$+ \frac{4pI_m \Delta S}{\pi^2} \left[\sum_{n_r} \frac{k_{wmn_r}}{n_r} \cos(n_r \theta) \sum_{n_t} \frac{k_{ptn_t}}{n_t} \cos\left(\frac{2n_t \omega t}{pM_s} + n_t \theta \right) \right]. \tag{2.66}$$

As only time varying[7] flux induces voltage, only the time varying flux density component of (2.66) has to be considered as

$$B_g^* = \frac{4pI_m \Delta S}{\pi^2} \left[\sum_{n_r} \frac{k_{wmn_r}}{n_r} \cos(n_r \theta) \sum_{n_t} \frac{k_{ptn_t}}{n_t} \cos\left(\frac{2n_t \omega t}{pM_s} + n_t \theta \right) \right]. \tag{2.67}$$

From (2.67) the amplitude of the n_t^{th} order induced magnet coil voltage (all coils considered in series) in a machine section is derived in Appendix A.3 as (A.27).

$$E_{mn} = \frac{4I_m \Delta S l d_g \omega}{\pi^2 M_s^2} \sum_{n_r} \frac{k_{wmn_r}}{n_r} \sum_{n_t} k_{ptn_t} \left[\left(\frac{1}{n_r + n_t} \right) \sin\left(\frac{(n_r + n_t)\theta_m}{2} \right) + \left(\frac{1}{n_r - n_t} \right) \sin\left(\frac{(n_r - n_t)\theta_m}{2} \right) \right], \tag{2.68}$$

With the instantaneous induced voltage given by (A.26) as

$$e_t = E_{mn} \sin\left(\frac{2n_t \omega t}{pM_s} \right). \tag{2.69}$$

The instantaneous power of the whole machine due to the n_t^{th} order stator slot permeance harmonic and the magnet coil current is given by

$$p_{mn} = e_t I_m M_s, \tag{2.70}$$

[7] θ refers to a position on the rotor, thus, when looking at a certain position on the rotor, although moving in relation to the stator, the value of θ stays constant with time.

with the torque at a rotor speed of ω_r then given by

$$\begin{aligned} T_{tn} &= \frac{e_t I_m M_s}{\omega_r} \\ &= \frac{p e_t I_m M_s^2}{2\omega} \\ &= \frac{2 I_m^2 \Delta S l d_g p}{\pi^2} \sum_{n_r} \frac{k_{wmn_r}}{n_r} \sum_{n_t} k_{ptn_t} \\ &\quad \left[\left(\frac{1}{n_r + n_t} \right) \sin \left(\frac{(n_r + n_t)\theta_m}{2} \right) + \left(\frac{1}{n_r - n_t} \right) \sin \left(\frac{(n_r - n_t)\theta_m}{2} \right) \right] \sin \left(\frac{2 n_t \omega t}{p M_s} \right). \end{aligned} \tag{2.71}$$

This results in torque pulsation with a frequency of $\frac{2n_t\omega t}{pM_s}$, in a balanced 3-phase machine.

2.8.3 Case study 1

A linear machine with 10 poles and 12 slots is modelled with FE software as shown in Fig. 2.13. The no-load air gap flux density of the analytical model (2.66) together with the FE results are shown in Fig. 2.14. The flux density is calculated with no current flowing in the stator coils, to eliminate the effect of the stator MMF. The harmonics present in the flux density wave forms of Fig. 2.14 are shown in Fig. 2.15. It is clear that there is good agreement between results of the proposed analytical method and FEA.

The harmonic orders in Fig. 2.15 are given by $|n_r \pm n_t|$ and travel at speeds of $\frac{2n_t\omega t}{S}$ with respect to the stator, with the direction of travel indicated by $sign(n_r \pm n_t)$. Plotting the real versus imaginary parts of some of these air gap flux density harmonics for one cycle of the working harmonic is shown in Fig. 2.16.

From the FE analysis the magnetic cogging force of the machine is shown in Fig. 2.17, together with the analytical calculation. The rotor of the machine is moved at a speed of 18 $m.s^{-1}$ to show the correlation between the FEA and the analytical method of torque calculation presented. Again, very good prediction of the cogging force is obtained from the anaytical method.

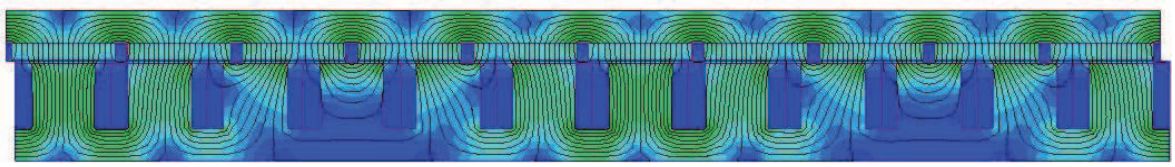

Figure 2.13: FE field solution for the 10-pole, 12-slot linear machine used for the case study.

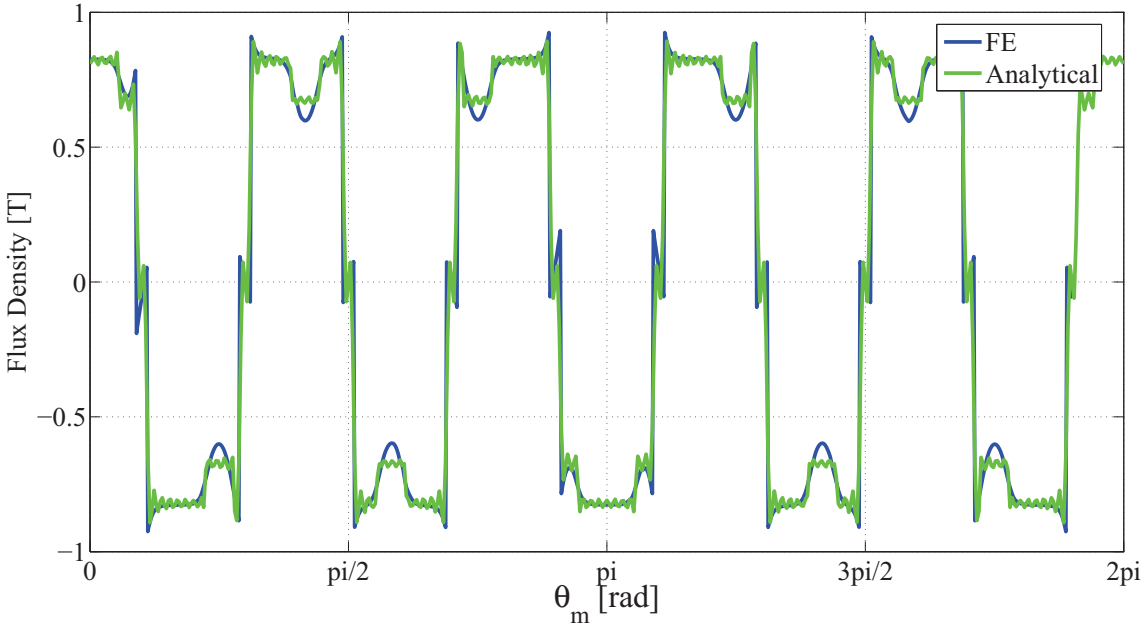

Figure 2.14: Analytical and FEA predicted air gap flux density due to the magnet MMF and stator slots of a 10-pole, 12-slot machine.

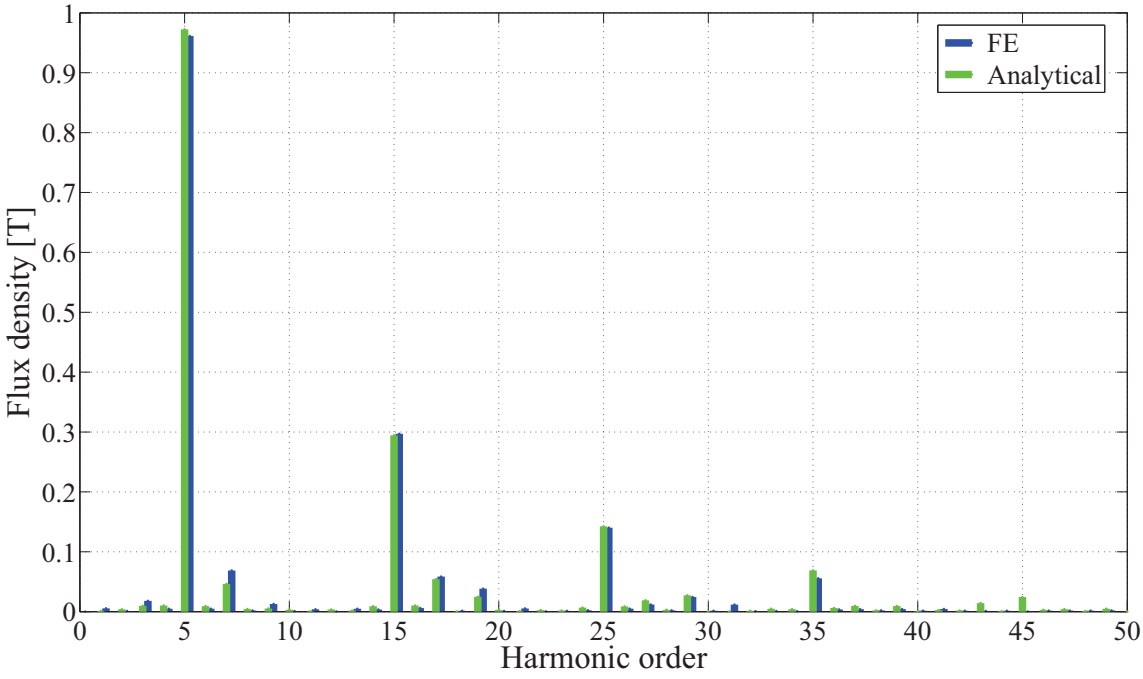

Figure 2.15: Analytical and FEA predicted air gap flux density harmonics due to the magnet MMF and stator slots of the 10-pole, 12-slot machine.

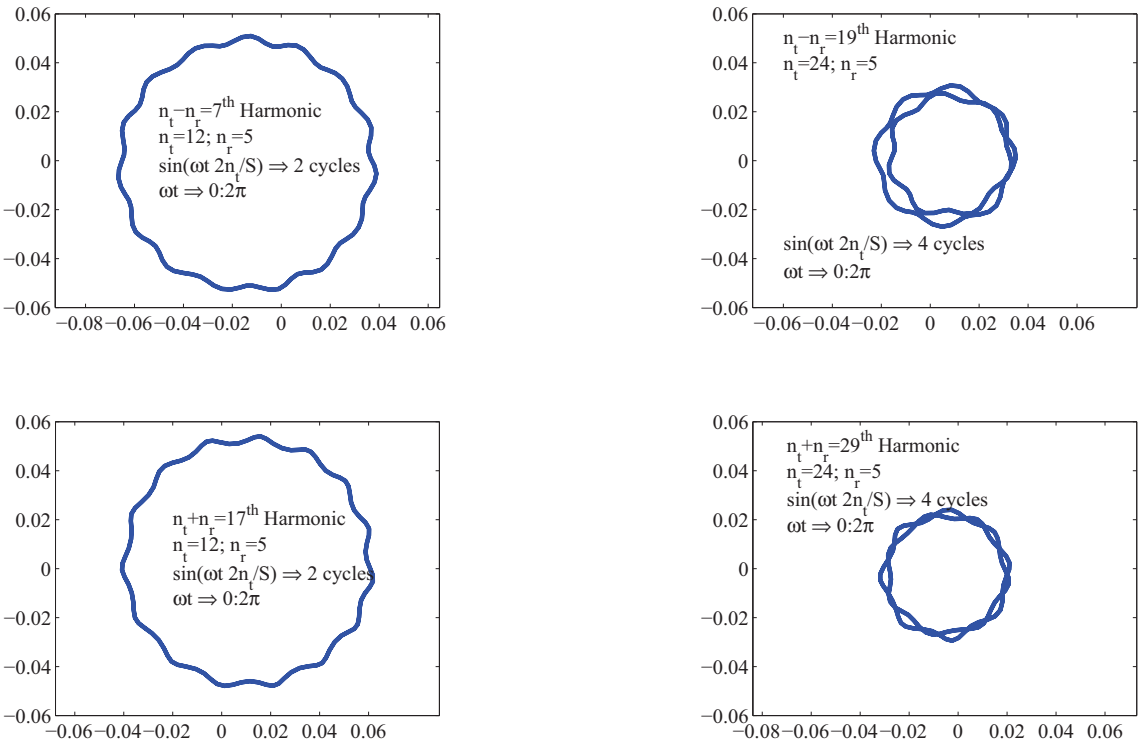

Figure 2.16: Analytical calculated real versus imaginary parts of some air gap flux density harmonics (7^{th}, 17^{th}, 19^{th} and 29^{th}) of the 10-pole, 12-slot machine.

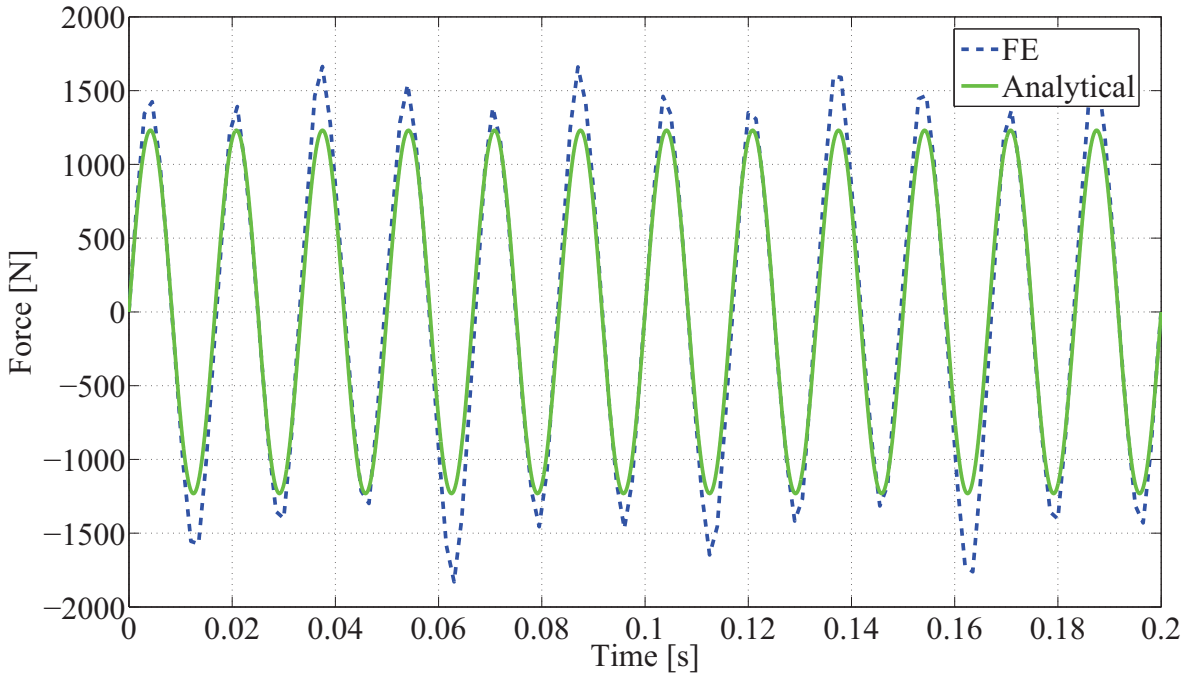

Figure 2.17: Analytical and FEA cogging force calculation of a 10-pole, 12-slot PM machine.

2.8.4 Case study 2

The cogging torque of the 40-pole, 30-slot PM machine discussed in Chapter 7[8] is calculated using the analytical method presented in this Chapter, similar to Case study 1. The model used for the FE prediction is shown in Fig. 2.18.

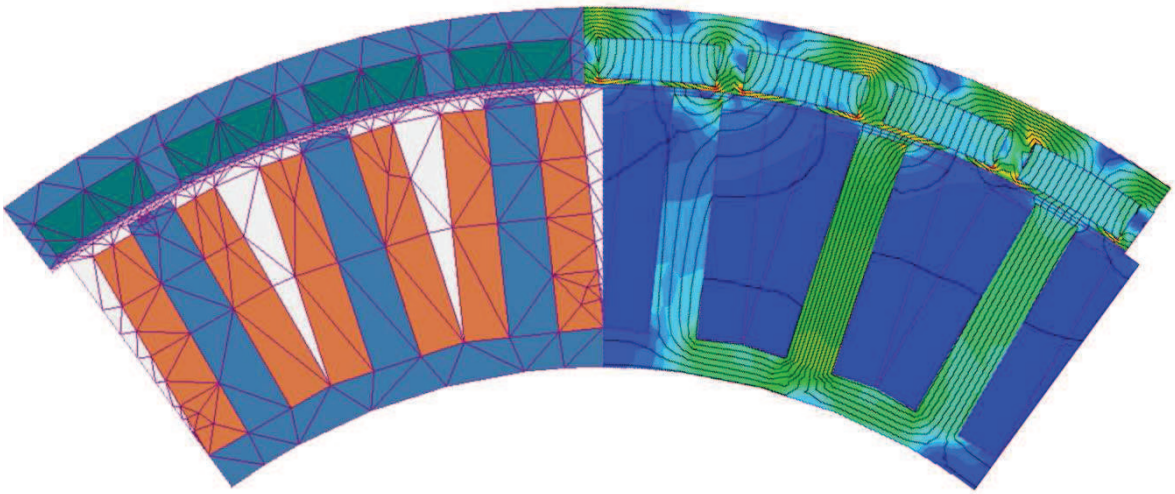

Figure 2.18: Section of the modeled 40-pole/30-slot PM machine.

The machine dimensions used in the analytical torque calculation are given in Table 7.1. Because the analytical model is only for surface mounted PMs, the thin iron pieces between the magnets and the iron sheet on the air gap side of the magnets, that is in the FE machine model, were taken as air in the analytical model. Even though there are differences in the analytical and FE machine models, the prediction of cogging torque, as shown in Fig. 2.19, still shows good correlation with the cogging torque calculated by the FEA program.

[8]The torque ripple of the PM hub machine is minimized in the optimization procedure as shown in Section 7.1.1.

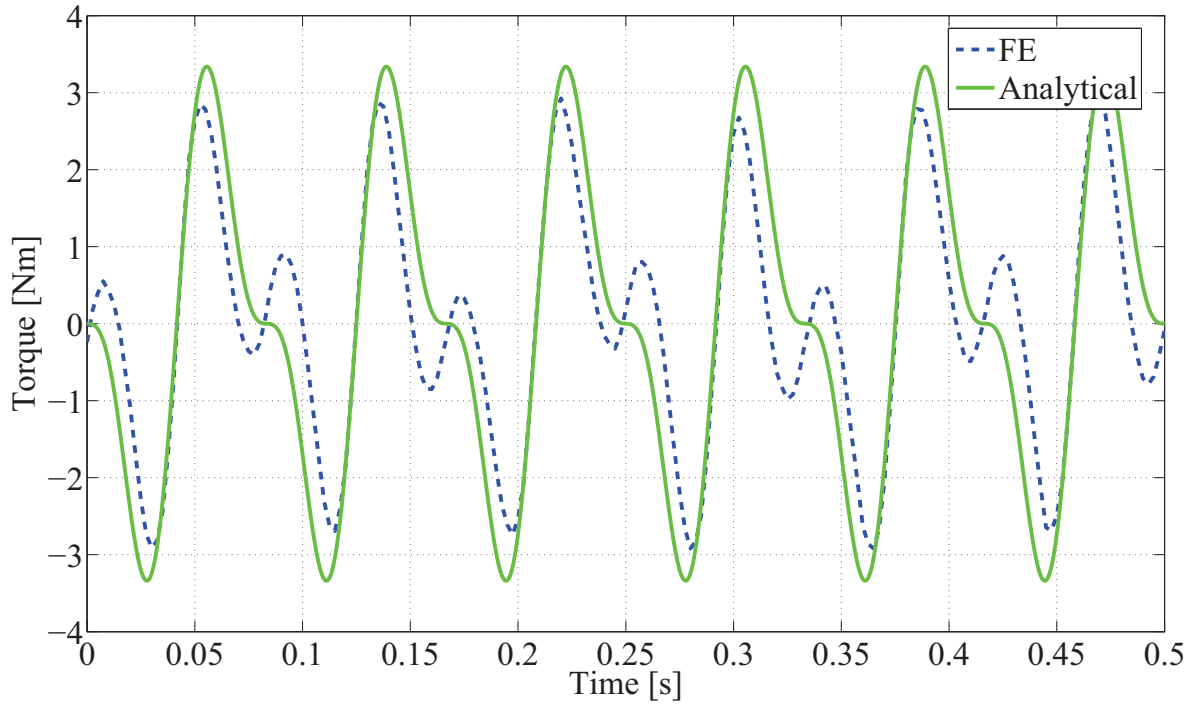

Figure 2.19: Analytical and FEA cogging torque calculation of a 40-pole, 30-slot PM machine.

2.9 Conclusion

In this Chapter stator MMF harmonics are mathematically described, not using complex analysis, for 3-phase PM machines with non-overlap windings having either negative or positive periodicity. It is shown that multiples of the 3^{rd} stator MMF harmonics do not exist in 3-phase machines and that stator MMF harmonics of even order do not exist when negative periodicity occurs.

It is shown that certain rotor MMF harmonics can be eliminated by changing the magnet pitch. This can be helpful in the process to minimize cogging torque. Three torque equations, for the three sources that generate torque ripple, are given in terms of winding factors. These equations can be used in the analytical performance calculations of concentrated coil machines with surface mounted magnets, when they need to be compared in terms of torque and torque ripple.

The analytical prediction of the cogging force and torque is in good agreement with FE analysis and can be used in a first design iteration of concentrated-coil PM machines to minimize torque ripple and reduce optimization time. The harmonic orders of the MMF, flux density and torque is also mathematically explained in this chapter.

CHAPTER 3

MODELLING

In this chapter the equivalent circuits and equations, that describe the permanent magnet synchronous machine, are discussed. The *abc* space phasor model with the reference fixed to the stator is transformed to the $dq0$ space phasor model with the reference fixed to the rotor. This transformation, known as Park's transformation, is used as in the steady state, the *d*- and *q*-axes values take on the form of DC values. The design optimization of the PM hub machine in Chapter 5 is then based on steady state $dq0$ values.

3.1 Equivalent dq circuit models

The general equation for the 3-phase stator voltage, $\mathbf{v}_{abc}$, of a PMSM in the *abc* reference frame is given by

$$\mathbf{v}_{abc} = r_s \mathbf{i}_{abc} + \frac{d\boldsymbol{\lambda}_{abc}}{dt}, \tag{3.1}$$

where $\mathbf{v}_{abc}$, $\mathbf{i}_{abc}$ and $\boldsymbol{\lambda}_{abc}$ are the stator voltage, current and flux linkage matrices respectively given by

$$\mathbf{v}_{abc} = \begin{bmatrix} v_a \\ v_b \\ v_c \end{bmatrix}, \qquad \mathbf{i}_{abc} = \begin{bmatrix} i_a \\ i_b \\ i_c \end{bmatrix} \qquad \text{and} \qquad \boldsymbol{\lambda}_{abc} = \begin{bmatrix} \lambda_a \\ \lambda_b \\ \lambda_c \end{bmatrix}. \tag{3.2}$$

The voltage matrix in (3.2) can then be transformed to a voltage vector-matrix, $\mathbf{v}_{dq0}$, in the $dq0$ reference frame using Park's transformation as

$$\mathbf{v}_{dq0} = \mathbf{k}_p \mathbf{v}_{abc}, \tag{3.3}$$

where $\mathbf{k}_p$ is Park's transformation matrix given by

$$\mathbf{k}_p = \frac{2}{3} \begin{bmatrix} \cos(\theta_r) & \cos\left(\theta_r + \frac{2\pi}{3}\right) & \cos\left(\theta_r - \frac{2\pi}{3}\right) \\ \sin(\theta_r) & \sin\left(\theta_r + \frac{2\pi}{3}\right) & \sin\left(\theta_r - \frac{2\pi}{3}\right) \\ \frac{1}{2} & \frac{1}{2} & \frac{1}{2} \end{bmatrix}. \tag{3.4}$$

The angle θ_r in (3.4) indicates the relative electrical rotor position, with the rotor's angular velocity given by $\omega = \frac{d\theta_r}{dt}$. From (3.1) and (3.3) the $\mathbf{v}_{dq0}$ voltages are given by

$$\mathbf{v}_{dq0} = \begin{bmatrix} v_d \\ v_q \\ v_0 \end{bmatrix} = r_s \begin{bmatrix} i_d \\ i_q \\ i_0 \end{bmatrix} + \frac{d}{dt} \begin{bmatrix} \lambda_d \\ \lambda_q \\ \lambda_0 \end{bmatrix} + \begin{bmatrix} -\lambda_q \\ \lambda_d \\ 0 \end{bmatrix} \omega \, . \tag{3.5}$$

For the steady state optimization the d- and q-axis currents are DC values so that

$$\frac{d\lambda_d}{dt} = \frac{\partial \lambda_d}{\partial i_d}\frac{di_d}{dt} = 0 \qquad \text{and} \qquad \frac{d\lambda_q}{dt} = \frac{\partial \lambda_q}{\partial i_q}\frac{di_q}{dt} = 0. \tag{3.6}$$

When (3.6) is substituted into (3.5), the steady state voltage equations are given by

$$\mathbf{V}_{dq0} = \begin{bmatrix} V_d \\ V_q \\ V_0 \end{bmatrix} = r_s \begin{bmatrix} I_d \\ I_q \\ I_0 \end{bmatrix} + \omega \begin{bmatrix} -\lambda_q \\ \lambda_d \\ 0 \end{bmatrix} \tag{3.7}$$

$$= r_s \mathbf{I}_{dq0} + \omega \boldsymbol{\lambda}_{dq0} \, . \tag{3.8}$$

For a balanced 3-phase system, these equations reduce to just dq models, since $V_0 = 0$. The flux linkages λ_d and λ_q include the end-winding flux linkage λ_e, the leakage flux linkage λ_l and the fundamental stator winding air gap flux linkage λ_m. The d-axis flux linkage also includes the flux linkage due to the PMs, λ_{PM}. These flux linkages are incorporated in the equivalent circuits as shown in Fig. 3.1, where E_d and E_q are the induced stator voltages due to the fundamental dq flux linkages.

3.2 Equivalent dq circuit parameters

In this section the calculation of the different dq circuit parameters of Fig. 3.1 are considered.

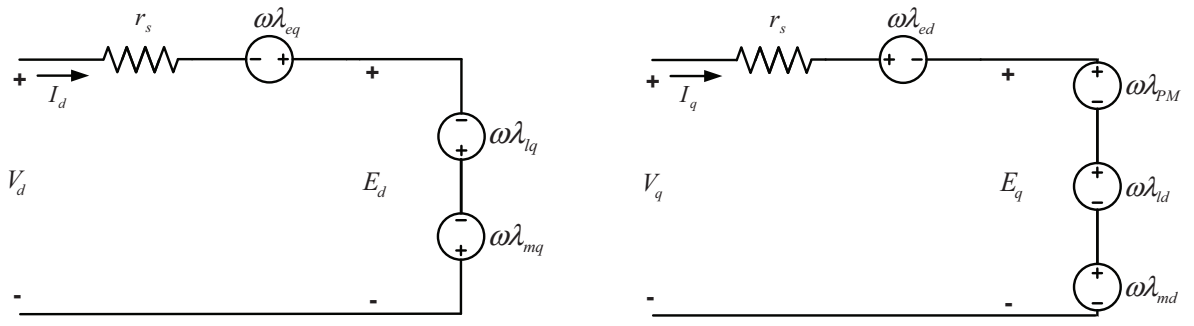

(a) $d-$ axis (b) $q-$ axis

Figure 3.1: Steady-state equivalent circuits of the PMSM.

3.2.1 Phase resistance r_s

The phase winding resistance r_s in Fig. 3.1 is calculated by

$$r_s = \frac{2N\rho_t(l + l_e)}{n_a \frac{A_{cu}}{z}}, \tag{3.9}$$

where n_a is the number of parallel circuits, N the number of turns in series per phase, l the active length of the machine with l_e being the average end-winding length, A_{cu} is the copper area in a slot and z is the number of conductors in a slot. When calculating the copper area from the slot dimensions, provision is made for the filling of the slot by using a fill factor. This fill factor also takes the areas of slot insulation and conductor insulation into account. The resistivity, ρ, of copper is a function of temperature, which at a copper temperature t_c, is given by

$$\rho_t = \rho_{20}\big[1 + \Upsilon_t(t_c - 20)\big], \tag{3.10}$$

where $\rho_{20} = 17 \times 10^{-9}\ \Omega m$ and $\Upsilon_t = 0.0039\,^{\circ}\mathrm{C}^{-1}$.

3.2.2 Equivalent current I_d and I_q

The allowed rated copper loss in the PM hub machine is a function of the cooling system design. The known rated copper loss is used as an input parameter to the machine design[9]. With the I^2R copper losses P_{cu} of the 3-phase machine known, the peak-value of the phase current, I, can be calculated by

$$I = \sqrt{\frac{2P_{cu}}{3r_s}}. \tag{3.11}$$

The current space phasor $\mathbf{I_s}$ is then calculated by

$$\mathbf{I_s} = I\angle\phi = I_q + jI_d \quad \text{with} \tag{3.12}$$

$$I_q = I_s\cos(\phi) \quad \text{and} \tag{3.13}$$

$$I_d = I_s\sin(\phi), \tag{3.14}$$

where ϕ is the angle measured from the q-axis as shown in Fig. 3.2. With the phase current known, the current density, J, in a stator slot can be calculated by

$$J = \frac{Iz}{A_{cu}n_a}. \tag{3.15}$$

The current density value is a good indicator, for quick reference, of the copper loss and the associated heat developed in the slot.

[9]The copper loss is a function of the cooling system and in this case specified by the engineers doing the cooling system design.

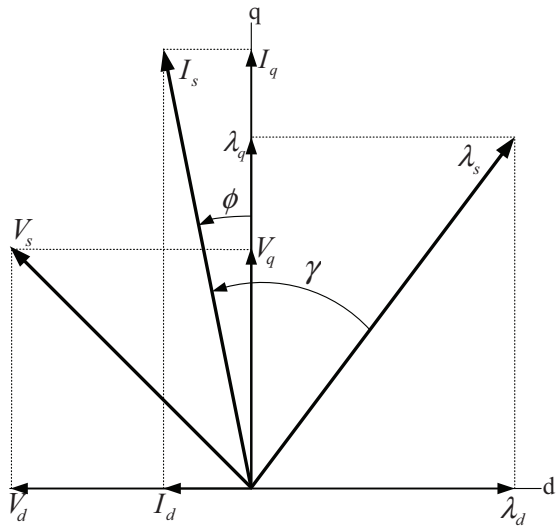

Figure 3.2: Space phasor diagram fixed in the rotor reference frame.

3.2.3 End-winding leakage inductance L_e

The end-winding leakage inductance is analytically calculated by [70]. For this calculation the inductance formula of an intermediate thick air-cored circular coil with rectangular cross section is used. The two half circle end-windings of the iron-cored non-overlap coil are combined, as shown in Fig. 3.3, to form an air-cored cylinder-shaped coil. The mean radius of this cylinder is a, while the axial and radial dimensions are respectively represented by b and c. The end winding inductance is then given by

$$L_e = 0.019739\left(\frac{2a}{b}\right)N^2 aK' \quad [\mu H], \tag{3.16}$$

where N is the number of turns in series per phase and K' a constant. The value of the K' is the difference $(K - k)$ of two quantities. Of these K is the constant in Nagaoka's formula for

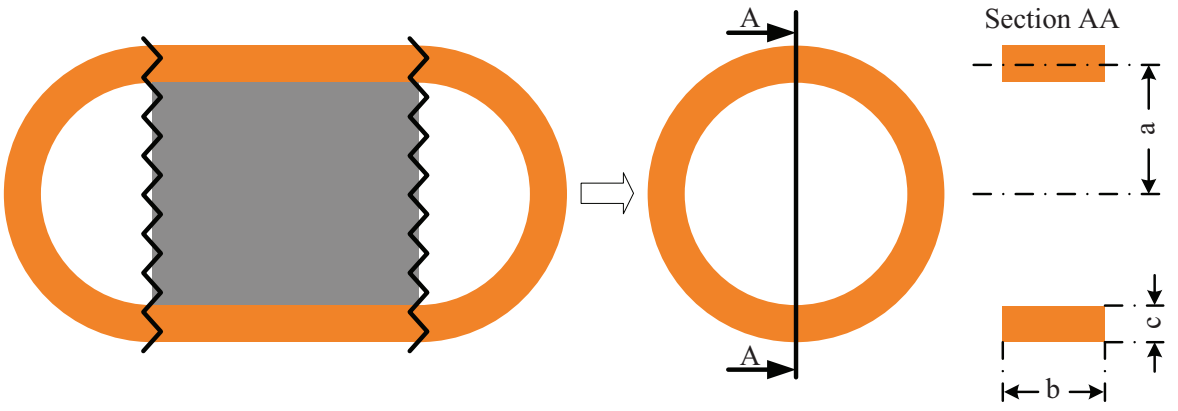

Figure 3.3: End-winding model to calculate the inductance L_e.

a solenoid and is tabulated as a function of $\frac{b}{2a}$ in Table C.1, as shown in [70]. The constant k takes into account the decrease of inductance due to the separation of the turns in the radial direction and the values are shown in Tables C.2 and C.3. The dimension of a in (3.16) needs to be in centimetres to give an inductance value in micro Henry.

The dq end-winding flux linkage, shown in Fig. 3.1, is calculated by using the dq currents and the calculated end-winding inductance as

$$\lambda_{ed} = L_e I_d \quad \text{and} \quad \lambda_{eq} = L_e I_q. \tag{3.17}$$

3.2.4 Air gap flux linkage and associated dq inductances

A non-commercial FE analysis package is used to calculate the air gap flux linkage in this section and is based on the macro air gap element of [71]. The flux linkage of a phase winding (take in this case phase a) is calculated by using a first-order triangular mesh in the FE analysis and solving for the magnetic vector potential A and integrating along the coil paths. With only a section of the machine meshed, the phase flux linkage, excluding the end-winding flux linkage λ_e, is calculated by

$$\lambda_a = \frac{2pzl}{n_a S} \sum_{j=1}^{y} \left(\frac{\Delta_j \zeta}{3} \sum_{i=1}^{3} A_{ij} \right) \tag{3.18}$$

where A_{ij} is the value of the magnetic vector potential of nodal point $i = 1, 2$ or 3 of the triangular element j. $\zeta = \pm 1$ gives the direction of integration with Δ_j the area of the triangular element j. The total number of elements of the meshed coil areas of the phase in the pole region is presented by y. The coil-area, S, the length, l, and the number of poles, p, are, amongst other things, necessary to implement the integration in the finite element program. The end-winding flux linkage component of phase a, $\lambda_{e(a)}$, is not included in the 2-D solution of (3.18), but is calculated separately as in (3.16) as $\lambda_{e(a)} = l_e i_a$. To verify the flux linkage calculation of the non-commercial FE package, it is compared to a commercial package, Magnet from Infolytica. The results, comparing the flux linkage of one phase, are shown in Fig. 3.4. The small difference can be attributed to the magnet modelling and the difference in the type of lamination steel used in the two programs.

The effect of skew is accounted for in the 2-D finite element solution by dividing the machine into a set of un-skewed machines of which the rotors are relatively displaced at an angle that is a fraction of the total skew. With k un-skewed machines the phase flux linkages are calculated by (3.19). The flux linkages of the un-skewed machine with the rotor at position α_n are denoted by $\lambda_{abc}(\alpha_n)$ and are calculated by (3.18).

$$\boldsymbol{\lambda}_{abc} = \frac{1}{k} \left[\sum_{n=1}^{k} \lambda_{abc}(\alpha_n) \right] \tag{3.19}$$

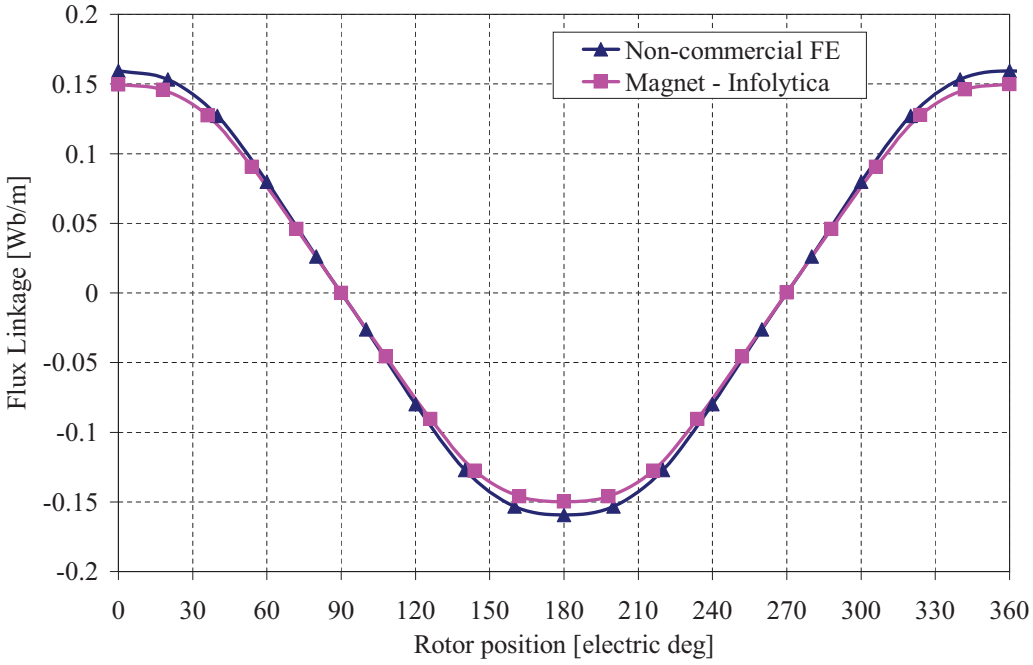

Figure 3.4: The flux linkage of a single phase, for the 40-pole 30-slot machine discussed in Chapter 7, is shown calculated using the non-commercial FE package together with the calculation done with a commercial package, Magnet of Infolytica.

With the phase flux linkages and the rotor position known, the dq flux linkages are calculated using Park's transformation as

$$\boldsymbol{\lambda}_{dq0} = \mathbf{k}_p \boldsymbol{\lambda}_{abc}. \tag{3.20}$$

The dq flux linkages[10] calculated in this way include the leakage flux, λ_l, of a coil so that

$$\lambda_d = \lambda_{md} + \lambda_{ld} + \lambda_{PM} \quad \text{and} \tag{3.21}$$

$$\lambda_q = \lambda_{mq} + \lambda_{lq}, \tag{3.22}$$

where λ_{PM} is generated by the PM. Figure 3.1 and equations (3.22) and (3.21) show λ_{md} and λ_{mq}, that is the stator winding air gap flux linkage. From this, the speed voltages $E_d = -(\lambda_{mq} + \lambda_{lq})\omega$ and $E_q = (\lambda_{md} + \lambda_{ld} + \lambda_{PM})\omega$ of the equivalent circuits of Fig. 3.1 are determined. The dq flux linkages can also be expressed as a space phasor, $\boldsymbol{\lambda_s}$, similar to the current in (3.12), as

$$\boldsymbol{\lambda_s} = \lambda_s \angle(\gamma - \phi) = \lambda_q + j\lambda_d \quad \text{with} \tag{3.23}$$

$$\lambda_q = \lambda_s \cos(\gamma - \phi) \quad \text{and} \tag{3.24}$$

$$\lambda_d = \lambda_s \sin(\gamma - \phi), \tag{3.25}$$

[10]It must be noted that due to the harmonics present in the PM hub motor the transformation of $\boldsymbol{\lambda}_{abc}$ could lead to small variations in the DC values of $\boldsymbol{\lambda}_{dq0}$.

(also see Fig. 3.2).

The d- and q-axis inductances L_d and L_q can be calculated in the FE analysis as

$$L_d = \frac{\lambda_{d(PM=0)}}{I_d} \quad \text{and} \quad L_q = \frac{\lambda_q}{I_q}\,, \tag{3.26}$$

by deactivating the PMs. Because the flux linkage due to the PM does not change with current, it should be subtracted from the d-axis flux linkage, if the value is known, to use in the inductance calculation as $L_d = \frac{\lambda_d - \lambda_{PM}}{I_d}$.

3.2.5 Equivalent voltage V_d and V_q

In this section the equivalent steady state d- and q-axis voltage of the PM hub motor is calculated. Similar to (3.12), the voltage space phasor shown in Fig. 3.2 is

$$\mathbf{V}_s = V_q + jV_d \quad \text{with} \tag{3.27}$$

$$V_q = I_q r_s + \omega(\lambda_{ed} + \lambda_{ld} + \lambda_{md} + \lambda_{PM}) \quad \text{and} \tag{3.28}$$

$$V_d = I_d r_s - \omega(\lambda_{eq} + \lambda_{lq} + \lambda_{mq})\,. \tag{3.29}$$

The voltage equations (3.28) and (3.29) are based on the steady state equivalent circuit of Fig. 3.1.

3.3 Electromagnetic torque

The average electro-magnetic torque, T_{ave}, that the PM hub motor produces is used in the design optimization, as discussed in Chapter 5. The torque ripple T_{rip} is calculated using a cycle of the instantaneous torque, T_{inst}, to find the maximum-, T_{max}, and minimum torque, T_{min}, values. The calculation of the various torque values is discussed in the following subsections.

3.3.1 Average torque

The average torque production of the PMSM can be written as the cross-product of the fundamental flux linkage space phasor, $\boldsymbol{\lambda_s}$, and the fundamental stator current space phasor, $\mathbf{I_s}$, i.e.

$$T_{ave} = \frac{3}{2} k \boldsymbol{\lambda_s} \times \mathbf{I_s}\,, \tag{3.30}$$

where k is a machine constant. Equation (3.30) can also be expressed from Fig. 3.2 as

$$T_{ave} = \frac{3}{2} k |\boldsymbol{\lambda_s}||\mathbf{I_s}| \sin(\gamma), \tag{3.31}$$

where $|\boldsymbol{\lambda_s}|$ and $|\mathbf{I_s}|$ are the respective magnitudes of the fundamental stator flux linkage and current space phasors. The angle γ is the torque angle, which is zero when the current space phasor coincides with the flux linkage space phasor. Equations (3.30) and (3.31) can be expressed in terms of dq-axis flux linkage and current components, as given by (3.23) and (3.12), for a p pole machine as

$$T_{ave} = \frac{3}{4} p(\lambda_d I_q - \lambda_q I_d) \, . \tag{3.32}$$

λ_{dq} and I_{dq} have been explained in previous sections. By using (3.26), (3.32) can then be expressed in the form

$$T_{ave} = \frac{3}{4} p\lambda_{PM} I_s \cos(\phi) + \frac{3}{8} p(L_d - L_q) I_s^2 \sin(2\phi). \tag{3.33}$$

The torque of the PMSM is a function of the flux linkage due to the magnets and the inductance difference $(L_d - L_q)$. Due to the inductance difference being relatively small for PMSM machines, compared to e.g. reluctances synchronous machines (RSM), the torque is mostly sensitive to the flux generated by the magnets.

3.3.2 Instantaneous torque

The Maxwell's stress tensor method is used to calculate the instantaneous electromagnetic torque at a certain rotor position of the PM machine accurately by [71],

$$T_{inst} = \frac{pr^2 l}{2\mu_0} \int_{\theta_1}^{\theta_2} B_r B_\theta d\theta \, , \tag{3.34}$$

where B_r and B_θ are the radial and tangential air gap flux density components. The machine's axial length is given by l, r is the air gap radius and p is the number of poles. The flux density components B_r and B_θ are calculated using the nodal magnetic vector potentials of the macro air gap element [71].

3.3.3 Torque ripple

The torque ripple and cogging torque (torque ripple at no load) of the machine are of special interest for in-wheel drives. The torque ripple of the machine is calculated as the difference in the peak to peak torque values and then expressed as a percentage of the average torque.

The torque ripple is calculated by position stepping the rotor in the FE analysis of the machine and calculating the instantaneous torque at every rotor position by using (3.34). This procedure generates a waveform of the instantaneous torque of the machine. This torque data

is processed to extract the minimum, maximum and average torque values. Once these values are known the torque ripple is calculated as

$$T_{rip} = \frac{T_{max} - T_{min}}{T_{ave}} \times 100\ \% \ . \tag{3.35}$$

CHAPTER 4

FREQUENCY LOSSES

Iron losses have been, and still are, an inportant topic in electrical machine design. The estimation and modeling of iron losses in PM machines, therefore, have received a lot of attention [26–39]. In literature fast analitycal or accurate FE methods are used to predict the different machine losses. A method of calculating the iron losses, magnet losses and stator copper eddy current losses that combines the analitycal method with information from FE analysis is presented in this Chapter.

The efficiencies of the optimized machines, discussed in Chapter 5, are compared to see what influence the design has on the machines' iron-, magnet- and eddy current losses. The losses calculated in this Chapter are not incorporated in the machine models given in Chapter 3. The equivalent circuit models of Chapter 3 are used in the optimization, and the losses are evaluated after the PM machines are optimized for the torque per copper loss performance.

The iron and eddy current losses in an electrical machine are defined in this chapter as frequency losses (P_f). These losses consist of the stator and rotor iron core losses (P_c), the eddy current losses in the stator conductors (P_s) and the eddy current losses in the permanent magnets (P_m), i.e.

$$P_f = P_c + P_s + P_m \,. \tag{4.1}$$

Since the various losses are caused by varying flux densities, these flux density variations are extracted at various points in the FE machine model during a time-stepped simulation. The information of the flux density variation is then used in the loss calculations. As an example, a slice of a FE machine model with the points indicated is shown in Fig. 4.1.

4.1 Iron losses

The specific iron loss p_c in W/kg is calculated with the machine steel under alternating flux conditions, and is separated into a hysteresis component (p_h) and an eddy current component (p_e) as in [14, 28] as

$$p_c = p_h + p_e = k_h f B^{\alpha} + k_e f^2 B^2 \,, \tag{4.2}$$

where f is the frequency and B is the peak value of the alternating flux density. The constants, k_h, k_e and α, can be obtained from the loss data of the steel provided by the manufacturer.

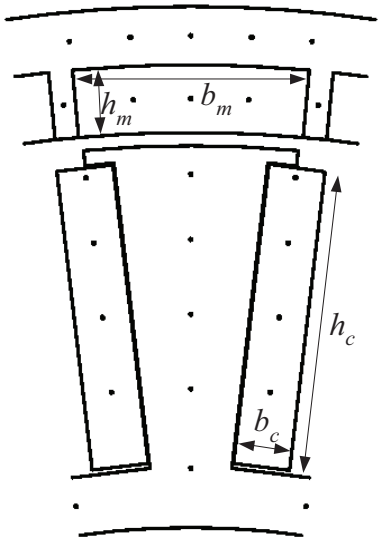

Figure 4.1: FE Machine section showing the points where flux density pulsations are calculated.

The calculation of the iron loss in this way may result in up to 20% lower values compared to measured values as stated in [29]. This is mainly due to non-sinusoidal flux density variations. Methods have been suggested by [28, 29] to compensate for these minor variations in the flux density. They are all based on analytical models. An improved iron loss formula is used by [28] that includes an excess or anomalous specific loss component (p_{exc}) as

$$p_c = p_h + p_e + p_{exc} \tag{4.3}$$

$$= k_h f B^{\alpha} + k_e f^2 B^2 + k_{exc} f^{1.5} B^{1.5} \,, \tag{4.4}$$

where k_{exc} is the excess loss constant. The eddy current loss constant is given by

$$k_e = \frac{\sigma \pi^2 w_s^2}{6\gamma} \,, \tag{4.5}$$

where σ is the conductivity of the material, w_s the lamination thickness and γ is the mass density of the laminations. With k_e known, a method of calculating the remaining constants, k_h, k_{exc} and α, from provided loss data becomes a mathematical operation as done by [72]. Manipulation of (4.4) results in a quadratic equation which is only frequency dependent as

$$\frac{p_c}{f} = k_h B^{\alpha} + k_e B^2 f + k_{exc} B^{1.5} \sqrt{f} \,. \tag{4.6}$$

This equation can be put in the general form as

$$\frac{p_c}{f} = a + b\sqrt{f} + c\left(\sqrt{f}\right)^2 \,, \tag{4.7}$$

where

$$a = k_h B^{\alpha} \,, \quad b = k_{exc} B^{1.5} \quad \text{and} \quad c = k_e B^2 \,. \tag{4.8}$$

Using basic curve fitting techniques on the provided loss data as in Fig. 4.2, the constants $k_h = 0.0139$ and $\alpha = 1.542$, are easily determined as single values, with $k_{exc} = 0.0007B + 0.0002$ being a linear function of the flux density amplitude.

The flux density variation in the iron parts of the machine, is extracted from the FE machine model at periodic intervals during a time stepped FE simulation. To simplify the analytical model of the loss calculation, the flux density variation at certain points in the machine model is assumed to be the same in a small region of the material around these points. Although radial flux density variations are present and are accounted for, only the tangential variation of flux density at different points in the rotor and stator yokes are shown in Fig. 4.3 as examples.

From Fig. 4.3 it can be deducted that the frequency components of the flux density in the rotor and stator iron are different. Flux density information extracted from the FE simulation can be used to obtain accurate information of the harmonic content[11]. The harmonic content of these flux density waveforms, shown e.g. in Fig. 4.4[12], is also described in Chapter 2, however,

[11] A discrete Fourier transform (DFT) is applied to the calculated flux density information to determine the frequency components (and amplitudes) of the flux density in a region.

[12] In Figs. 4.4, 4.6 and 4.8 the working harmonic of the PM machine is expressed as harmonic number one, while a DC value is harmonic number zero. Therefore, the harmonic order 1.5 would equate to 30 cycles per machine revolution for the 40-pole PM machine

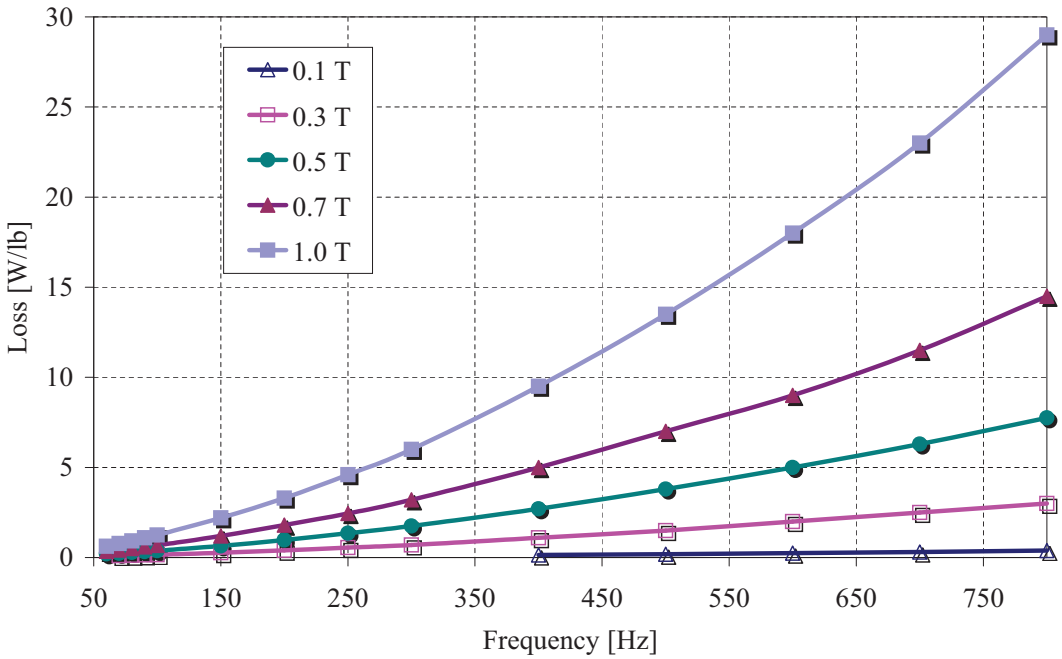

Figure 4.2: Loss data versus frequency provided by a manufacturer of M19 fully processed N-O Si-Fe 29 gauge (0.35 mm) sheet steel; the loss data are shown with flux density amplitude as a parameter.

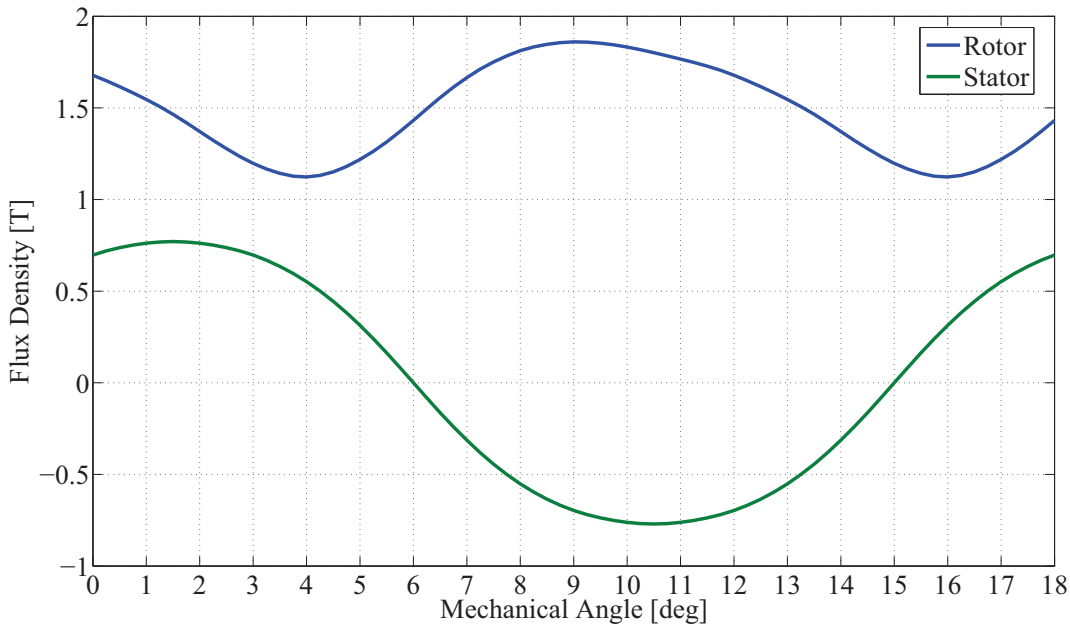

Figure 4.3: Tangential flux density variation at different points in the rotor and stator yokes of an optimized 40-pole, 30-slot machine with open stator slots.

the information from the FE simulation includes any saturation effects that might be present, which are ignored in the simple analytical model of Chapter 2.

4.2 Eddy current losses in the stator conductors

If a conductor is exposed to an alternating flux density field of frequency f and amplitude B, then the eddy current losses induced in that conductor are calculated by [73] as

$$P_s(n_c = 1) = \frac{\pi^3 l d^4 B^2 f^2}{8\rho}, \tag{4.9}$$

where l, d and ρ are respectively the length, diameter and resistivity of the conductor and n_c is the number of conductors exposed to the alternating field. The eddy current loss in the stator conductors due to the alternating stator conductor current can be taken into account by increasing the phase resistance R_s. This loss forms part of the I^2R copper loss, but is ignored in the calculations, as in practice it is very small in PM in-wheel machines.

The flux density, due to the magnet MMF, decays with distance from the magnets. Therefore, the coil sides are divided into four layers around the four points shown in 4.1. In each of these four layers the average flux density variation is calculated and used in (4.9). The layers are divided so that the number of conductors increases in the layer as the distance from the magnets increases, e.g. the top layer would have only one row of conductors while the second

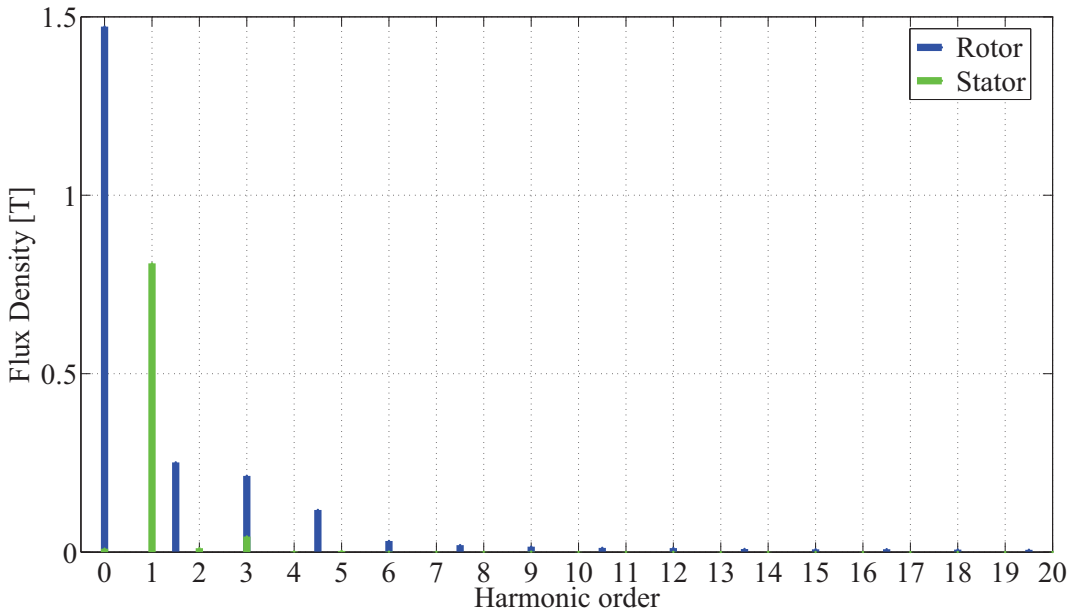

Figure 4.4: Tangential flux density harmonics at different points in the rotor and stator yokes of an optimized 40-pole, 30-slot machine with open stator slots.

layer would have three rows of conductors included. The number of conductors in each layer is then multiplied with (4.9) to find the loss value for that layer.

Both the radial and tangential flux density variations in the slot are considered. In Fig. 4.5 the average radial variation of the different layers are shown for an optimized 40-pole, 30-slot machine with open stator slots. From Fig. 4.5 the decay of the flux density variation from the top layer to the bottom layers is clear. The fundamental frequency of the flux density variation, arising from the movement of the magnets, is equal to an electric machine cycle. The harmonic contents of the flux density variations in the different layers is shown in Fig. 4.6. From these results it can be concluded that the majority of eddy current losses in the stator coils will be near to the air gap (1^{st} layer), closest to the magnets.

4.3 Eddy current losses in the permanent magnets

The induced eddy current losses in magnets are of great concern in concentrated-coil PM machines due to the relatively large flux pulsations in the magnets caused by the stator slotting and the stator MMF harmonics. Because of the linear demagnetization curve of the magnet material, there is no hysteresis loss component, but only an induced eddy current loss component due to the conductivity of the material. The eddy current loss in the magnets is estimated by using an equation given by [27] that calculates the instantaneous magnet loss density in magnets. From the equation given by [27] the average loss density in the magnet, p_m in W/m^3, is

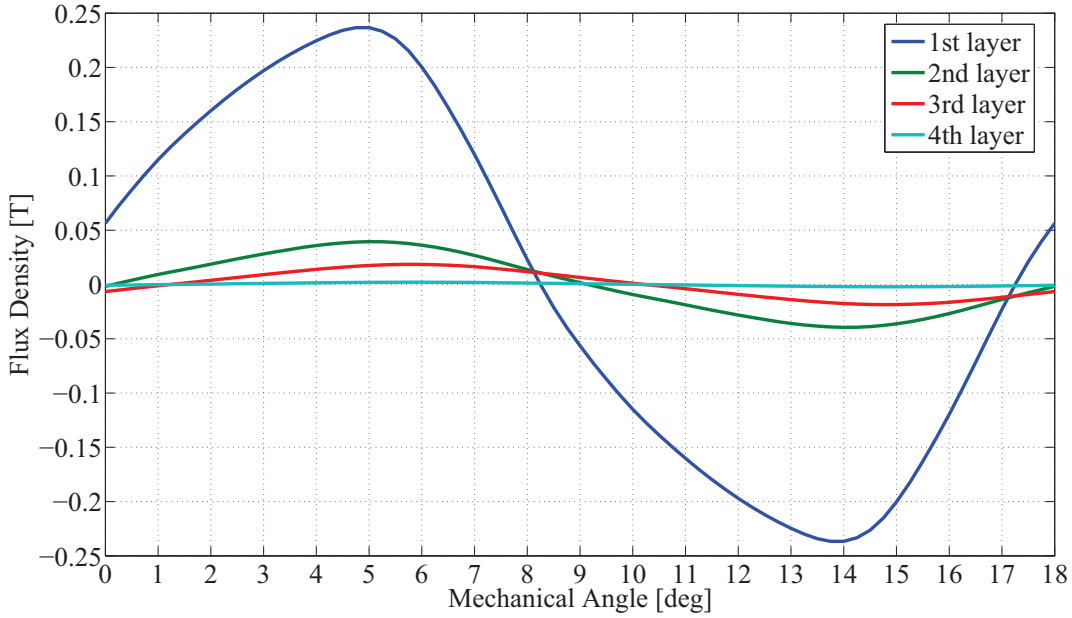

Figure 4.5: Average radial flux density variation in the four layers of the stator coil of an optimized 40-pole, 30-slot machine with open stator slots.

derived as

$$p_m \approx \frac{\pi^2 b_m^2 B^2 f^2}{3\rho}, \tag{4.10}$$

where b_m is the magnet width and ρ is the resistivity of the magnet material.

The radial flux density variation at a point in the magnet under no-load conditions (just due to the slot) is shown in Fig. 4.7 of an optimized 40-pole, 30-slot slot machine with open stator slots. The flux density variation in the tangential direction is so small that it is considered to be zero and effectively ignored in the loss calculations of the magnets. It is important to note that the frequency content of the flux density variation in the permanent magnets, as shown in Fig. 4.7, is similar to that in the rotor yoke, but different to the flux density pulsations in the stator. The harmonic content of the pulsations in Fig. 4.7 is shown in Fig. 4.8.

4.4 Frequency harmonic loss calculation

The principle of superposition is used to include the various harmonic components in the loss calculation of the iron losses, eddy current losses in the stator coil and permanent magnet losses. Hence, if the number of regions is n and the harmonic order considered is v, then the iron loss, P_c, is calculated from (4.4) as

$$P_c = \sum_{j=1}^{n} \left(m_{rj} \sum_{i=1}^{v} k_h f_{ij} B_{ij}^{\alpha} + k_e f_{ij}^2 B_{ij}^2 + k_{exc} f_{ij}^{1.5} B_{ij}^{1.5} \right), \tag{4.11}$$

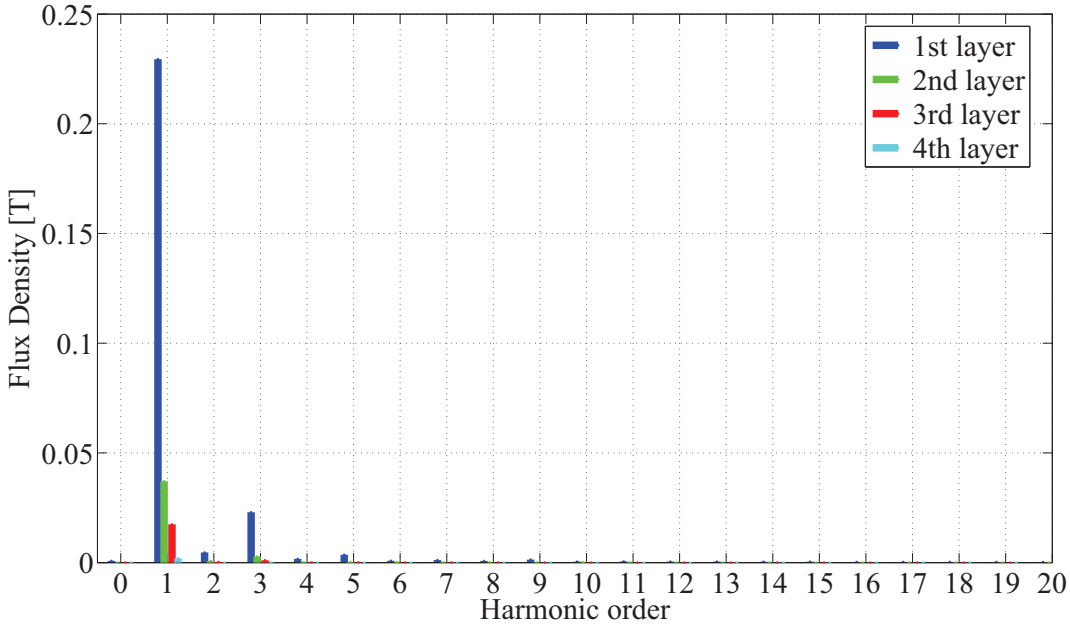

Figure 4.6: Average radial flux density harmonics in the four layers of the stator coil of an optimized 40-pole, 30-slot machine with open stator slots.

where m_{rj} is the mass of the region j, and f_{ij} and B_{ij} are the frequency and the flux density amplitude of harmonic order i of region j respectively. Similarly the eddy current losses in the stator conductors are calculated from (4.9) as

$$P_s = \sum_{j=1}^{n} \left(n_{cj} \sum_{i=1}^{v} \frac{\pi^3 l d^4 B_{ij}^2 f_{ij}^2}{8\rho} \right), \tag{4.12}$$

where n_{cj} is the number of stator conductors in region j. The eddy current losses in the permanent magnets are estimated from (4.10) as

$$P_m = \sum_{j=1}^{n} \left(Vol_j \sum_{i=1}^{v} \frac{\pi^2 b_{mj}^2 B_{ij}^2 f_{ij}^2}{6\rho} \right), \tag{4.13}$$

where Vol_j is the volume of region j in the magnet.

4.5 Conclusion

The error made when using the proposed method to calculate the various losses of a machine under certain operating conditions is not of high importance in this study. The results of the loss calculations are used in Chapter 5 to compare different optimum designed machines and their associated losses. By using the results in a comparative study, the error, if any, made in the calculations can be ignored since it will be the same for all the machine examples used.

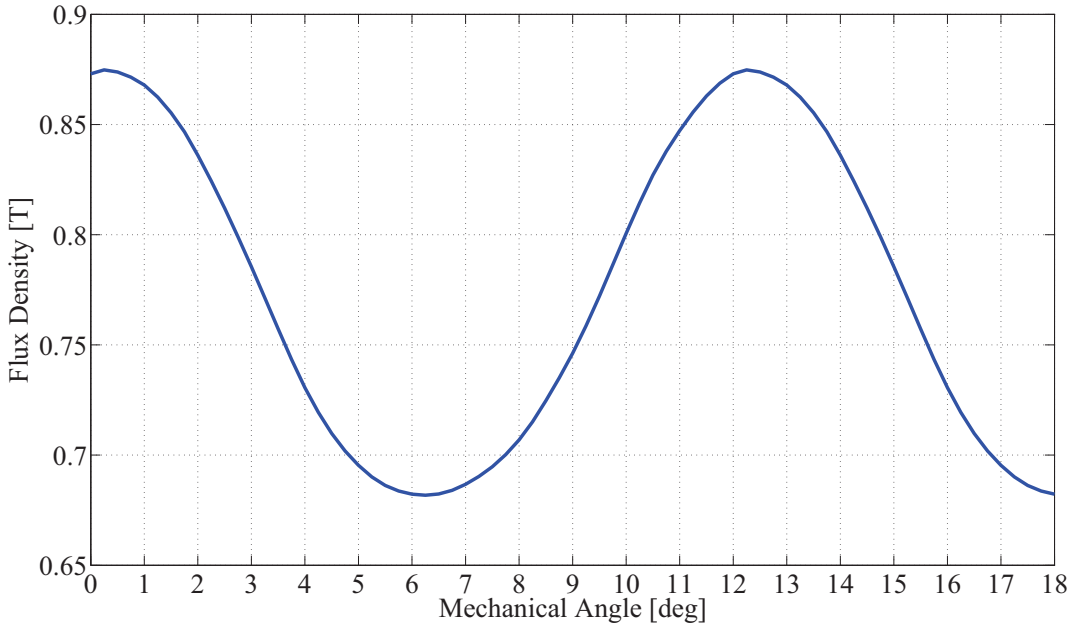

Figure 4.7: Radial flux density variation in the magnet of an optimized 40-pole, 30-slot machine with open stator slots under no-load conditions.

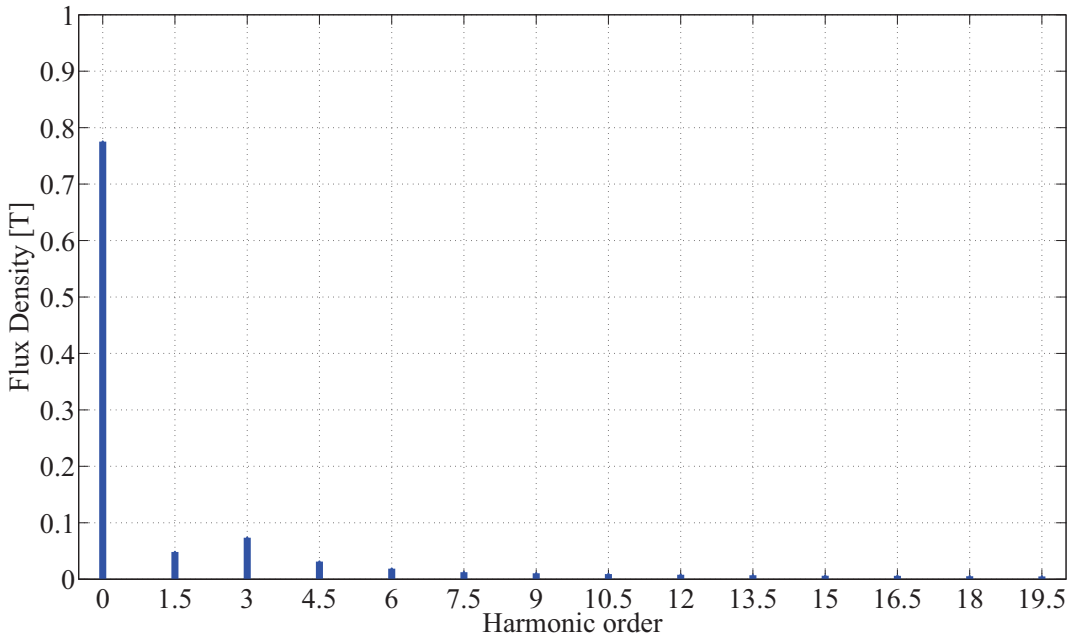

Figure 4.8: Radial flux density harmonics in the magnet of an optimized 40-pole, 30-slot machine with open stator slots under no-load conditions.

CHAPTER 5

OPTIMUM DESIGN

The per wheel power and torque performance of a typical 1600cc internal combustion engine (ICE) powered vehicle is shown in Fig. 5.1. The power and torque at each wheel is calculated from the models given by [74], included in Appendix B, and assuming a four wheel drive vehicle. Also shown in Fig. 5.1 is the power and torque per wheel available if a PM hub motor is used. In this case the hub motor performance is that of a non-overlap concentrated-coil PM machine. The technology of these concentrated-coil PM machines, amongst others, reduces manufacturing cost [75], increases efficiency by reducing the end winding length [76] and exhibits high torque quality [77]. The topology of an outside rotor with interior PMs and concentrated-coil non-overlapping double layer winding stator with semi-closed slots, discussed in this chapter, is shown in Fig. 5.2.

There are various possible pole-slot combinations for these concentrated-coil PM machines [14, 78, 79]. The winding factors for the different pole-slot combinations were calculated by [14, 69], with a simplified method given in Chapter 2.2. The machine with the highest winding factor is normally considered to be the best machine but the final pole-slot choice is also influenced by possible vibrations and noise of the PM machine due to unbalanced magnetic

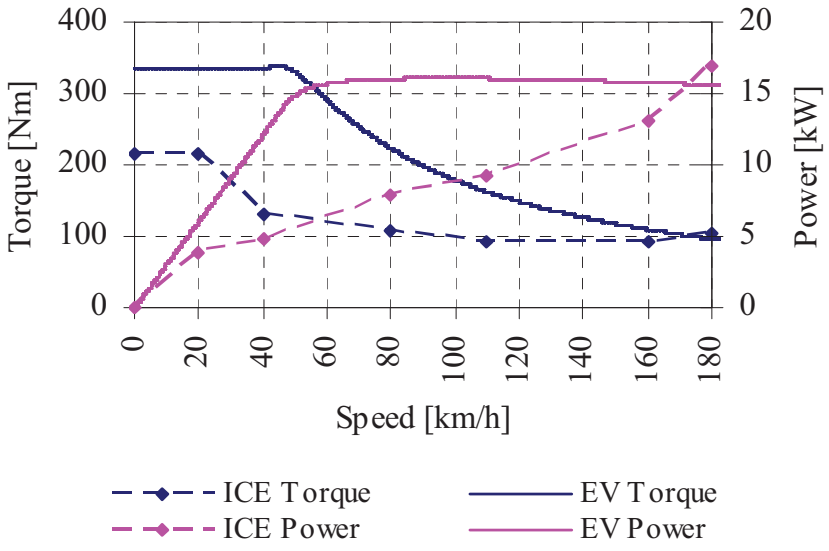

Figure 5.1: Power and torque per wheel versus speed of an ICE powered vehicle and EV hub drive vehicle.

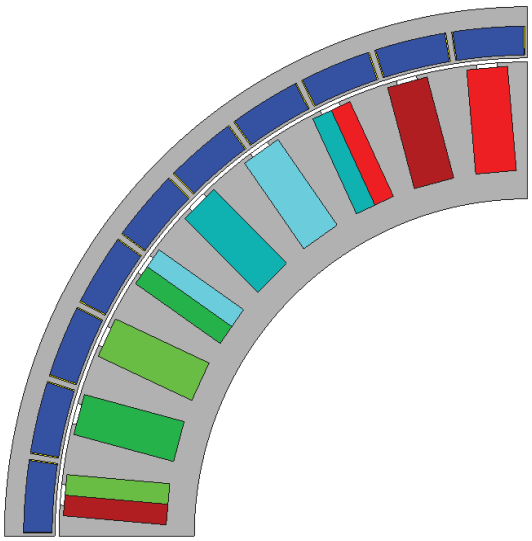

Figure 5.2: Section of a 40-pole/36-slot machine with interior PMs and concentrated-coil windings for use as a hub motor in an EV.

forces and torque ripple [80–82]. The machine losses are also affected by the pole-slot choice, as explained by [68].

Machines with low winding factors are normally not considered for various applications due to their expected lower performance. A complete performance evaluation of optimum designed PM machines with low winding factors compared to machines with good winding factors is still lacking in literature. In this chapter a performance evaluation of different PM machine design configurations that include those designs with low manufacturing costs and low winding factors is done. The application is for EV hub motors as explained above. There are various stator and rotor design aspects that affect the performance of the PM machine with non-overlap concentrated-coil windings. These design aspects are considered in the following sections.

5.1 Stator slot shape

The stator slot shapes investigated for the application are divided into two categories, namely open slot shapes and semi-closed slot shapes as shown in Fig. 5.3a and 5.3b respectively (the coil assembly method is shown in Fig. 5.4). A comparison of these two types of slots in the performance of brushless DC machines is also done by [83], although for a different application. The slot shapes certainly, and may significantly affect the performance of the machine. This performance, however, must be weighed against manufacturing cost. For example, stator cores with semi-closed slots have to be wound, which is more expensive than open slot straight teeth

stators where preformed coils can be used. In this study only PM machines with concentrated-coil, double layer windings are considered.

5.1.1 Case study: slot opening

A case study is done on a 20-pole, 30-slot machine with single layer windings and surface mounted PMs to see what the effect is of closing or opening the stator slot at the air gap side [84]. According to literature, this is not such a good machine, but the combination is specifically chosen to see what the effect of the slot opening is on the torque ripple and the flux pulsations in the rotor.

The two aspects that are looked at in this study are the torque ripple and flux density pulsations versus stator slot opening. The modelling described in Chapters 3 and 4 of the PM machine is used to calculate the torque ripple and the flux density pulsations in the rotor. These calculations are done for a range of stator slot openings. The opening is varied from an almost

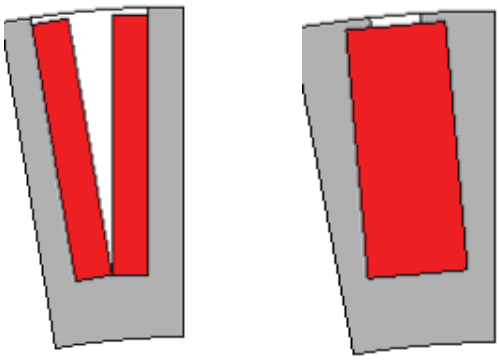

(a) Open slot (b) Semi-closed slot

Figure 5.3: Stator slot design options.

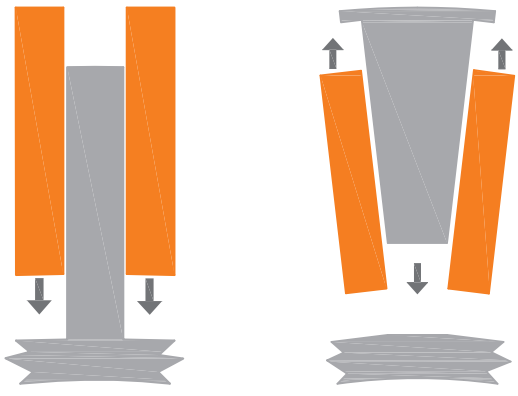

(a) Open slot (b) Semi-closed slot

Figure 5.4: Stator lamination and coil assembly.

closed 1.5 mechanical degrees to an open slot topology, with 6.5 mechanical degrees being the slot width. Figure 5.5 shows the machine topology using the two extreme values in the range. Some of the machine's dimensions and performance figures are given in Table 5.1. It should be noted that the average torque remains almost constant through the range of slot openings and that the mass of the machine changes slightly.

Figure 5.6 shows the variation in amplitude of the flux density in the magnets when the rotor is position-stepped and the stator slot opening is varied. (The flux densities are not estimated from the air gap flux density, but calculated in the iron yoke and magnets of the rotor.) The flux density pulsations complete 15 cycles in every revolution of the 20-pole machine. This means that the fundamental flux density pulsation frequency in the rotor is 1.5 times the fundamental current frequency in the stator. These pulsations are not present in a normal distributed

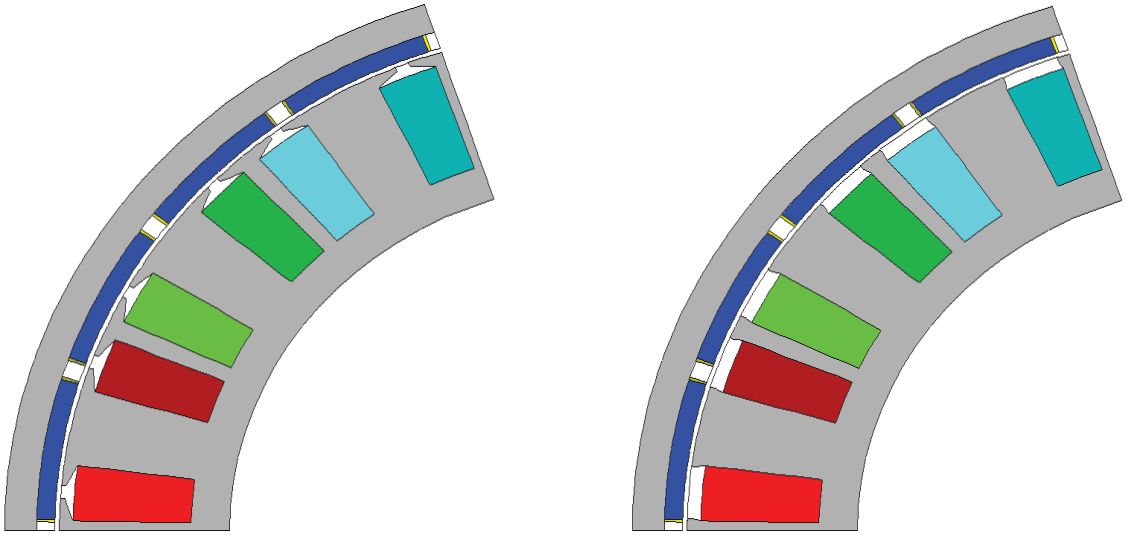

(a) 1.5 degree slot opening (b) 6.0 degree slot opening

Figure 5.5: Stator slot openings of machines with 20 poles and 30 slots.

Table 5.1: Parameters of the 20-pole 30-slot machine

Torque [Nm]	244
Power [kW]	10.6
Speed [r/min]	420
Rotor outer diameter [mm]	270
Stator inner diameter [mm]	170
Axial length [mm]	80
Active Mass [kg]	19.0
Winding factor	0.866

winding PM machine and are due to the pole-slot combinations of the PMSM as explained in Chapter 2. The amplitude of the flux density pulsations increases when the slot opening is varied from semi closed to open (the increase is the same for the flux density pulsations in the rotor's iron core and magnets). This increase is significant if you consider that just the eddy current losses in the rotor core are proportional to the square of the amplitude of the pulsations as given by (4.4).

Torque ripple is of special interest in direct drives and the effect of the slot opening on the torque ripple is shown in Fig. 5.7. A decrease of up to 23% in torque ripple can be achieved when an open slot is used instead of a semi closed stator slot for this machine topology. An important advantage when changing the stator slot opening to affect the torque ripple, is that the average torque stays almost constant from minimum to maximum values of the slot opening.

5.2 Rotor configuration

A few rotor design options that affect specifically the torque and constant power speed range (CPSR) performance of the machine have to be considered. The CPSR is defined, amongst others, by [85] and discussed in section 5.6.2. These design options are (i) outer rotor versus inner rotor and (ii) surface mounted magnets versus embedded or interior magnets. The mechanical integrity that the outer rotor design gives to the structure regarding the centrifugal

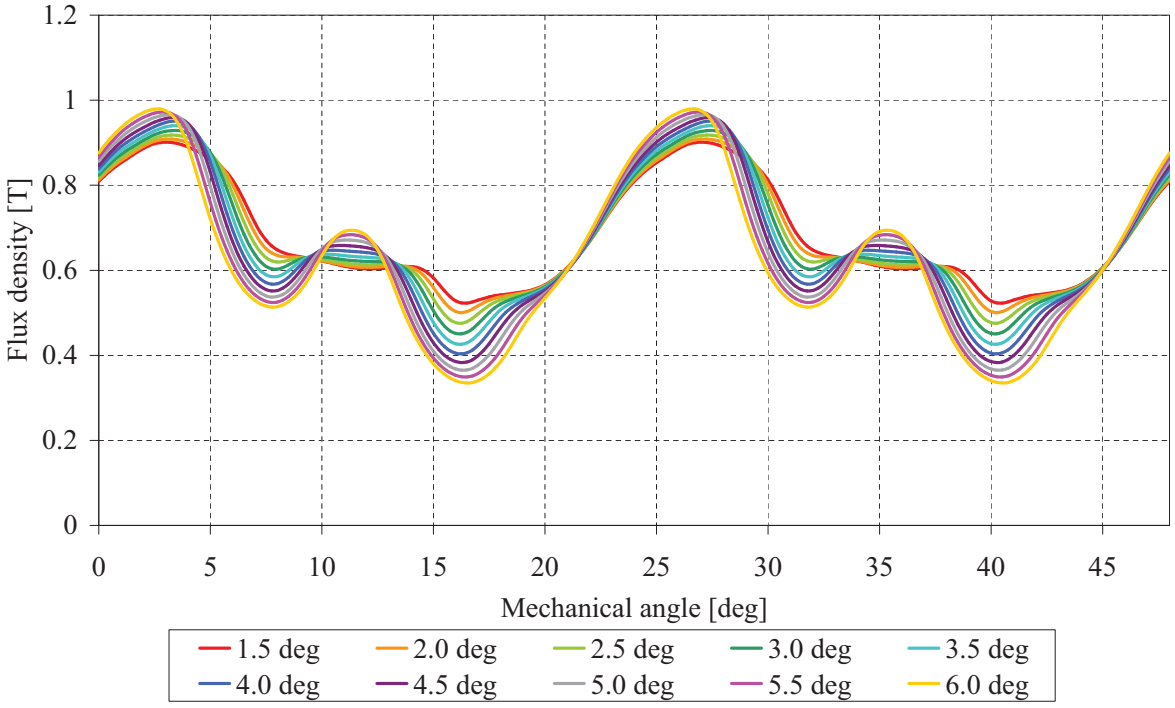

Figure 5.6: Flux density pulsations in the magnets with stator slot opening a parameter.

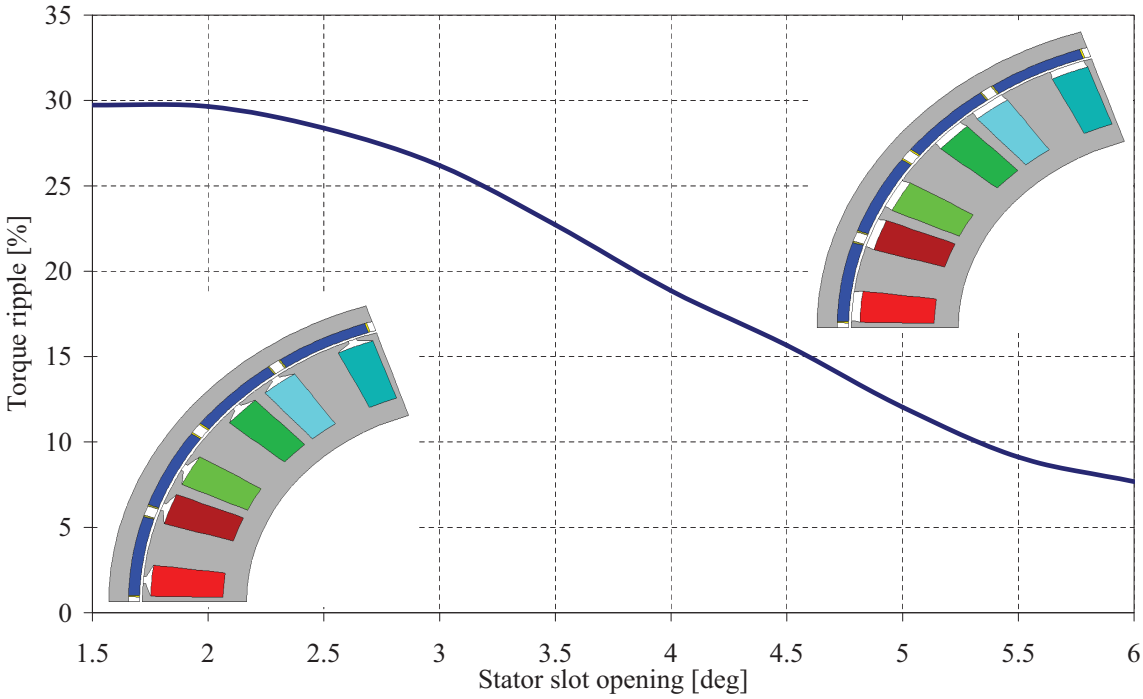

Figure 5.7: Torque ripple of the machine with stator slot opening as variable.

forces on the magnets is an advantage. With the outer rotor the air gap surface area is increased while adhering to specific volume requirements. The outer rotor also allows easier manufacturing of the stator as the slots are exposed. In this study only the outer rotor option is considered.

Three cases are investigated with regard to the mounting of the magnets namely surface mounted magnets, embedded magnets and interior magnets as shown in Fig. 5.8. Embedded magnets have the space between the magnets filled with laminated iron, while interior magnets are totally enclosed with laminated iron.

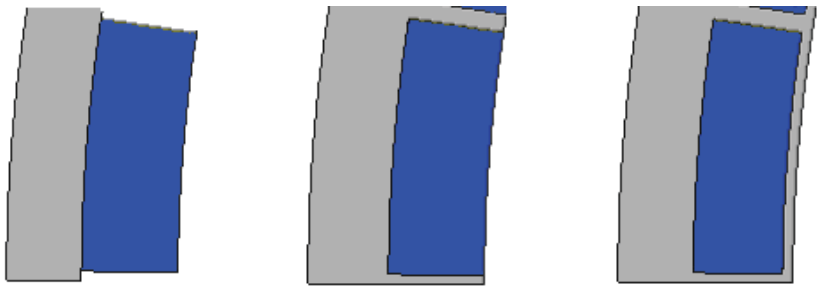

(a) Surface PM (b) Embedded PM (c) Interior PM

Figure 5.8: Rotor design options.

5.3 Pole-slot combination

A substantial amount of work has been published on the winding factors of various pole-slot combinations of concentrated-coil PM machines [14, 15, 68, 69, 78, 86]. In general the winding factor is used as the main criterion in choosing a pole-slot combination for best machine performance. In conjunction with this there are two other factors that also affect the pole-slot combination choice. These factors are the lowest common multiple (LCM) and the greatest common divisor (GCD) of the pole and slot numbers. The LCM value affects the torque ripple of the machine, while the GCD value gives the number of magnetic symmetrical portions in the machine. Considering the work done by [80–82], a pole-slot combination that gives the highest LCM value and lowest GCD value but greater than unity, should be chosen. The pole number in these choices is normally dictated by the machine speed and frequency.

For example: 40-pole/30-slot : LCM = 120
GCD = 10
30-pole/27-slot : LCM = 270
GCD = 3

5.4 Objective function

As the different stator and rotor design options and configurations result in very different performances in the high speed region of the machine, the design optimization is done at base speed rather than at maximum speed of the PM hub drive. The best possible machine performance from Fig. 5.1, is required at 50 km/h vehicle speed and not e.g. at 130 km/h. The high speed performance, specifically the CPSR, of the EV hub drive is then studied as a result of the design optimization done at base speed.

The design optimization at base speed is done by maximizing the torque per I^2R copper loss of the machine, subject to certain design constraints. In this way the torque/copper-loss performance of the PM machines can be compared, which is important in the low speed region of the machines. The other machine performances like torque ripple, torque/active-mass and efficiency are studied and compared as a result of the torque/copper-loss design optimization.

For the particular in-wheel EV case studied, the I^2R copper loss of the PM machines is set at a rated value of 1 kW in the FE program and used in the design optimization; this amount of copper loss obviously depends on the cooling and rated performance of the machine. The

objective function to be maximized (or minimized) can be written in the simple form of

$$Y = F(\mathbf{X}), \tag{5.1}$$

where Y is the output value of the unconstrained objective function and $\mathbf{X}$ is a multidimensional vector representing the machine dimensions, but may also include other parameters that will affect the value of Y.

For the evaluation in this chapter, the average torque, T_{ave}, per I^2R copper loss of the machine is maximized. The current density J, as parameter, is used in a constrained optimization as described by [87]. A weighted penalty function, that assigns a positive penalty ε for increased constraint violation, is added to the objective function. The objective function is then defined as

$$Y = F(\mathbf{X}, w) = T_{ave}(\mathbf{X}) - w\varepsilon, \tag{5.2}$$

where

$$\varepsilon = \left\{ \begin{array}{cc} (J(\mathbf{X}) - J_{max})^2 & : J(\mathbf{X}) > J_{max} \\ 0 & : J(\mathbf{X}) \leq J_{max} \end{array} \right\} \tag{5.3}$$

and w is an associated weighting factor. As is clear from (5.3), a quadratic penalty function is used which ensures a positive value for ε when the current density exceeds the set maximum value J_{max}; and $\varepsilon = 0$ when the current density is within the specified limit. For this reason F in (5.2) can be expressed as a simple algebraic sum.

5.4.1 Optimization parameters

The machine parameters that are kept constant in the optimization procedure are the copper losses (P_{cu}), current angle (ϕ), outer diameter, inner diameter and stack length of the machine. By keeping the outer machine dimensions constant the active volume of the machine is kept constant. This is a prerequisite for the mechanical design and the support structure that needs to fit inside a normal wheel rim. The five machine dimensions that are varied and optimized in the design, to maximize (5.2), are the air gap diameter (d_g), the coil width (b_c), coil height (h_c), the magnet pitch (b_m), and magnet height (h_m), as shown in Fig. 5.9. The yoke height is optimized as a consequence of the optimization of the other dimensions.

5.5 Design optimization

Various optimization algorithms are compared by [88] and from these the Powell's optimization algorithm, described in 1964 [89], is chosen and used to optimize the overall machine

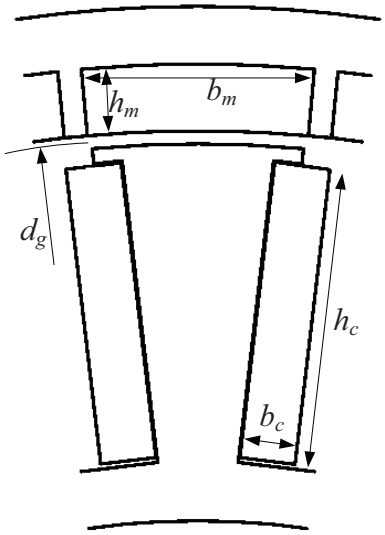

Figure 5.9: A machine section showing the machine dimensions optimized in the design optimization.

design. The algorithm is adapted to maximize, instead of minimize, the objective function. The optimization algorithm then finds the multidimensional vector **X** that results in a maximum value of the objective function Y. The I^2R copper losses are taken into account by keeping it constant in the optimization, while the other losses are studied as a result of the optimization.

The procedure for optimizing the design of the PM machines can be best explained by the use of the flow chart of Fig. 5.10. Using the FE solution, the optimization algorithm assigns values to the vector **X** that maximizes the objective function Y. For each iteration r, the optimization algorithm determines multiple directions of search along which Y is maximized. The FE program is incorporated into the optimization algorithm, so that each time a new value is assigned to the vector **X**, the FE program is executed to determine Y.

The FE program generates a new mesh, of the modeled machine section, each time it is executed. The new mesh is generated according to the changed input **X**. After re-meshing the FE program does the pre-processing followed by the non-linear solution to determine the magnetic vector potentials throughout the model. When the magnetic vector potentials are known, the FE program calculates the various flux linkages and the air gap torque. (The correct B-H curve is used in the non-linear solution, to take saturation in the laminated steel parts of the machine into account.) The FE program is called by the optimization algorithm, and at the end of each optimization iteration the value of Y is tested to see if an absolute maximum has been reached. If a maximum of Y has been reached the optimization procedure terminates and if not, another iteration is performed. Total execution time of an optimization depends on the number of machine variables (in the vector **X**).

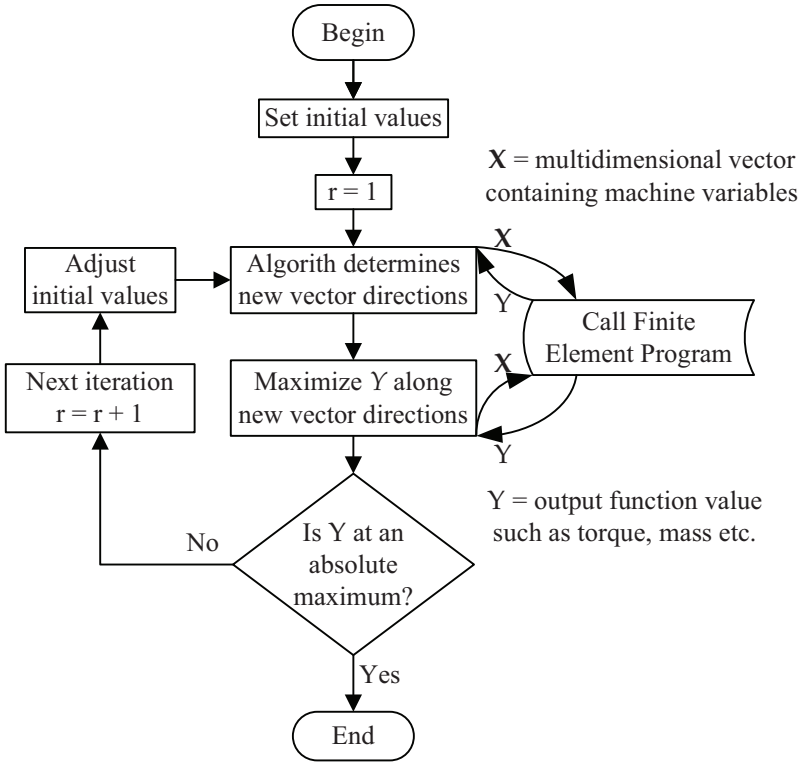

Figure 5.10: Optimization procedure using the FE method.

In Fig. 5.11 some results are given of the Powell optimisation method for the 30-pole 27-slot machine with semi-closed stator slots and embedded magnets, as discussed in Chapter 7. Here the trend of the objective function, magnet height, h_m, and coil height, h_m, is shown.

5.6 Design comparison

5.6.1 Optimized 40-pole machine designs

Different machine designs are optimized to see how the slot shape, rotor configuration and pole-slot combinations affects the machine performance. As mentioned before, the machines are optimized at base speed. The design optimization is done as described in sections 5.4 and 5.5. The total number of series turns per phase is adjusted so that the terminal voltages of the machines are equal. (The terminal voltage-limit is due to the fixed dc-bus voltage of the hub drive inverter.) The phase current is given by (3.11), according to the phase resistance because the I^2R copper losses are fixed at 1 kW.

The pole-slot combinations investigated are the 40-pole/30-slot machine with a winding factor of 0.866 and the 40-pole/36-slot machine with a winding factor of 0.945. The 30-slot stator is specifically chosen to investigate a machine with a low winding factor. The pole number of the machines is fixed to keep the machine speed and frequency the same so that losses can

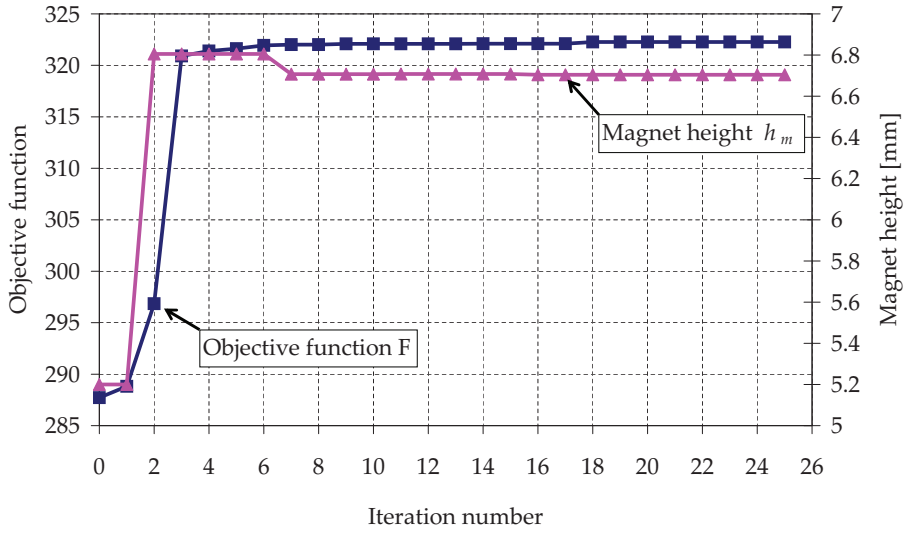

(a) Magnet height

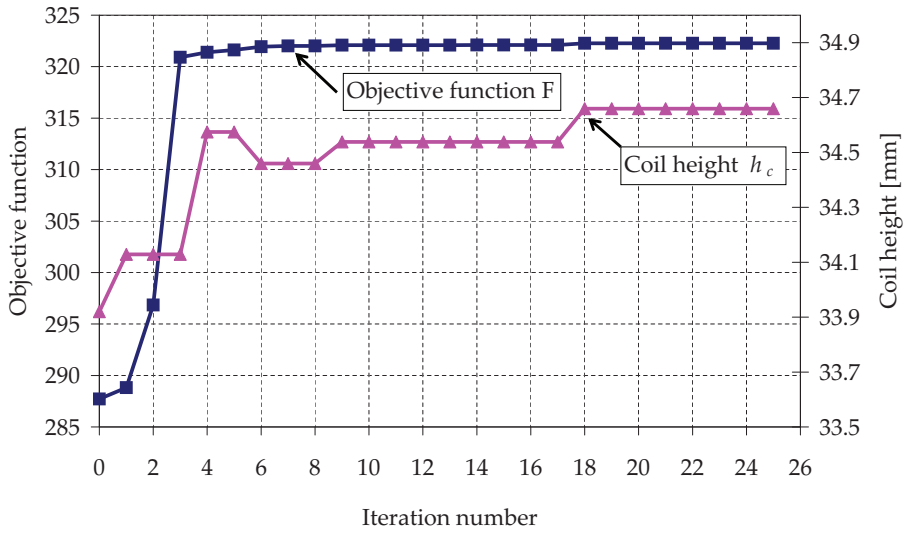

(b) Coil height

Figure 5.11: Trend of the machine dimensions and objective function in the design optimisation of a 30-pole 27-slot machine with semi-closed stator slots and embedded magnets, as discussed in Chapter 7.

be compared on an equal basis. The machines are modelled with both open and semi-closed stator slots as well as with the three desribed rotor configurations. In total twelve machines are modelled and optimized. Figure 5.12a shows a machine section ($\frac{1}{10}^{th}$) of the 40-pole/30-slot machine with open slots and interior PMs, while Fig. 5.12b shows a section ($\frac{1}{4}^{th}$) of the 40-pole/36-slot machine with surface mounted PMs and semi-closed slots. Some dimensions that are common in all the machines are given in Table 5.2

The various losses of the optimized machines are calculated (as described in Chapter 4) and are explained in Tables 5.3 and 5.4. The open slot design significantly influences the PM losses

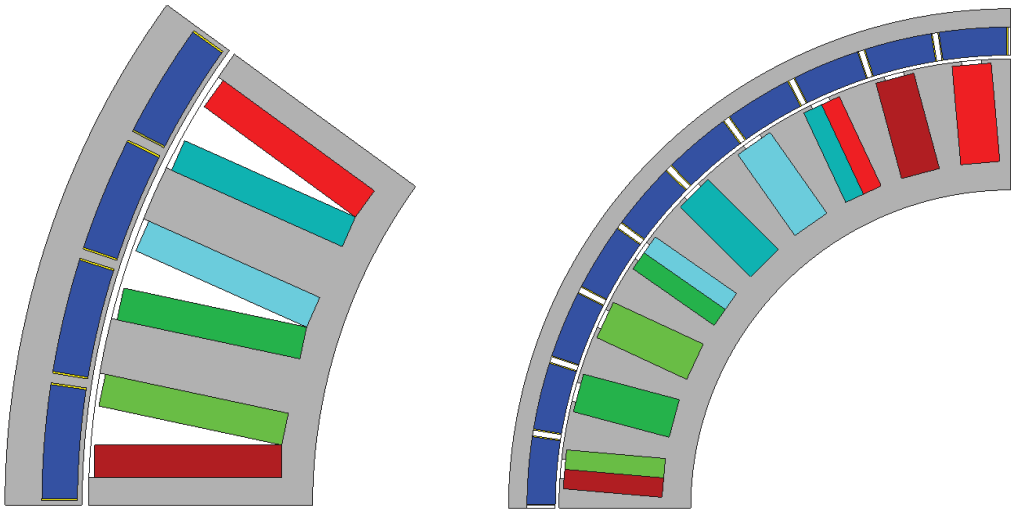

(a) 30-slot machine (b) 36-slot machine

Figure 5.12: FE machine models used in the design optimization.

Table 5.2: Parameters of the 40-pole machines

Base speed [r/min]	420
Rotor outer diameter [mm]	270
Stator inner diameter [mm]	172
Axial length [mm]	100

on the rotor and the eddy current losses the stator, with both these losses being higher than in the case of the machines with the semi-closed stator slots.

From the results in Tables 5.5 and 5.6 it is clear that the winding factor is not an accurate indication of the torque per copper loss performance of the machine. In fact the low winding factor PM machines are found to have slightly higher torque per copper loss performance than the good winding factor PM machines. The efficiency, however, of the low winding factor machines is typically 2% lower than that of the good winding factor machines. As the I^2R copper loss of all the machines is the same, low winding factor machines are shown to have higher iron and magnet losses, i.e. for a given pole number.

Other factors, such as the slot and rotor topology, have a significant effect on the machine performance. The open slot PM machines have 5-10 % less torque per copper loss than the semi-closed slot PM machines. However, the active mass of the open slot machines is less, so that the torque per active mass of the open slot and semi-closed slot PM machines is very much the same. If only these results are considered, the open slot machines have the advantage of a lower manufacturing cost due to the use of preformed stator coils.

Table 5.3: 40-Pole/30-Slot loss breakdown

Slot type	Semi-closed slots		
Magnets	Surface	Embedded	Interior
Rotor Iron Losses [W]	42	125	119
Stator Iron Losses [W]	36	40	34
Eddy current losses [W]	227	213	146
Magnet Losses [W]	609	501	376
I^2R [W]	1000	1000	1000
I_{rms} [A]	63.5	66.4	66.0
Total losses	1914	1879	1675
Slot type	Open slots		
Magnets	Surface	Embedded	Interior
Rotor Iron Losses [W]	89	179	169
Stator Iron Losses [W]	48	61	48
Eddy current losses [W]	359	366	252
Magnet Losses [W]	1101	864	614
I^2R [W]	1000	1000	1000
I_{rms} [A]	57.7	61.5	59.7
Total losses	2597	2470	2084

The LCM value of the 40-pole/36-slot machines is three times higher than that of the 40-pole/30-slot machines. Although the relationship between the LCM value and the torque ripple is not linear, it gives an indication of the torque quality of the machine [82]. The LCM-value is also an indication of the losses of a machine relative to other machines with the same pole number.

5.6.2 Constant power speed range (CPSR)

The constant power speed range is defined as the inverse ratio of the machine's base speed and highest speed of which the power output of the machine is equal to 1 p.u. The 1 p.u. power points at base speed and highest speed are indicated in Fig. 5.13 by the red dots on the power curve of the 40-pole/36-slot machine. Figure 5.13 shows two, out of the twelve machines', power versus speed profiles[13]. Note that for the 40-pole/30-slot machine in Fig. 5.13 the CPSR,

[13]The difference in CPSR between these machines can be attributed to the 30 % difference in d-axis inductance.

Table 5.4: 40-Pole/36-Slot loss breakdown

Slot type	Semi-closed slots		
Magnets	Surface	Embedded	Interior
Rotor Iron Losses [W]	12	59	47
Stator Iron Losses [W]	30	32	29
Eddy current losses [W]	43	37	21
Magnet Losses [W]	305	264	194
I^2R [W]	1000	1000	1000
I_{rms} [A]	61.1	63.3	60.7
Total losses	1389	1391	1290
Slot type	Open slots		
Magnets	Surface	Embedded	Interior
Rotor Iron Losses [W]	30	101	77
Stator Iron Losses [W]	30	36	29
Eddy current losses [W]	156	143	76
Magnet Losses [W]	946	690	424
I^2R [W]	1000	1000	1000
I_{rms} [A]	55.0	57.2	53.3
Total losses	2162	1970	1605

as indicated by Table 5.5, is equal to 5.2. From Tables 5.5 and 5.6 it can be seen that surface mounted PM machines have lower CPSR's compared to the embedded and interior mounted PM rotor machines.

5.7 Conclusion

The performance of different optimum designed double-layer PM concentrated-coil machines for in-wheel EV applications is considered in this Chapter. From the design comparison the following conclusions are drawn:

- The torque per I^2R copper loss performance of concentrated-coil PM machines cannot be judged solely on the winding factor of these machines, as suggested by [90].
- The PM machines with low winding factors and low LCM-values are shown to have higher iron and magnet losses, and thus lower efficiencies, than machines with good

Table 5.5: 40-Pole/30-Slot optimization results per 1 kW I^2R losses

Slot type	Semi-closed slots		
Magnets	Surface	Embedded	Interior
k_w / LCM / GCD	0.866 / 120 / 10		
T_{ave} [Nm]	339.7	336.2	294.7
T_{ave}/Mass [Nm/kg]	18.95	18.5	16.21
T_{rip} [%]	28.7	18.2	9.6
CPSR	1.9	5.2	5.37
L_d [mH]	1.082	1.263	1.362
L_q [mH]	0.965	1.115	1.219
Efficiency [%]	91.8	91.8	91.7
Slot type	Open slots		
Magnets	Surface	Embedded	Interior
k_w / LCM / GCD	0.866 / 120 / 10		
T_{ave} [Nm]	308.7	310.1	281.3
T_{ave}/Mass [Nm/kg]	18.93	18.81	17.05
T_{rip} [%]	11.7	21.6	24.2
CPSR	1.6	2.05	4.7
L_d [mH]	1.017	1.013	1.187
L_q [mH]	0.999	1.08	1.225
Efficiency [%]	88.2	88.8	89.5

winding factors and higher LCM-values. There is also a clear tendency that machines with open slots have higher iron, magnet and stator eddy current losses than machines with semi-closed stator slots, due to the magnet and slot interaction. However, this loss difference is found to be less in machines with good winding factors than in machines with low winding factors.

- The rotor topology affects the average torque and CPSR of the machine. Machines with interior PM rotors have less developed torque per copper loss than machines with surface mounted PM rotors. However, the CPSR of machines with interior PM rotors is better than the CPSR of machines with surface PM rotors and this result agrees with the work done by [91].

- Although the developed torque per copper loss of machines with open slots is less than

Table 5.6: 40-Pole/36-Solt optimization results per 1 kW I^2R losses

Slot type	Semi-closed slots		
Magnets	Surface	Embedded	Interior
k_w / LCM / GCD	0.945 / 360 / 4		
T_{ave} [Nm]	337.3	326.6	290.2
T_{ave}/Mass [Nm/kg]	18.94	18.06	16.06
T_{rip} [%]	4.0	4.5	2.1
CPSR	1.3	1.85	5.9
L_d [mH]	1.029	1.089	1.358
L_q [mH]	0.955	1.054	1.229
Efficiency [%]	93.9	93.7	93.4
Slot type	Open slots		
Magnets	Surface	Embedded	Interior
k_w / LCM / GCD	0.945 / 360 / 4		
T_{ave} [Nm]	304.1	303.5	275.3
T_{ave}/Mass [Nm/kg]	18.39	17.97	16.43
T_{rip} [%]	1.0	2.1	2.1
CPSR	1.3	1.45	2.05
L_d [mH]	1.025	0.97	1.268
L_q [mH]	0.988	1.027	1.267
Efficiency [%]	89.8	90.6	91.5

that of machines with semi-closed stator slots, the torque per active mass is found to be the same as that of these machines.

- An important general finding is that the performance of open stator slot machines with rectangular preformed coils, and thus low manufacturing costs, is surprisingly better than what was expected. This was particularly the case for machines with good winding factors.

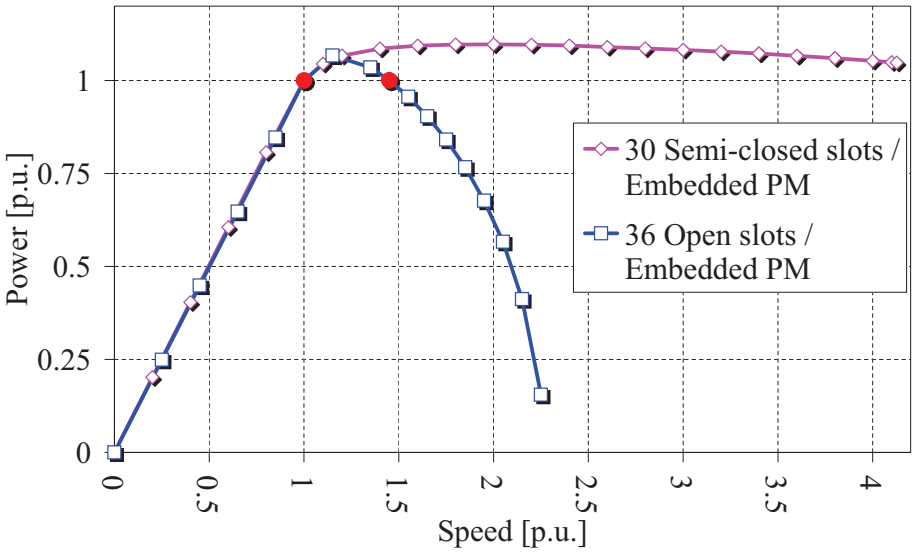

Figure 5.13: Rated power versus speed curves of a 40-pole/30-slot and 40-pole/36-slot PM machine.

CHAPTER 6

OPTIMUM CONTROL

The focus on high efficiency and cost effective drives for EVs, has led to the adoption of certain types of synchronous machines, with control algorithms that maximize efficiency [92]. To achieve the efficient wide speed operation (shown in Fig. 5.1) from the PM hub motors, that are used for this EV application, the control needs to be optimized. This requires a torque control algorithm that ensures high efficiency performance of the hub drive over the entire speed range. Implementing such a control algorith is required to test the designed hub motors through the operational speed range.

Two main schools of thought have emerged in regard to machine control, namely direct torque control (DTC) [93–100] and field orientated control (FOC) [64–67, 101–106], although it is not always possible to make such a clear distinction, and sometimes a combination of methods or a different approach is used.

Some torque control strategies within the field oriented control (FOC) category, similar to what is presented in this chapter, have been suggested [64–67]. In [64], the torque control problem is explained very well. The q-axis current reference is given by a PI speed controller, and the d-axis current reference is calculated: a decision between maximum torque per ampere (MTPA) or field weakening (FW) control is made based on the measured speed, and in both cases, the d-axis current reference is calculated using analytical machine equations with constant parameters. High dynamic decoupling current controllers are used to give the voltage reference. A voltage reference compensation function to limit the voltage reference in a way that gives preference to controlling the d-axis current, is also suggested. It has been demonstrated that this kind of control is capable of a fast dynamic response. The switch-over from MTPA to FW does not seem to be a problem, using the given decision-making trees. In [66] and [67] similar ideas are presented.

The focus of this chapter is on the torque control strategy for the EV hub motor. The proposed algorithm falls into the FOC category. Maximum torque per ampere and efficient field weakening is implemented using a set of 2D lookup tables (LUT) that directly translate the torque reference to the correct current space phasor reference in the synchronously rotating dq reference frame, for any given speed and DC bus voltage. This is similar to the work in [65], although in this chapter the method for obtaining the 2D LUTs is explained in full detail.

The torque control algorithm has been applied on the designed hub motors discussed in Chapters 5 and 7 [92]. The proposed torque control concept is explained in the sections that follow and implementation details are given.

6.1 Dynamic machine model

The stator voltage equation in the rotor reference frame is given by (3.5) and the torque equation is given by (3.32). These equations are general enough to take saturation, cross coupling and torque ripple (flux linkage variation with varying rotor position) into account. However, core loss (iron loss) and the end-winding flux linkage are neglected and assumed negligible for the purpose of this work.

The rated values and related information of the hub motor that are used as examples are given in Table 6.1. The hub motor has 40 poles with a non-overlap concentrated stator winding and an interior permanent magnet rotor.

The FE model cross section is shown in Fig. 6.1. The results from FE analysis shown in Fig. 6.2 describe the hub motor in polar coordinates. The input current vector to the FE program is $\mathbf{I}_s$ and the electro-static solution gives $\boldsymbol{\lambda}_{dq0}$. T_{ave} is solved using (3.32), and $\mathbf{V}_{dq0}$ is solved in the steady state using (3.8) with ω as an independent variable.

Figure 6.2a shows the current $\mathbf{I}_s$ of the hub motor with the outer circle corresponding to the rated current magnitude. Figure 6.2b shows the corresponding flux linkage $\boldsymbol{\lambda}_{dq0}$ for the hub motor, where it can be noted that saturation occurs in the positive d-axis. Figure 6.2c shows the torque magnitude $|T_{ave}|$ with current angle ϕ for the hub motor, i.e. the effect that current angle has on torque production for various current magnitudes. It allows one to identify maximum torque per ampere (MTPA) points easily. Small circles indicate MTPA points with the corresponding MTPA points shown in Figs. 6.2a, 6.2b and 6.2d.

Figure 6.2d shows the voltage evaluated for the rated speed of the hub motor using (3.8), in the steady state. Considering the voltage limitation imposed by the drive system (due to the DC bus voltage), as indicated by the dotted circle in Fig. 6.2d, achievable operating conditions are limited to the region within the circle (the solid lines) and unachievable operating conditions outside the circle (the dotted lines). This voltage restriction is reflected on the current, flux linkage and torque graphs as shown in Figs. 6.2a, 6.2b and 6.2c respectively.

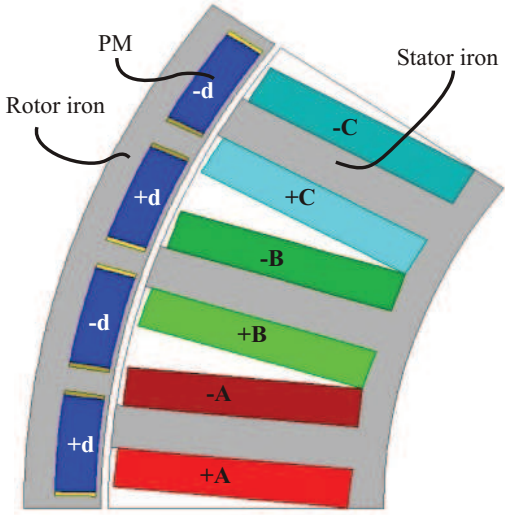

Figure 6.1: FE model of hub motor with concentrated windings.

Table 6.1: Hub motor rated values and related information.

Speed	465 r/min	Frequency	155 Hz
Voltage	73 V rms l-l	DC bus	120 V
Current	93 A rms	Flux linkage	0.085 V.s
Power	10 kW	Torque	200 N.m
Pole pairs	20	Stator slots	30

6.2 Suggested torque control algorithm

From FE analysis we know that the machine parameters are not constant, and in applications such as EVs where the DC bus voltage has a wide operating range, a decision for the current vector reference based only on the measured speed will not work. Any scheme that is based on parameter approximations of the non-linear functions, and those that use complicated decision trees and iteration, does not seem to be the simplest and most elegant solution. For industry acceptance, a scheme that is easy to implement, is always an advantage.

The hub motor has the greatest torque producing component due to the PMs, however, it also has a significant reluctance torque component, similar to a RSM, that must be utilized in a maximum torque per ampere (MTPA) control strategy. One method to implement MTPA is to use closed loop current vector control and to translate the torque reference (command) to the correct current vector reference that will result in MTPA. The translation can be done by finding the MTPA points on the dq current plane using FE analysis (please refer to Fig. 6.2c),

and to store these results in a set of one dimensional (1D) lookup tables (LUT), i.e. one 1D LUT for the the d-axis current reference as a function of reference torque $i_d^*(T_{ave}^*)$ and one 1D LUT for the q-axis current reference as a function of reference torque $i_q^*(T_{ave}^*)$.

Torque can be controlled successfully and energy efficiently below base speed using this method, however, once the machine advances beyond the base speed, the flux linkage magnitude caused by the MTPA current space phasor reference cannot be sustained due to the inverter's voltage limitation. This is illustrated by Figs. 6.2b and 6.2d. The current space phasor reference then has to deviate from the MTPA locus in order to get the flux linkage magnitude within the limit. The question is how to choose the current vector reference that will produce torque as close to the reference torque as possible, but at the same time will result in flux linkage that is within the flux linkage magnitude limit, and that stays within the current limits and to minimize the current magnitude (minimize power, assuming copper losses to be dominant).

The suggested torque control algorithm is illustrated by Fig. 6.3. Current vector control in the rotor reference frame using space vector PWM is used. In Fig. 6.3, the block C(s) is a PI controller with speed voltage decoupling and W(s) is a speed observer [107]. The flux linkage magnitude restriction is calculated using the measured speed (electrical rad/sec) and the measured DC bus voltage. The correct current space phasor reference for the requested torque, under the flux linkage magnitude restriction, is then obtained from a set of two-dimensional (2D) lookup tables, i.e. one 2D LUT is used for the d-axis current reference as a function of both torque reference and maximum allowable flux linkage magnitude $i_d^*(T_{ave}^*|\lambda_s|_{MAX})$ and one 2D LUT is used for the q-axis current reference as a function of both torque reference and maximum allowable flux linkage magnitude $i_q^*(T_{ave}^*|\lambda_s|_{MAX})$. Two dimensional interpolation is used so that reduced size lookup tables can be used.

In this method, there is a direct translation from the torque reference and flux linkage magnitude restriction to the current vector reference. There are no complicated equations, approximation or any decision making tables, plus the method works at any speed and any DC bus voltage. Therefore, the calculation effort has been removed from the load of the DSP and is rather performed off-line in an automated process. FE results are used directly and there is no approximation of parameters, although the modelling and results in the example are only valid in case of steady state operation.

6.3 Lookup table creation

Results from FE analysis are used to create 2D lookup tables: the torque reference and maximum flux linkage are inputs, and the i_d and i_q references are outputs. 2D interpolation is applied to the 2D tables in the control program. To create the lookup tables, a series of constraints are expressed as contour lines on the current plane, and decision making logic is used to find the correct current references. The MTPA contour is used as the line that represents the optimal solution. The torque reference contour and maximum flux linkage contour, as well as the maximum current contour (and maximum negative i_d due to possible de-magnetization of the PMs) represent the constraints.

Three examples are given next, and presented in Fig. 6.4. At high speed, for a given DC bus voltage, there is a maximum flux linkage that may be obtained and can be approximated by $|\boldsymbol{\lambda}_s| < \frac{V_{max}}{\omega}$, where V_{max} is the maximum voltage that can be given by the inverter with the given PMW method. Here, the resistive loss component and dynamic situations are neglected, and therefore in practice, a voltage buffer needs to be used to reserve some voltage. A current vector reference that lies on the maximum flux linkage contour needs to be selected, and therefore the reference torque may not be obtained. However, a point on the maximum flux linkage contour that is as close to the torque reference contour and the MTPA line as possible, may be selected, thereby obtaining the maximum amount of torque with the lowest current. This situation is shown in Fig. 6.4a.

At medium speed, the maximum flux linkage constraint is not so tough, and it is possible to obtain the reference torque. In this case, the intersection of the torque reference contour and maximum flux linkage contour is selected. This situation is shown in Fig. 6.4b.

At low speed, the maximum flux linkage constraint is very light, and it is possible to obtain the reference torque using less flux linkage than the constraint, i.e. to use a point on the MTPA curve. This situation is shown in Fig. 6.4c.

This decision making process has been automated and the 2D table is constructed within minutes using MATLAB. Since 2D interpolation is used in the control program, the table size can also be fairly small. A lookup operation is also much faster than any iterative decision making logic during execution. The method is exact, because it uses the FE analysis, so there is not even an attempt to linearize the machine or to find approximation functions. Two tables are created in an automated process for use inside the control program, and this is illustrated by Figs. 6.2e and 6.2f. The program flow diagram for creating the LUTs is given in Fig. 6.5.

6.4 Simulation

The torque control algorithm was simulated using a machine model that includes sets of 2D tables from FE analysis for the mapping between current and flux linkages, i.e. the effect of saturation and mutual coupling is modeled. The effect of non-sinusoidal flux linkage distribution during rotation, i.e. flux pulsation, and torque ripple, as well as iron-losses are neglected. The results of this simulation are shown in Fig. 7.14.

6.5 Conclusion

A torque control algorithm for PM hub motors that works for the entire speed range and for variable DC bus voltage is proposed and demonstrated.

The suggested torque control algorithm is based on a set of 2D LUTs that are generated directly from FE results and the method of obtaining these tables is fully explained. The practical implementation of the method is easy and should therefore be attractive for industrial drive applications.

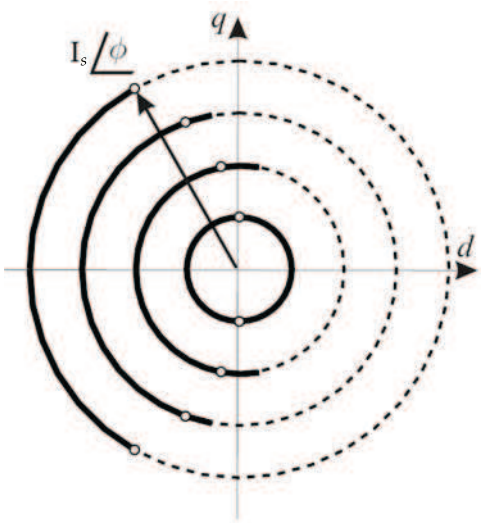

(a) Hub motor current.

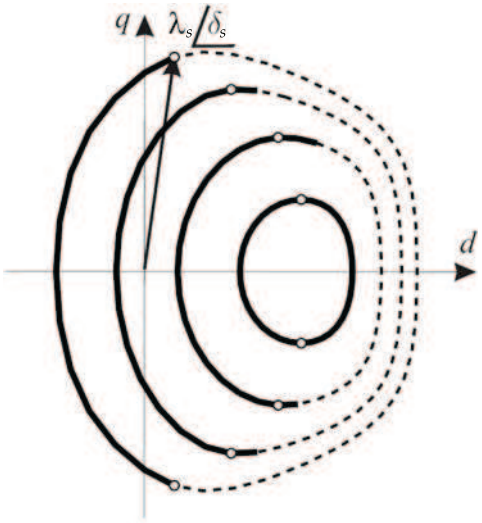

(b) Hub motor flux linkage.

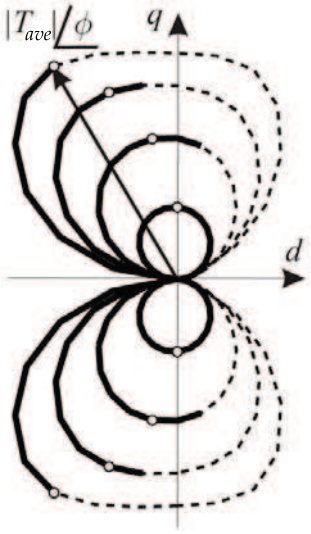

(c) Hub motor torque.

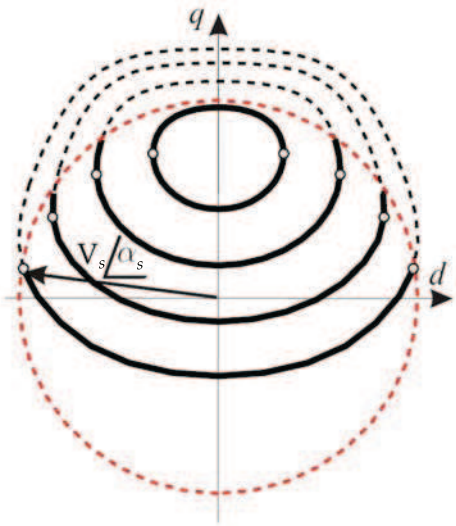

(d) Hub motor voltage.

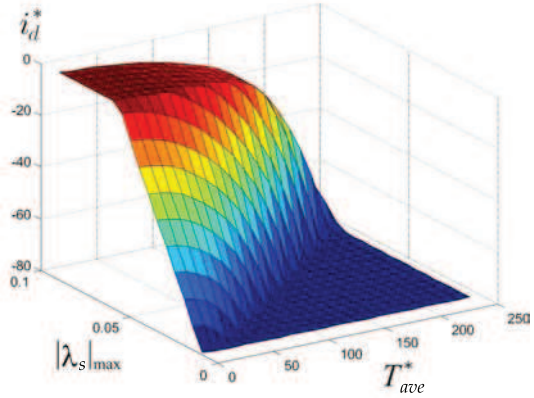

(e) Hub motor i_d reference.

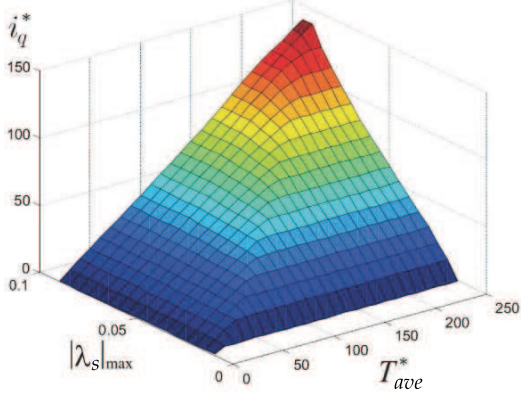

(f) Hub motor i_q reference.

Figure 6.2: FE results and torque control LUTs.

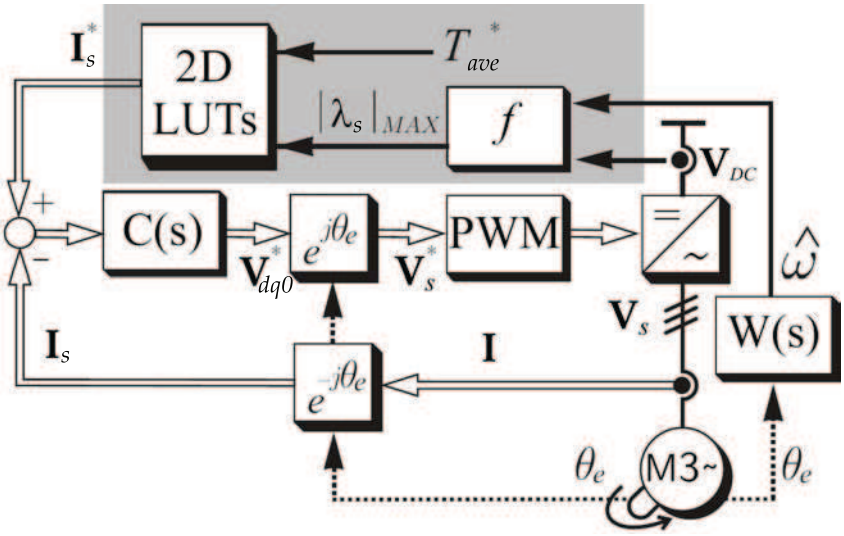

Figure 6.3: Torque control block diagram.

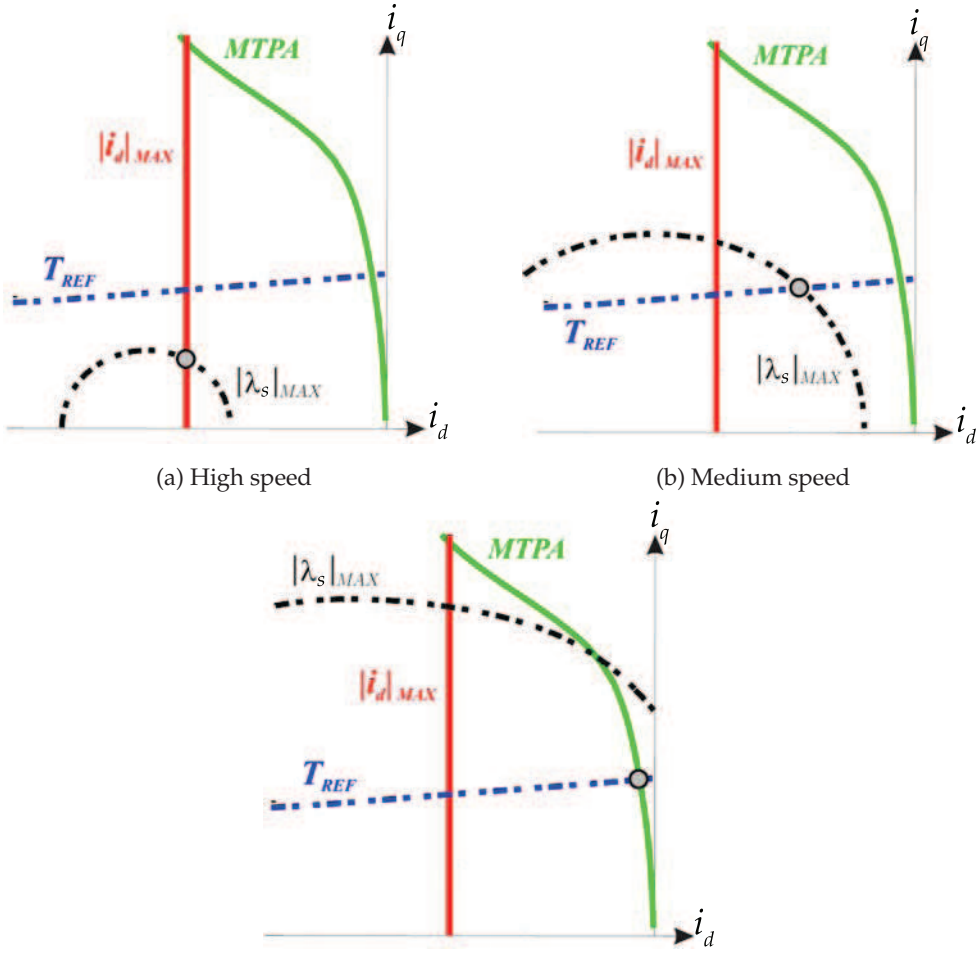

(a) High speed

(b) Medium speed

(c) Low speed

Figure 6.4: Three examples during torque control lookup table creation.

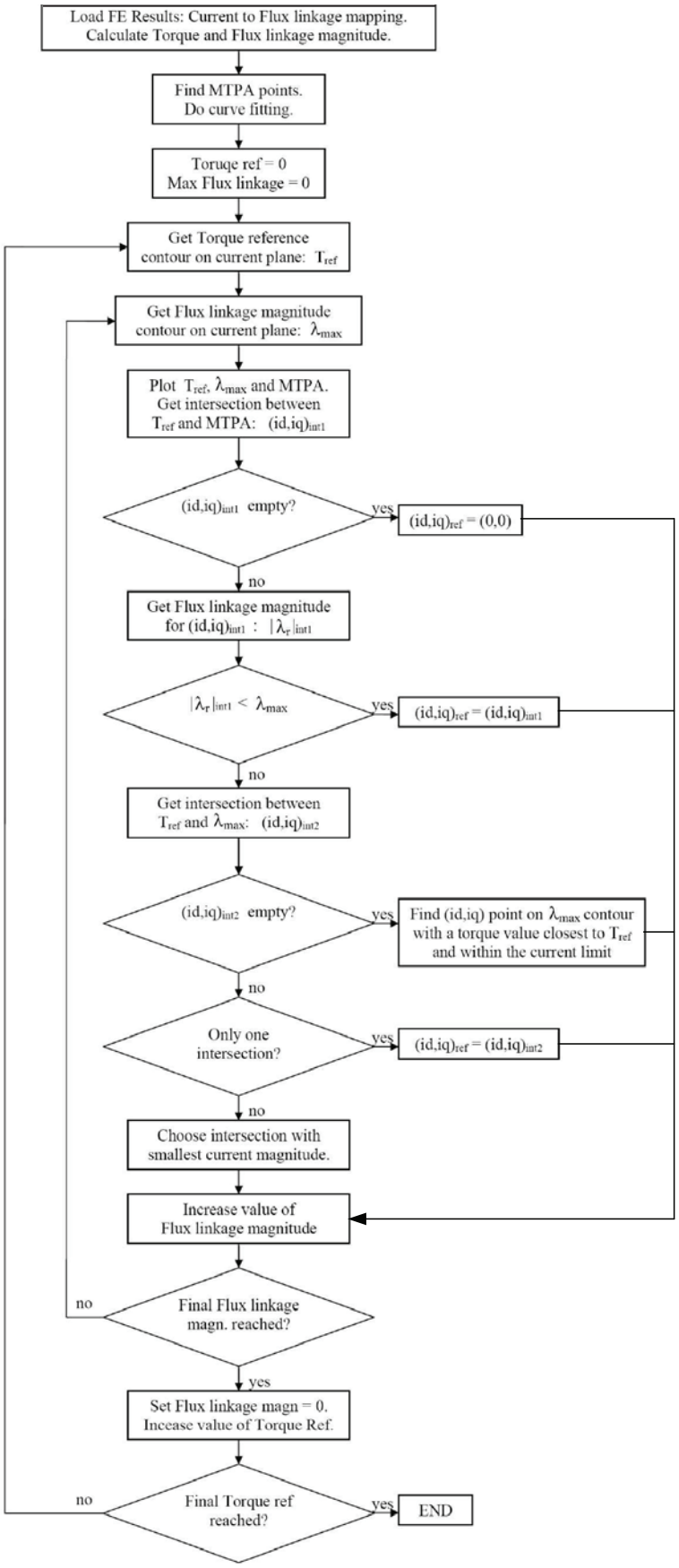

Figure 6.5: 2D LUTs setup program.

CHAPTER 7

PROTOTYPE DESIGN, CONSTRUCTION AND TESTING

To verify the accuracy of the FE results of the PM hub motor designs, two prototype machines (Hub motor 1 and Hub motor 2) were built and tested. The first prototype is a double layer open slot machine with interior magnets having a pole/slot combination of 40/30. The second prototype is a double layer semi-closed slot machine with embedded magnets having a pole/slot combination of 30/27. The FE design and mechanical construction as well as the various tests performed on these machines are described in this chapter.

7.1 Hub motor 1

7.1.1 FE design optimization

With a pole-slot combination of 40 poles and 30 slots the working harmonic winding factor is 0.866, the lowest common multiple (LCM) value is 120 and the greatest common divisor (GCD) value is 10. The design optimization is based on the minimization of the active mass, M, of the machine. While minimizing the active mass of the machine it still has to generate a certain minimum torque, T_{min}, not exceed a specified torque ripple limit, $T_{rip_{min}}$, and be within the current density limit, J_{max}. The constrained objective function, as discussed in Chapter 5, Section 5.4, is expressed as

$$Y = F(\mathbf{X}) = M(\mathbf{X}) + \sum_{i=1}^{3} w_i \varepsilon_i, \tag{7.1}$$

where w_i is the weighting factor of the penalty ε_i, defined as

$$\varepsilon_1 = \left\{ \begin{array}{cc} (T_{min} - T_{ave})^2 & : T_{min} > T_{ave} \\ 0 & : T_{min} \leq T_{ave} \end{array} \right\} \tag{7.2}$$

$$\varepsilon_2 = \left\{ \begin{array}{cc} (T_{rip} - T_{rip_{min}})^2 & : T_{rip} > T_{rip_{min}} \\ 0 & : T_{rip} \leq T_{rip_{min}} \end{array} \right\} \tag{7.3}$$

$$\varepsilon_3 = \left\{ \begin{array}{cc} (J - J_{max})^2 & : J > J_{max} \\ 0 & : J \leq J_{max} \end{array} \right\}. \tag{7.4}$$

The layout of the machine shown in Fig. 7.1 is the result of the FE optimization, with the machine parameters given in Table 7.1.

7.1.2 Construction

The manufacturing of the various hub motor parts was outsourced, but the assembly and winding wiring was done in house. The following sections are a build pictorial of hub motor 1.

7.1.2.1 Stator

The stator core, that also served as the main axle, with the enclosed cooling channels is shown in Fig. 7.2a. After the channels are sealed the stator laminations are press fitted. The completed assembly is shown in Fig. 7.2b.

Preformed coils are used to fit on the stator laminations. These coils are wound on a winding machine using a jig of dimensions similar to the stator teeth. The assembly of the stator coils, with 21 turns of rectangular copper wire, is shown in Fig. 7.3. Figure 7.3a shows one coil fitted to the stator and Fig. 7.3b shows 4 coils fitted. It is important to note that insulation is used to isolate the copper and stator laminations and to protect the copper from the sharp edges of the laminations. With all the coils fitted, the different views of the stator, at this stage, are shown in the last three figures of Fig. 7.3.

After the coil assembly, the separate coils are connected to form 3 phases with 2 parallel circuits each. To secure the coils, and make the assembly resilient to vibrations, the stator is encapsulated in an epoxy resin. The stator is put into a mould after which the cold curing epoxy resin is added and then cured. To increase the glass transition temperature of the epoxy,

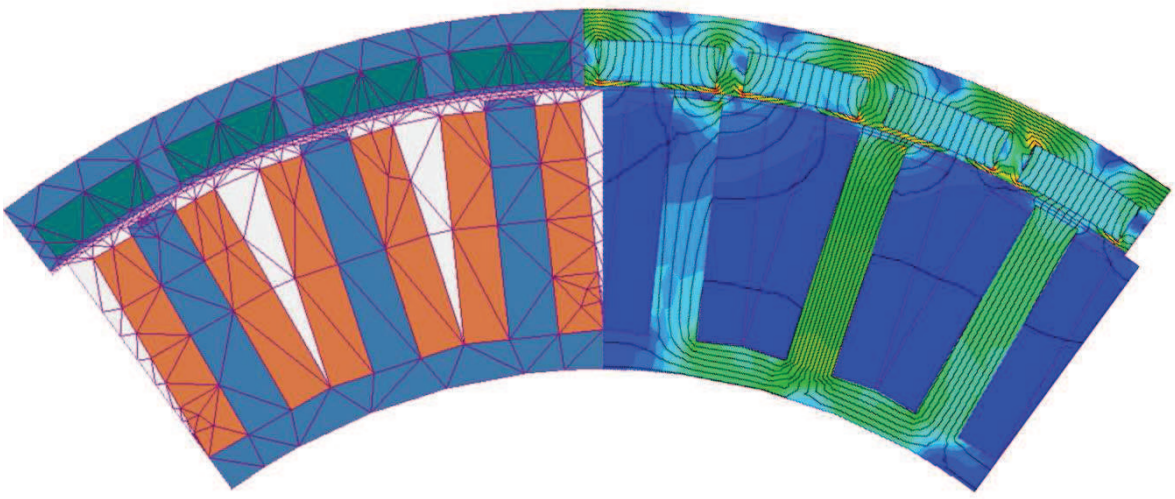

Figure 7.1: Section of the modeled 40-pole/30-slot Hub motor 1.

Table 7.1: Dimensions, rated values and related information of hub motor 1.

Poles	40	Slots and Coils	30
Rotor outer diameter	270 mm	Stator outer diameter	247 mm
Rotor inner diameter	249 mm	Stator inner diameter	171.9 mm
Axial length	80 mm	Active mass	15.58 kg
Magnet pitch	7.3°	Magnet height	5.54 mm
Slot height	32.69 mm	Tooth height	32.69 mm
Coil width	6.17 mm	Tooth width	6.72 mm
Number of turns per coil	21	Number of parallel circuits	2
Current density	8.4 A.mm^{-2}	Phase resistance	31.82 mΩ
Rated voltage	120 V rms	Rated current	93 A rms
Power	10 kW	I^2R losses	1 kW
Torque	200 Nm	DC bus	120 V
Base speed	465 r/min	Magnet type	Nd-Fe-B

it is left to cure for 1 day at room temperature after which it is baked at 100 $^{\circ}C$ for 4 hours. This increases the glass transition temperature from $\pm$ 66 $^{\circ}C$ to 130 $^{\circ}C$. Figure 7.4 shows the completed stator and the mould used for the casting.

Two temperature sensors, (thermo-couples in this case) were inserted between two random coils before casting. These thermo-couples are used to determine the temperature of the copper during operation.

7.1.2.2 Rotor

The rotor consists of the outer shell (Fig. 7.5a), the rotor laminations and the magnets. The laminations are press fitted to the outer shell before the magnets are inserted (Fig. 7.5b). The magnets slide into the lamination pockets and are secured in-place, during operation, by the second part of the rotor shell that blocks off the holes. The complete active rotor part is shown in Fig. 7.5c and Fig. 7.5d.

In this case the rotor was skewed using two sections. The first section's laminations were inserted, after which the magnets were inserted. Then the next stack of rotor laminations was

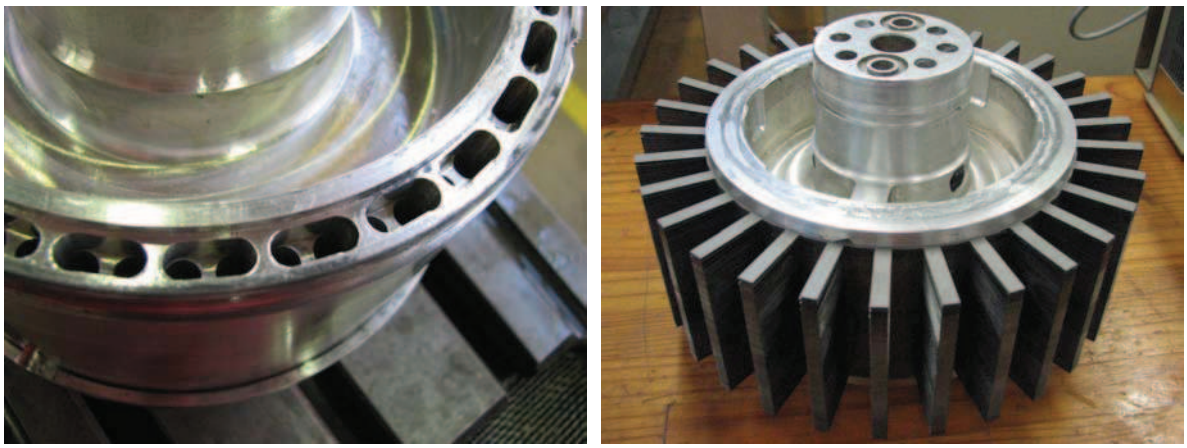

(a) Cooling channels (b) Lamination assembly

Figure 7.2: The first steps in the stator construction.

placed, but rotated slightly. This rotation angle was implemented by using two key ways in the rotor outer shell to help align the laminations. These key ways in the rotor shell can be seen in Fig. 7.5a and constitute a rotor mechanical skew angle of 1.5°.

7.1.2.3 Motor

With the stator and rotor completed, the motor is assembled. Due to the internal magnets and the relatively thin stator teeth, the attraction force between the rotor and stator is not that large, and assembly is easy, a matter of fitting the bearings and pushing everything together. No jig or setup time was required for assembly or disassembly, and this is an advantage of this topology. The assembled machine can be seen in Fig. 7.6a still requiring the fitting of the position sensor. With the position sensor fitted, the machine is closed and now completely sealed (Fig. 7.6b). Figure 7.6c and 7.6d show the complete machine with the rim and tyre fitted.

7.1.3 Torque control

A torque control scheme, that is explained in Chapter 6, is first simulated using Matlab and then implemented using a digital signal processor (DSP) that commands the 3-phase inverter. With all the finite element results available for this machine, the implementation of the algorithm and the generation of the required lookup tables can be done relatively fast.

Figure 7.7 shows the dq-axis current references used to obtain maximum torque per ampere through the whole speed range.

7.1.4 Experimental setup

The mechanical experimental setup consists of the hub motor, torque sensor, gearbox, fly-wheel and a 37 kW induction machine drive. The induction machine drive is used as a drive or load for the hub motor; by dissipating the energy in a dynamic brake resistor. The fly-wheel serves as a filter for torque ripple measurement. The gearbox, with a gear ratio of 1:3, is used to step up the speed of the hub motor and therefore to be a better match for the speed characteristics of the induction machine drive.

The electrical side of the power electronic drive consists of a 3-phase half-bridge inverter using 200 A IGBT modules and is supplied by a lead acid battery pack with a nominal voltage of 120 V. All 6 terminals of the 3-phase windings of the hub motor are made available, and for testing the water cooled hub motor is connected in a Y configuration.

The digital signal processor used for the drive system is a TMS 320 VC 33 DSP. This is a 20 MHz floating point processor that has to work with the current- , voltage- and position measured signals. With all the measurement information available a PI current controller is implemented in the DSP to maintain the correct phase currents according to the reference torque. The DSP has to calculate the correct PWM output signals for the inverter, based on the various measurements and inputs. The DSP is programmed using the C programming language to help reduce the execution time of the control algorithm. The control block diagram is shown in Fig. 6.3.

A diagram of the test setup can be seen in Fig. 7.8 with pictures of the actual setup shown in Fig. 7.9. After laboratory testing the drive was mounted on a small utility vehicle, as shown in Fig. 7.10, for some field testing. Unfortunately due to project constraints little testing was done with the drive on the vehicle.

7.1.5 Results

To confirm the results obtained from the FE analysis, as well as to obtain the parameters of the machine, certain tests were performed on the prototype in the laboratory. The results are shown and discussed in the following sections.

7.1.5.1 Open circuit

The open circuit voltage versus speed profile of the motor is measured. This is done by driving the motor at different speeds using the induction motor drive. The hub motor speed is increased in steps of 100 r/min up to 1200 r/min (which would equal $\pm$ 120 km/h vehicle speed).

The measured voltage values are slightly lower than the calculated values as shown in Fig. 7.11. This is due to the manufacturing tolerances of the magnets. When measuring the dimensions of the magnets it was found that the magnets were manufactured on the low side of the specified tolerance, and the loss in magnet volume correlates to the loss in voltage shown in Fig. 7.11. Except for this small difference, there is good correlation on amplitude and the waveform between the measured and calculated open circuit voltage of the prototype.

7.1.5.2 Short circuit

For safety reasons the short circuit operation of the hub motor is of some importance in vehicle applications. Specifically at high speeds a total short circuit at the inverter terminals could cause catastrophic results depending on the way the motor responds. Due to the relatively high impedance of the prototype design, the short circuit torque at high speeds is about 10% of the rated torque as shown by the torque versus speed curve of Fig. 7.12. This behaviour is very good when considering vehicle performance under extreme conditions such as a short circuit[14] of the 3-phase hub motor.

7.1.5.3 Load

The operation of the hub motor drive under steady state load conditions was tested with the drive/load induction machine always running at a constant speed.

For the first load test the hub motor was run at 100 r/min (well below base speed) to test the torque output versus current amplitude and current angle. The results of this test are shown in Fig. 7.13, with the markers indicating the measured values, and the solid lines indicating the FE predicted results. The test was performed at $\frac{1}{3}$, $\frac{2}{3}$ and full load current with the current angle varied through two quadrants including motoring and generating mode.

The hub motor was designed with the given specifications of a drive consisting of full-bridge inverter using a 120 V DC supply. Only being able to test with a half-bridge inverter reduced the output voltage by a half and the torque versus speed performance is scaled accordingly. The measured test data as well as the appropriate calculated data are shown in Fig. 7.14. Good correlation between the measured and calculated data is shown. The torque versus speed measurements were done with the proposed control algorithm, described in Chapter 6, implemented on the DSP. This shows good steady state performance and confirms the accuracy of the simulated results.

[14] In the measurement setup all the machine phase terminals were connected to create a short circuit.

7.1.6 Conclusion

The volume restriction of the hub motor meant that the mechanical designers had to use every little space available to fit the required components. The building of the machine required careful consideration at each step due to the unfamiliar terrain. When building the machine, tolerances had to be double checked regularly to ensure the correct fit of all components.

Tests showed that the measured data and FE results of the prototype are in excellent correlation with each other. The load tests through the whole speed range, using the proposed control algorithm, show good correlation with the simulated results.

Although this hub motor's pole-slot combination results in a low winding factor, a relatively good performance is obtained, which confirms the results of the comparison done in Chapter 5.

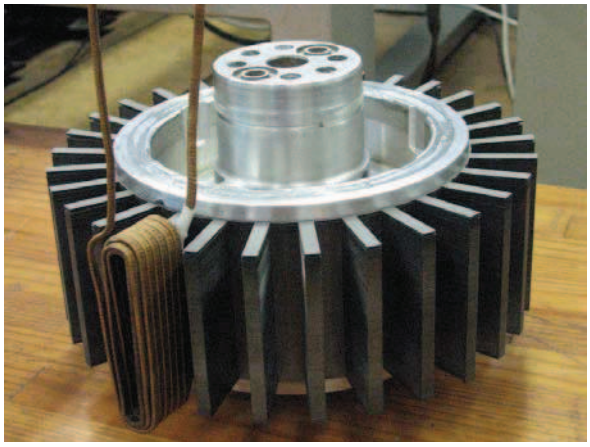

(a) First coil

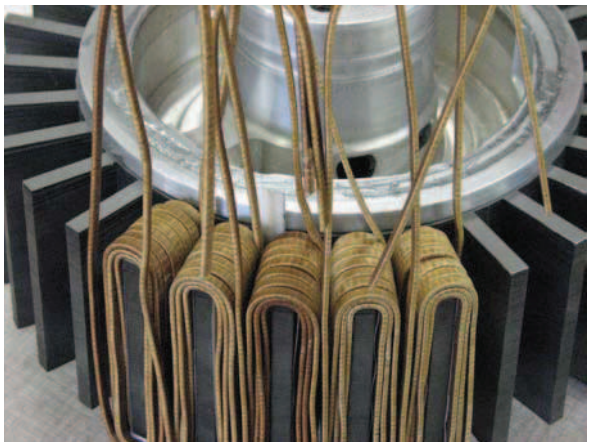

(b) Four coils assembled

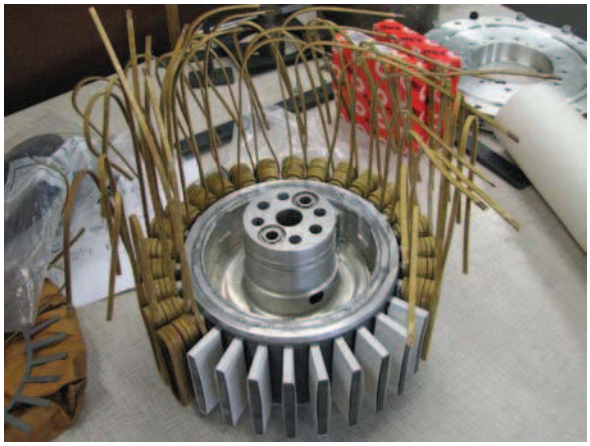

(c) Teeth insulation

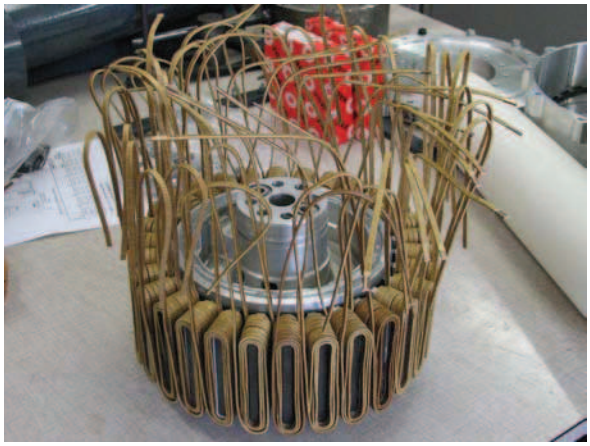

(d) 30 Coils assembled - top view

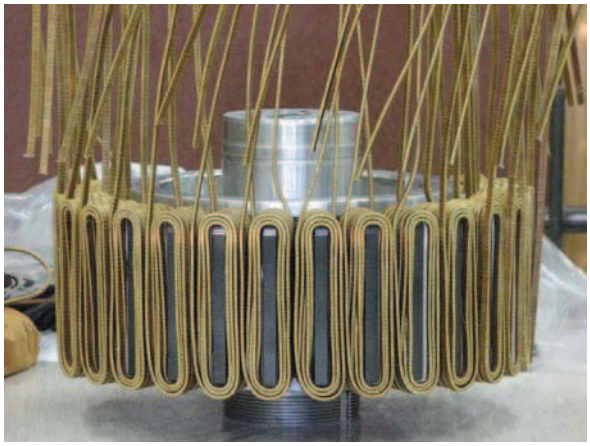

(e) 30 Coils assembled - side view

(f) 30 Coils assembled - bottom view

Figure 7.3: Assembling the coils on the stator.

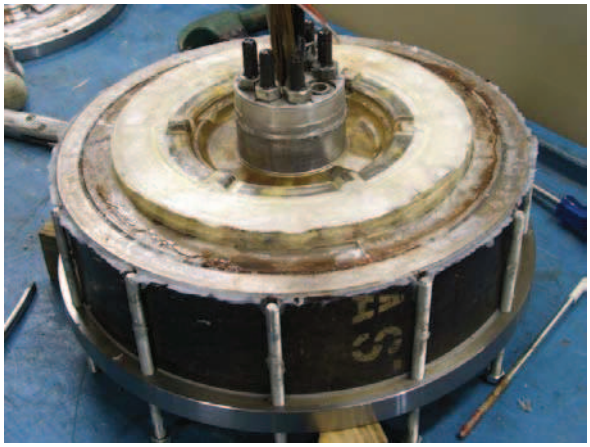

(a) Mould top cover removed

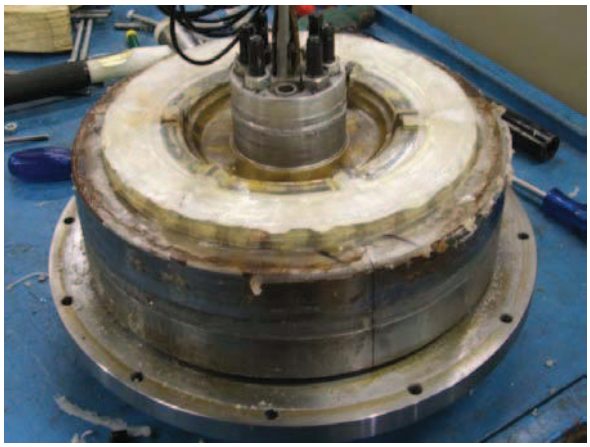

(b) Mould outer removed

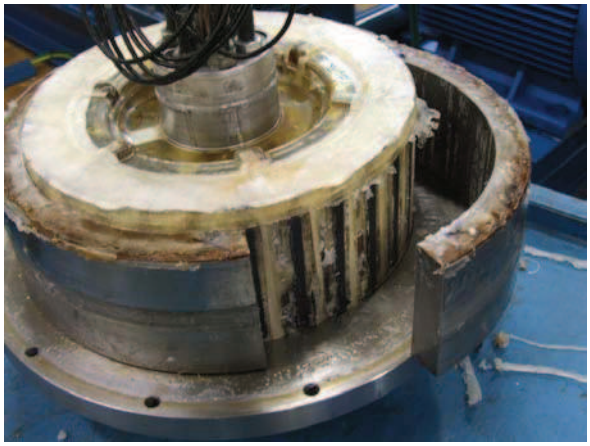

(c) Removing mould inner

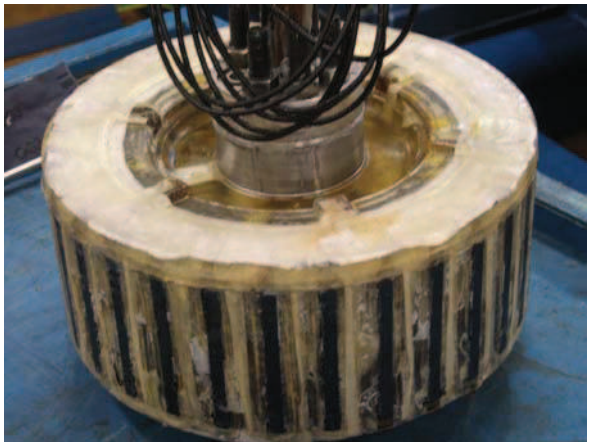

(d) Mould removed

(e) Windings is completely covered by epoxy

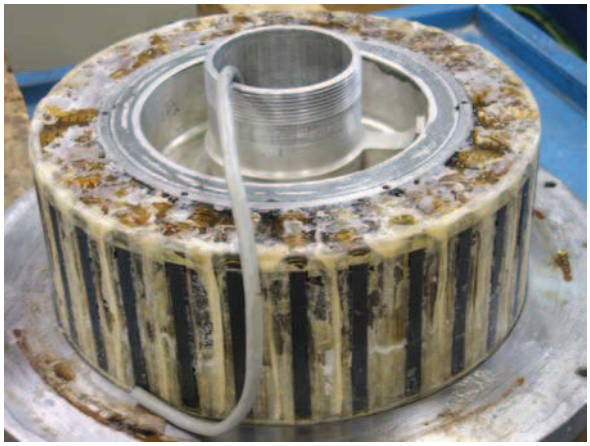

(f) Resolver cable coming out from the centre hub

Figure 7.4: Completed 30-slot stator with straight teeth.

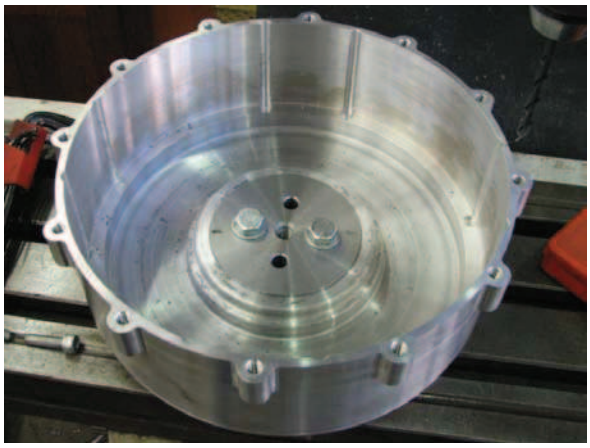

(a) Rotor outer shell

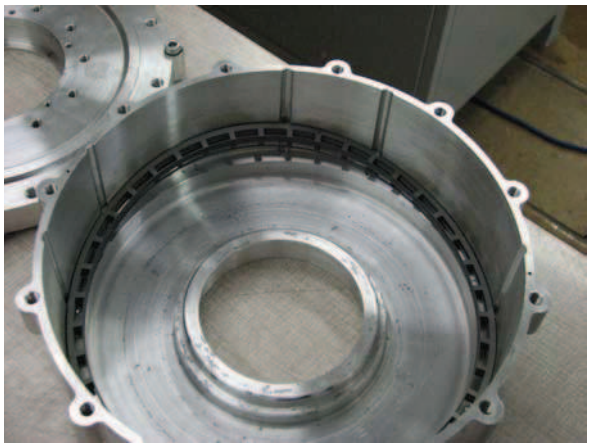

(b) Lamination fitting

(c) Finished rotor

(d) Close-up view of the interior magnets

Figure 7.5: Rotor assembly.

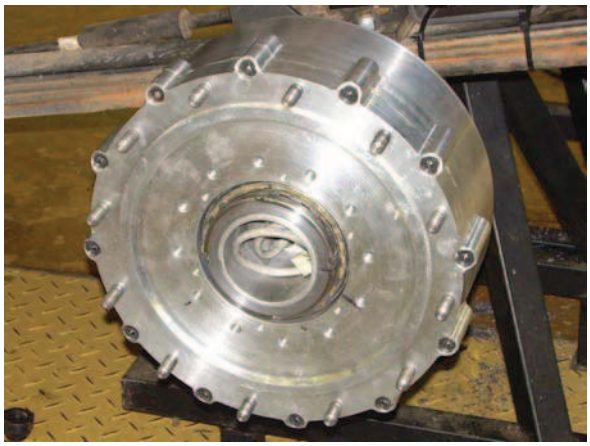

(a) Motor assembled without resolver cover plate

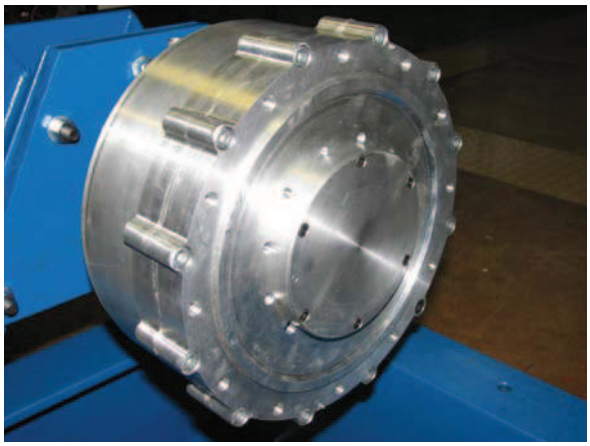

(b) Resolver cover plate fitted

(c) Rim and tyre fitted - front view

(d) Rim and tyre fitted - rear view

Figure 7.6: Assembled hub motor 1 ready for testing.

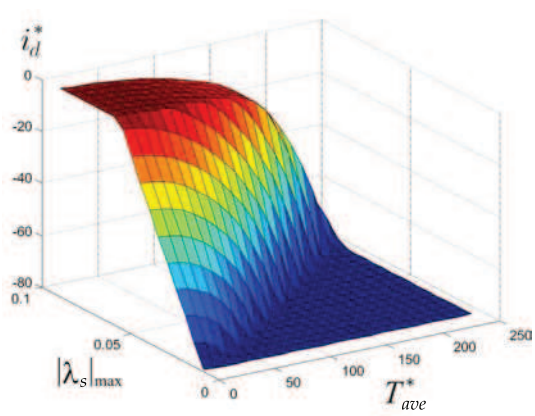

(a) HM1 i_d reference.

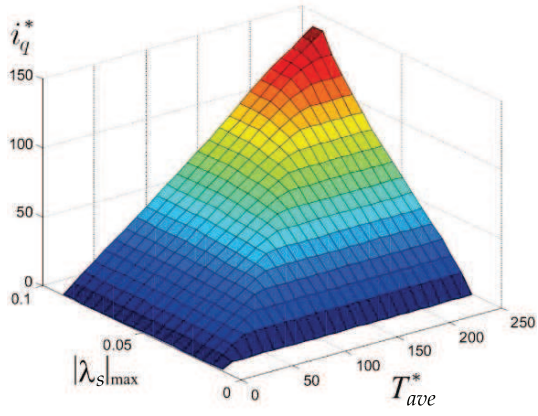

(b) HM1 i_q reference.

Figure 7.7: Torque control LUTs for hub motor 1.

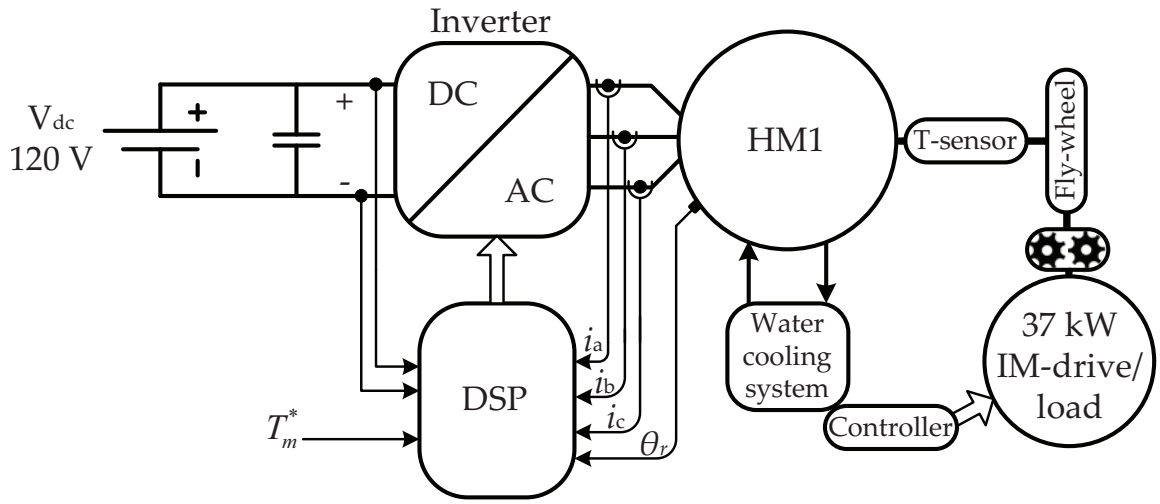

Figure 7.8: Test setup diagram for Hub motor 1.

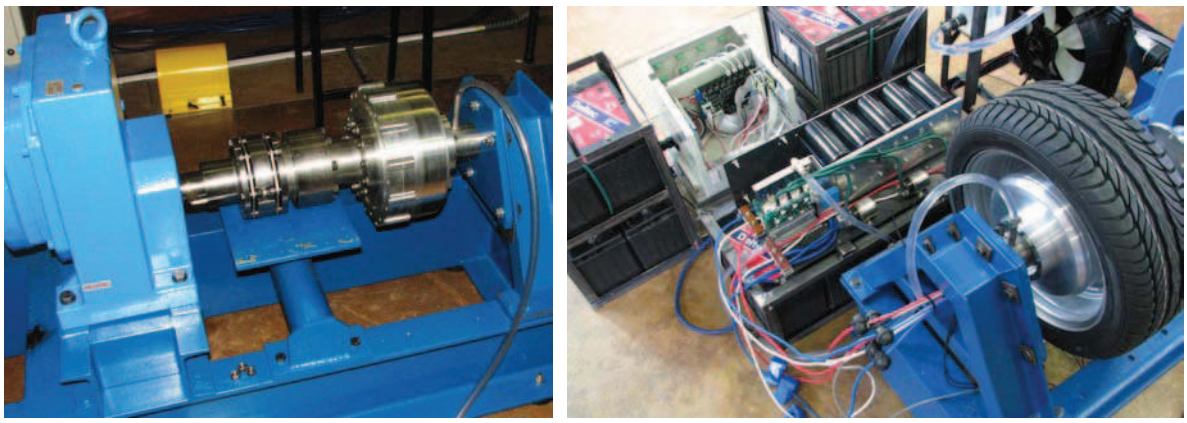

(a) Hub motor 1 connected to the gearbox

(b) Hub motor 1 ready for testing

Figure 7.9: Hub motor 1 laboratory test setup.

(a) Motor mounted on test vehicle

(b) Test vehicle ready to be driven

(c) View of rear axle and suspension setup

(d) Laboratory setup is moved to the test vehicle

Figure 7.10: Hub motor 1 field test setup.

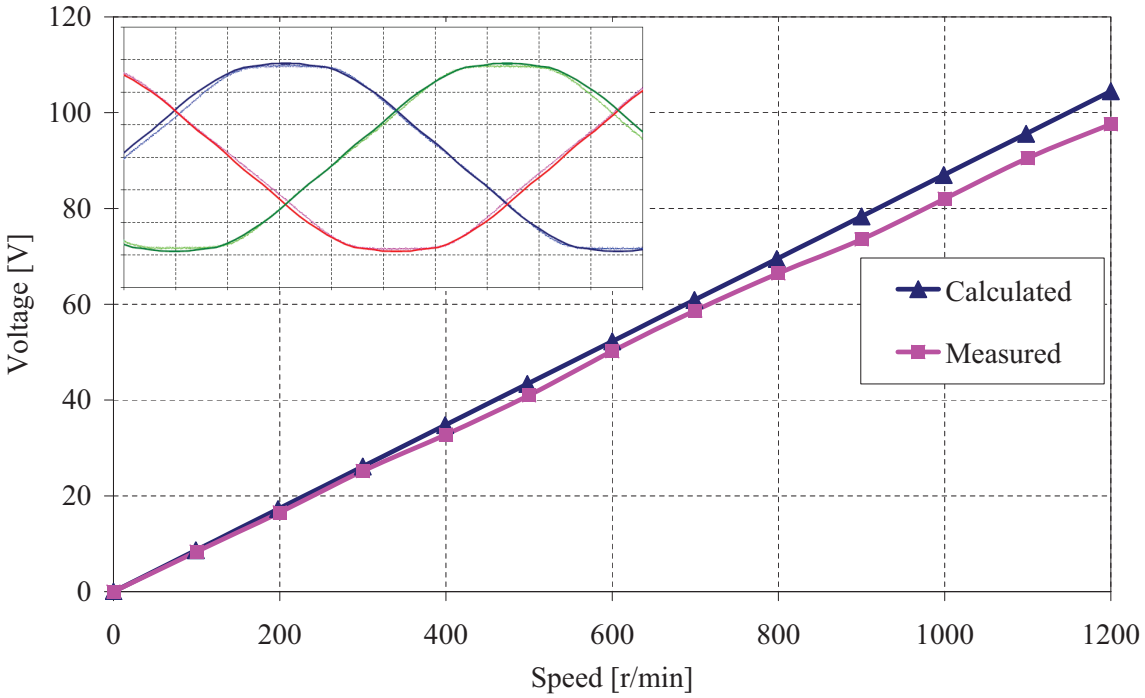

Figure 7.11: The measured and calculated open circuit voltage of Hub motor 1

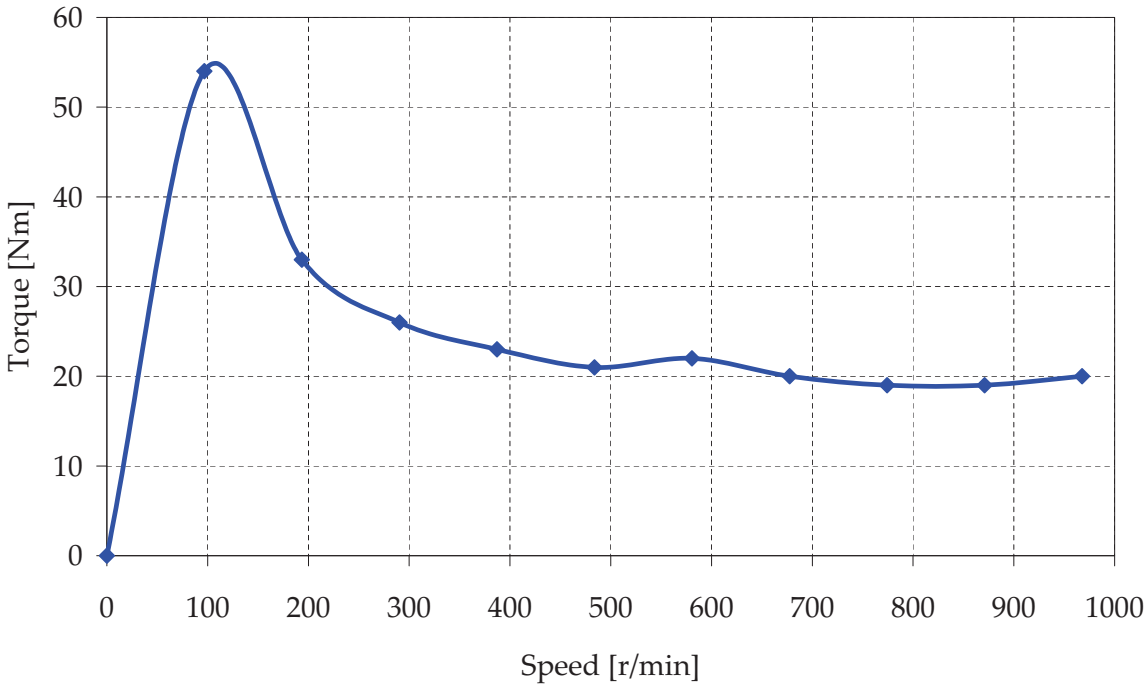

Figure 7.12: The measured torque of Hub motor 1 when short circuited

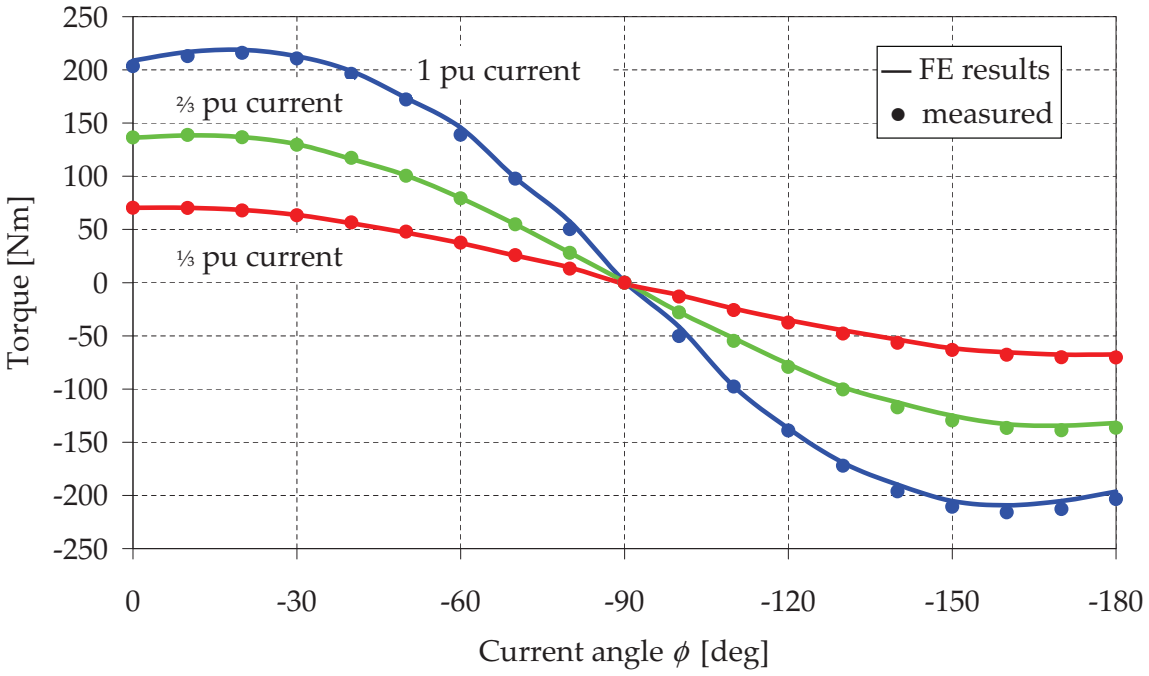

Figure 7.13: Measured and calculated torque vs. current angle of Hub motor 1 with per unit load current a parameter.

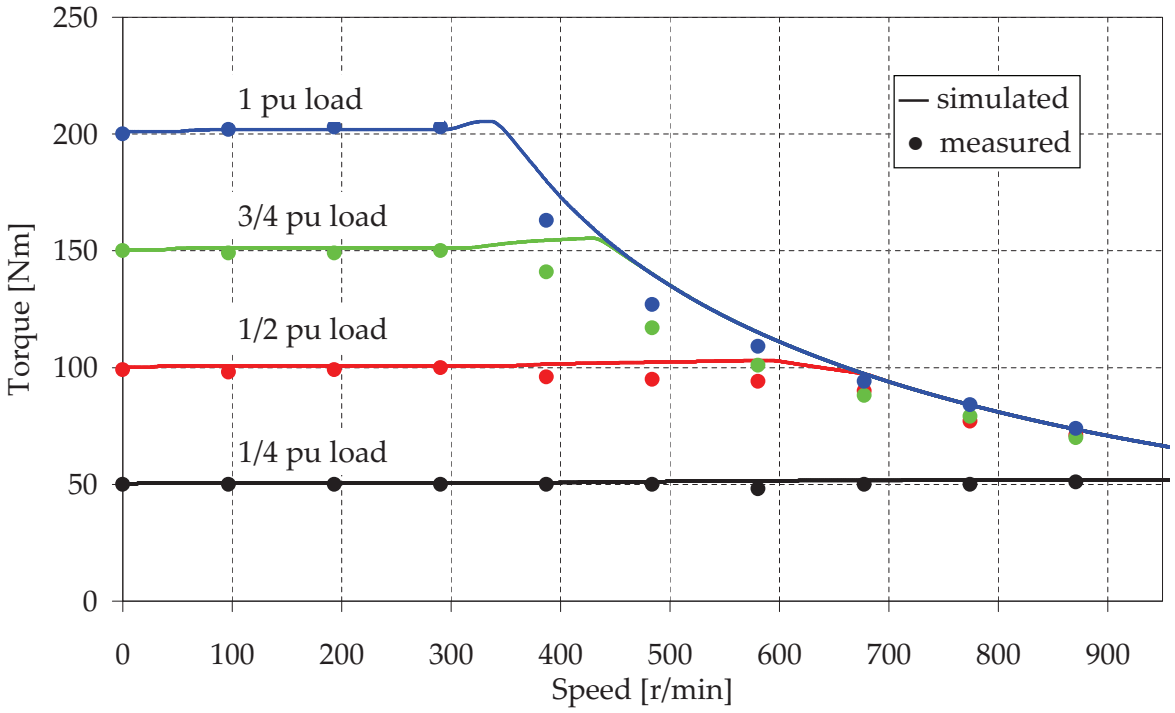

Figure 7.14: Measured and simulated torque vs. speed of Hub motor 1 with load a parameter.

7.2 Hub motor 2

7.2.1 FE design optimization

For the second prototype hub motor a pole-slot combination of 30 poles and 27 slots was chosen. This pole-slot combination has a winding factor of 0.945, a LCM value of 270 and a GCD value of 3. The average torque, T_{ave}, of the machine is maximized in the design optimization. While maximizing the torque of the machine, the current density limit J_{max}, must not to be exceeded. The current density is used in the constraint optimization as parameter by modifying the objective function. A weighted penalty function, that assigns a positive penalty for increased constraint violation, is added to the objective function. The objective function is then defined as

$$Y = F(\mathbf{X}) = T_{ave}(\mathbf{X}) - w\varepsilon, \tag{7.5}$$

where w is the weighting factor of the penalty ε, defined as

$$\varepsilon = \left\{ \begin{array}{cc} (J - J_{max})^2 & : J > J_{max} \\ 0 & : J \leq J_{max} \end{array} \right\}. \tag{7.6}$$

The machine in Fig. 7.15 is the result of the FE design optimization, with the machine parameters given in Table 7.2.

7.2.2 Construction

Semi-closed stator slots are chosen for the second hub motor's stator design, such as in Fig. 5.3b. This slot design prohibits the used of preformed coils and complicates winding the double layer windings. This typically results in a lower filling factor and takes more time to complete. To overcome this and to be able to use preformed coils, the stator laminations are manufactured in two parts. The yoke and the teeth are separated so that the teeth are fixed after installing a preformed coil. The coil is pushed onto the loose iron laminated stator tooth, and then the assembly is fixed onto the stator yoke. This is illustrated in Fig. 5.4b. The detail construction is shown and discussed below.

An embedded PM rotor configuration was chosen for the second hub motor prototype. An example of this configuration is shown in Fig. 5.8b. This topology is simpler than the fitting of surface mounted PMs on the rotor. It is still necessary to glue the magnets to the rotor laminations. The assembly of the magnets and rotor laminations is easy in this case, but it does take more time than for the interior PM topology.

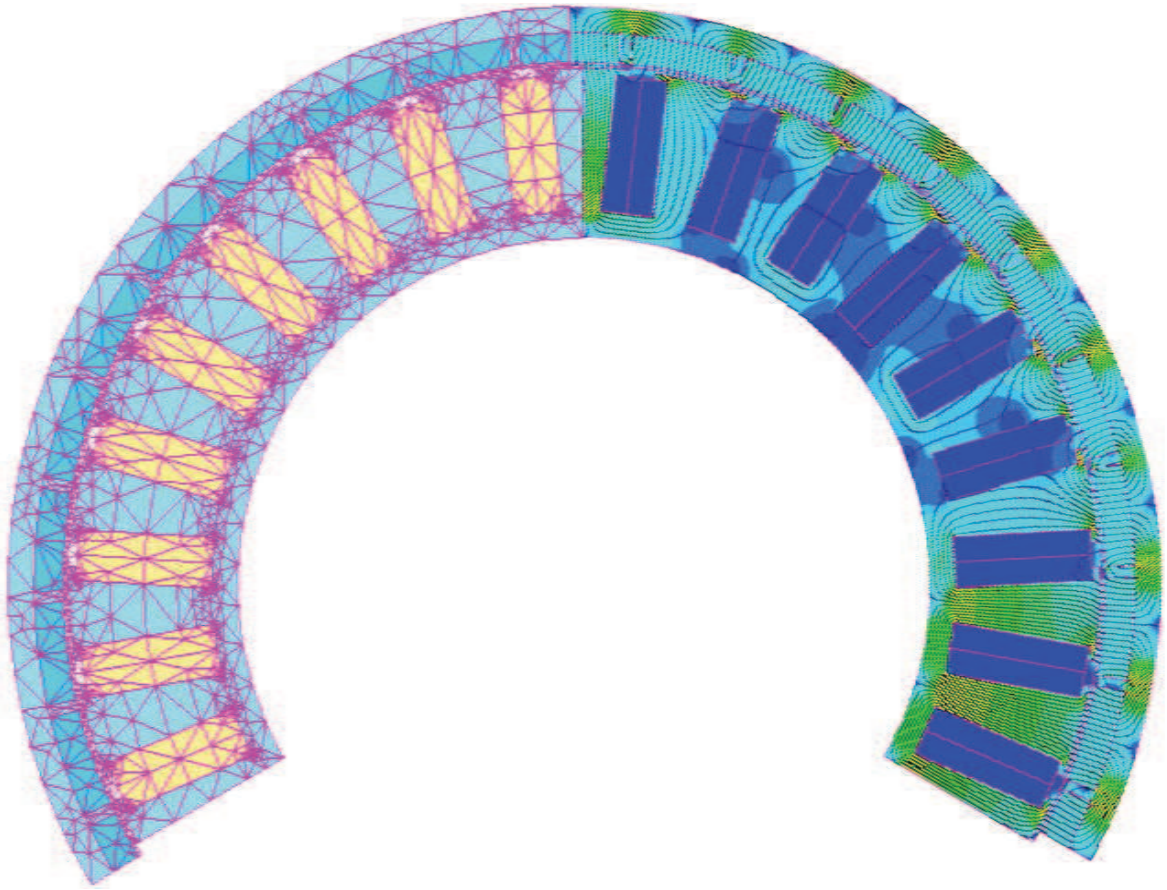

Figure 7.15: Section of the modeled 30-pole/27-slot hub motor 2.

7.2.2.1 Stator

The stator yoke core, with enclosed cooling channels, is shown in Fig. 7.16a. The stator yoke laminations are press fitted, and the completed yoke assembly is shown in Fig. 7.16d.

Due to the semi-closed stator slots, and their outwards taper, fitting preformed coils is impossible. Preformed coils can only be pushed onto the teeth if they are loose from the stator yoke as shown in Fig. 5.4b. To use loose teeth, but still be able to secure them tightly to the stator yoke, the mechanical design is altered. This alteration consists of making the stator teeth with lips that can slide into slots in the stator yoke lamination stack shown in Fig. 7.16d. This puzzle type of assembly ensures secure location of the stator teeth without any extra fixtures or glue. The slots in the stator yoke laminations can be seen in Fig. 7.16 with the lips on the teeth and part-assembly shown in Fig. 7.17b.

The stator tooth laminations have to be assembled separately to fit the preformed coils, before the tooth stack and coil unit is slided onto the stator yoke. The stator tooth laminations are assembled using a mould, shown in Fig. 7.17a, and some glue to keep the laminations together until final fitment. The preformed coils are then fitted on to the tooth stack as shown

Table 7.2: Hub motor 2 dimensions, rated values and related information.

Poles	30	Slots/Coils	27
Rotor outer diameter	270 mm	Stator outer diameter	241.1 mm
Rotor inner diameter	243.9 mm	Stator inner diameter	162 mm
Axial length	100 mm	Active mass	22.02 kg
Magnet pitch	10.8°	Magnet height	7 mm
Slot height	31.9 mm	Tooth height	33.5 mm
Coil width	5.93 mm	Tooth pitch	13.33°
Number of turns per coil	51	Number of parallel circuits	3
Current density	11.5 A.mm^{-2}	Phase resistance	142.5 mΩ
Rated voltage	120 V rms	Rated current	53 A rms
Power	16 kW	I^2R losses	1.2 kW
Torque	340 Nm	DC bus	350 V
Base speed	450 r/min	Magnet type	Nd-Fe-B

in Fig. 7.17c and Fig. 7.17d.

Figure 7.18a shows two tooth-coil units fitted onto the stator yoke. After the tooth-coil assembly is fitted onto the stator yoke, the separate coils are connected to form three phases with three parallel circuits each. Some more pictures of the whole process are shown in Fig. 7.19, with the end result shown in Fig. 7.19f. Here the three phase wires can be seen together with the two black wires of the thermo couples that are used to monitor the winding temperature[15].

To secure the tooth-coil units and make the assembly resilient to vibrations, the stator is encapsulated in an epoxy resin. The stator is put into a mould after which the cold curing epoxy resin is added and then cured. Figure 7.20 shows the completed stator and mould used for the casting.

The completed stator, with the axle installed, is shown in Fig. 7.21. All the phase cables, thermo couple wires, cooling pipes etc. have to go through the hollow axle for connection on

[15]Notice that no electrical connection is visible in Fig. 7.19d, but all wires are covered with sleeving. Single wires that are routed to their points of connection are also covered by sleeving. All ferrule connections are covered and where they touch the cooling tank double the amount of sleeving is used to prevent ground faults.

the vehicle. The resolver, used for position feedback, is installed in the front part of the axle (as can be seen in Fig. 7.20f) during final assembling of the motor.

7.2.2.2 Rotor

The rotor consists of the outer shell (Fig. 7.22a), the rotor laminations and the magnets. The laminations are press fitted in the outer shell before the magnets are inserted (Fig. 7.22b). The magnets slide into the lamination pockets and are secured into place by the second part of the rotor shell that blocks off the ends. The magnets are glued to the rotor laminations but this step is actually not necessary since the wedge shape of the magnet slot in the laminations prevents the whole magnet from falling out and sticking to the stator laminations. The complete active rotor part is shown in Fig. 7.22d.

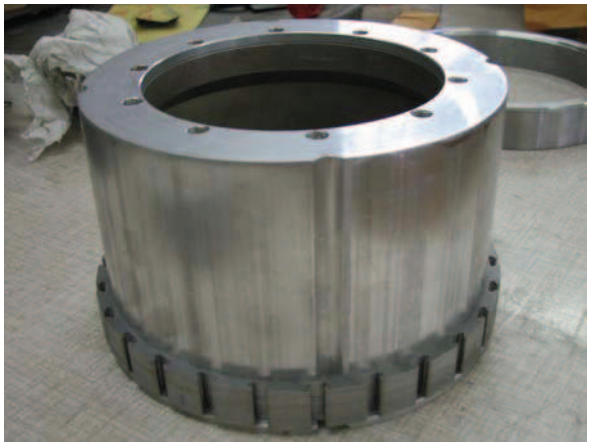

(a) Stator inner yoke - side view

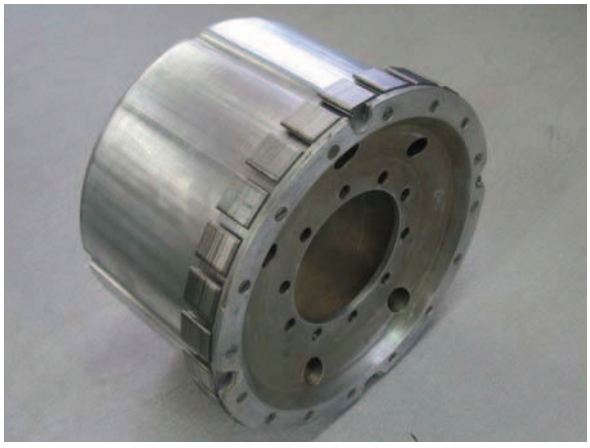

(b) Stator inner yoke - front view

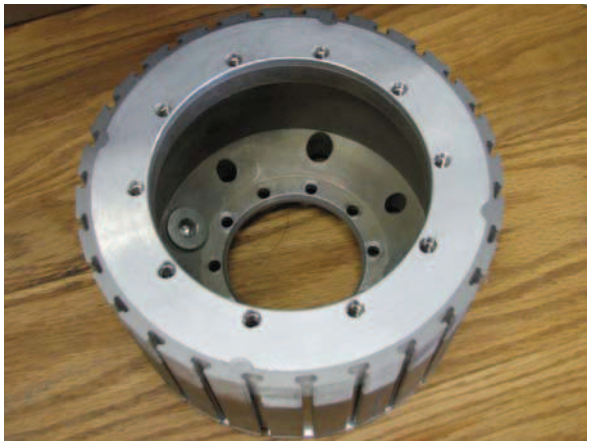

(c) Stator inner yoke - rear view

(d) Completed stator inner yoke

Figure 7.16: First steps in the stator construction, the inner yoke.

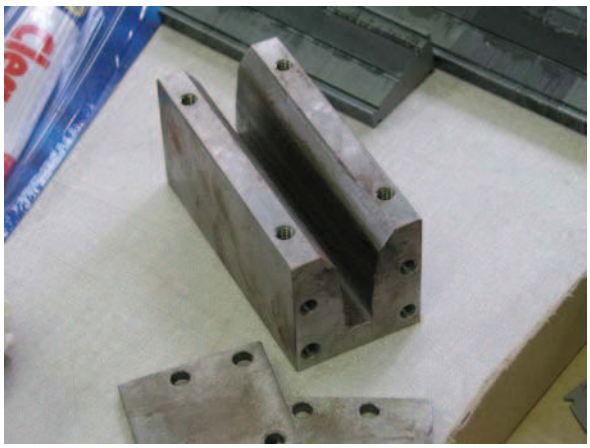

(a) Tooth mould

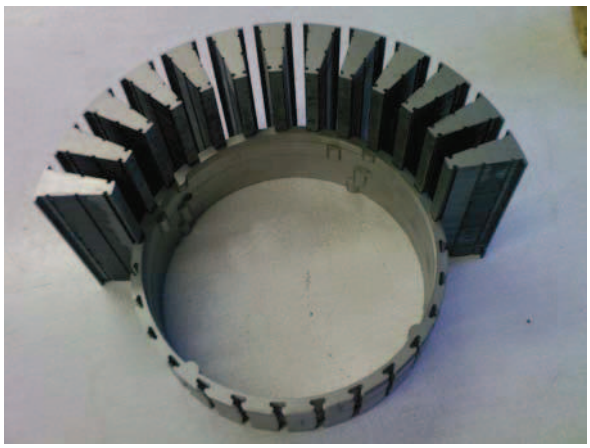

(b) Assembly of the stator teeth and yoke laminations

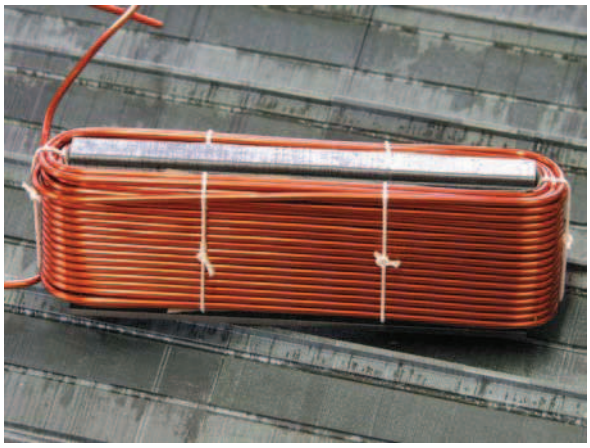

(c) Preformed coil on the laminated tooth - bottom view

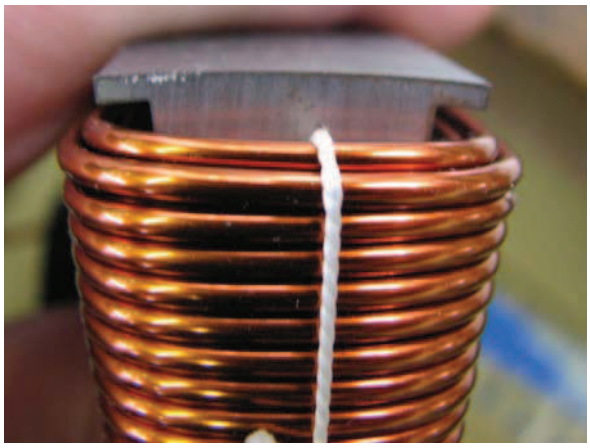

(d) Preformed coil on the laminated tooth - side view

Figure 7.17: Assembling the stator teeth and coils.

7.2.2.3 Motor

With the stator and rotor completed, the motor is assembled. Due to the open embedded magnets and the relatively large amount of stator iron, the attraction forces between the rotor and stator are great and assembly is not as easy as in the case with HM1. A special jig is required for assembling and disassembling and this is a disadvantage of this topology. The assembled machine can be seen in Fig. 7.23. Figure 7.23b shows the end plate used to couple the rotor via a bellows-coupling to the resolver. With the position sensor fitted, the machine is closed and then completely sealed (Fig. 7.23c). Figures 7.23e and 7.23f show the complete machine mounted to the A-frame that is to be used in the laboratory setup.

7.2.3 Torque control

As with hub motor 1, the torque control scheme that is explained in Chapter 6, is first simulated using Matlab, and then implemented using a DSP to command the inverter. With all the FE results available for this machine, the implementation of the algorithm and the generation of the required LUTs take place relatively fast. Figure 7.24 shows the dq-axis current references used to obtain maximum torque per ampere through the whole speed range for hub motor 2.

7.2.4 Experimental setup

The mechanical experimental setup is the same as for hub motor 1 as described in Section 7.1.4. A diagram of the test setup can be seen in Fig. 7.25 with pictures of the actual setup shown in Fig. 7.26. Figure 7.26b shows the integrated fixed point DSP and inverter. Unfortunately due to project constraints, little testing was done with the integrated DSP and inverter, due to ongoing development required on the DSP.

7.2.5 Results

To confirm the results obtained from the FE analysis as well as to parameterize the machine, certain tests were performed on hub motor 2 in the laboratory. For this part of the project two of the same protype hub motors were built and tested. The results are shown and discussed in the following sections.

7.2.5.1 Open and short circuit

The open circuit voltage versus speed profile of the second hub motor was measured. As shown in Fig. 7.27 the measured values are in good correlation with the calculated values for the prototype machine.

The resulting current versus speed curve for HM2 under short-circuit conditions is shown in Fig. 7.28, with the torque versus speed curve shown in Fig. 7.29.

7.2.5.2 Load

Load tests on HM2 are done in the same way as for HM1 as described in Section 7.1.5.3. The results of this test are shown in Fig. 7.30, with the markers indicating the measured values and the solid lines indicating the FE predicted results. Good correlation between the measured and calculated data is shown with some differences. These differences can be attributed to control issues that arose while using the fixed point DSP. Further development was necessary

to finalize the inverter and DSP design, and the torque performance through the whole speed range of HM2 could not be varified.

7.2.6 Conclusion

The test results show that the measured data and FE results of hub motor 2 are in good correlation with each other. The proposed control algorithm that can be used in the whole speed range of the drive, could unfortunetely not be implemented and tested on this prototype. Hub motor's 2 pole-slot combination results in a good winding factor, and good performance is obtained with less observed cogging torque than observed in hub motor 1. Cogging torque and torque ripple are difficult to measure and they are omitted from the practical measurements.

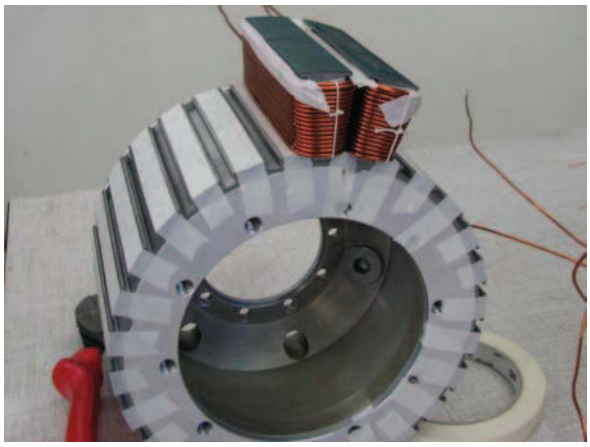

(a) Assembly of stator tooth-coil units

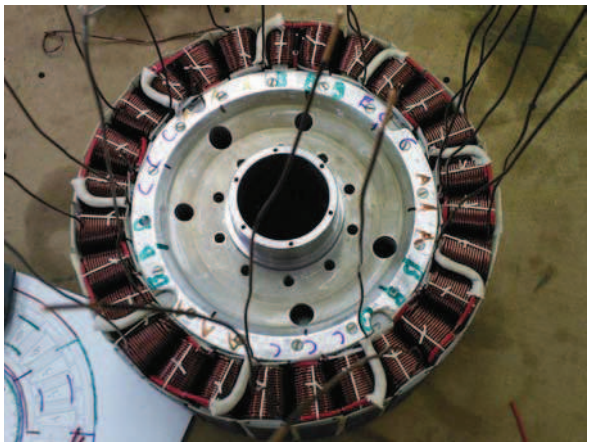

(b) Stotor coils being connected

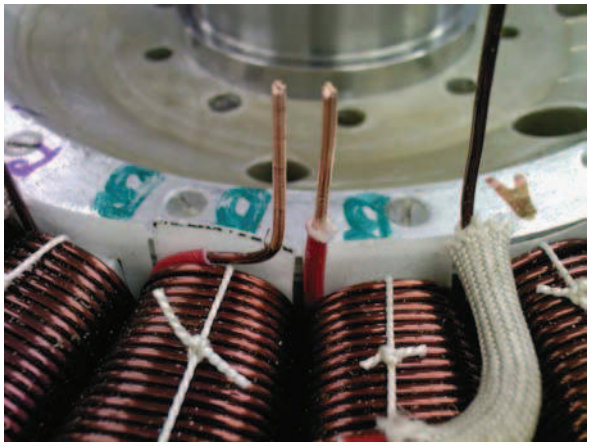

(c) Stripped coil terminals

(d) Connecting terminals with lugs

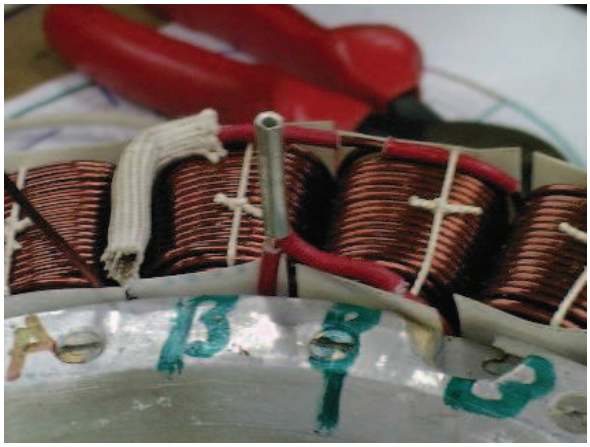

(e) Finished connection

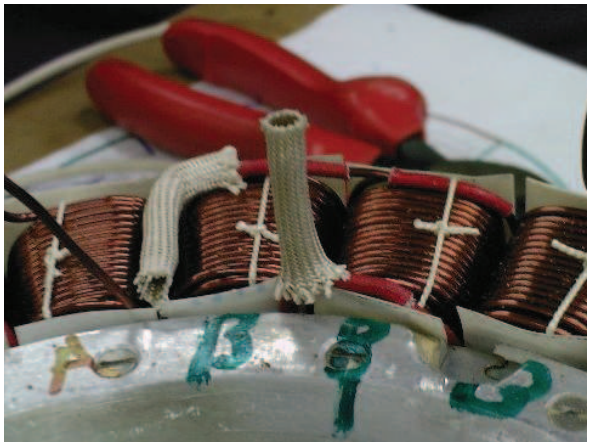

(f) Isolating the connection with some sleeving

Figure 7.18: Connecting the stator coils.

(a) Finished connection

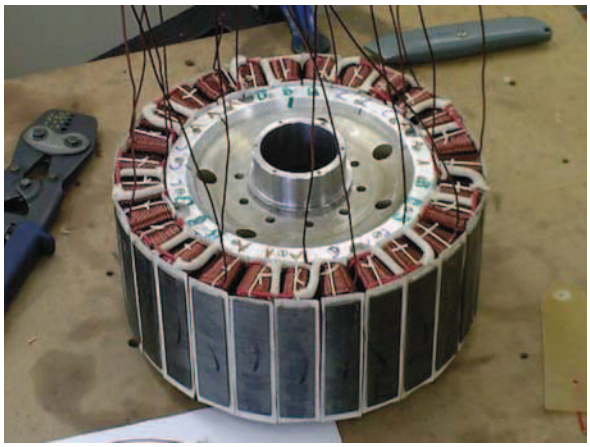

(b) A couple of connections still needs to be done

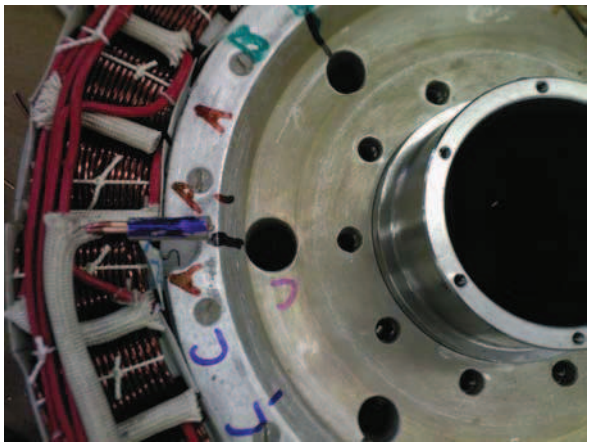

(c) A phase connection point

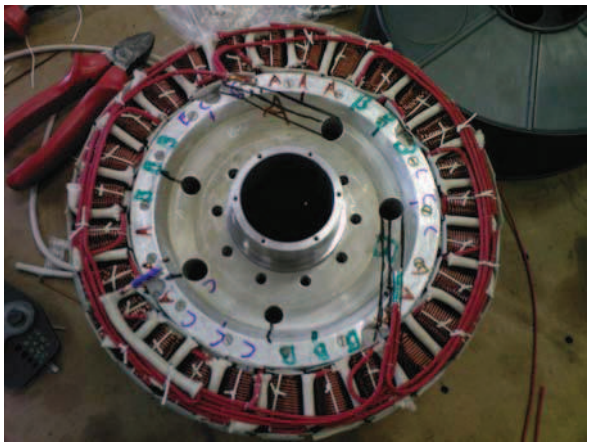

(d) 3-phase connection points

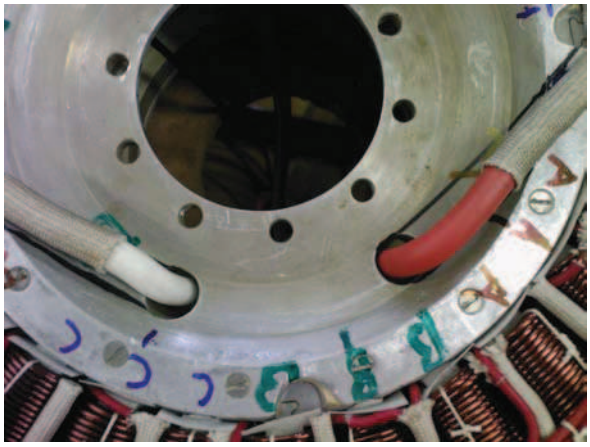

(e) Phase cables connected

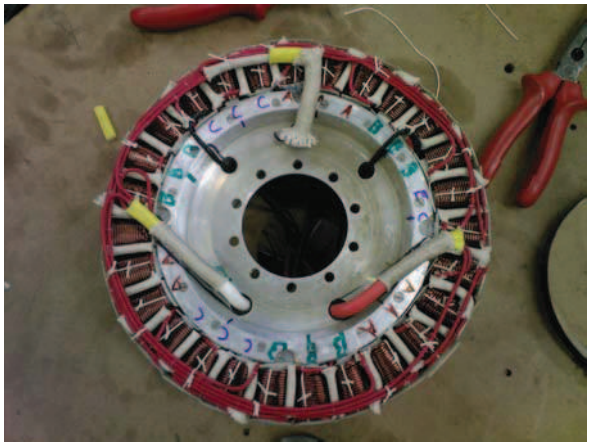

(f) Stator completely wired

Figure 7.19: Finishing the stator wiring.

(a) Stator mould

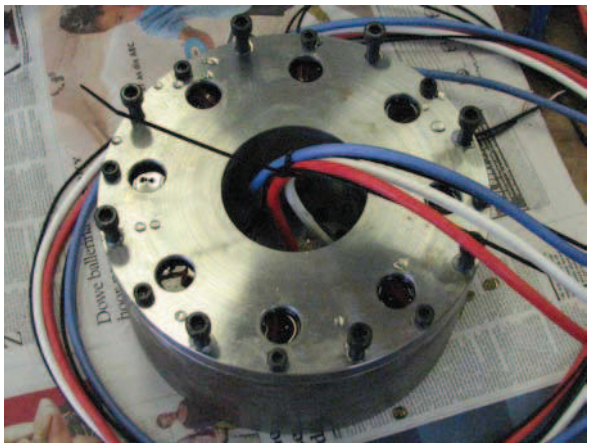

(b) Ready to be cured

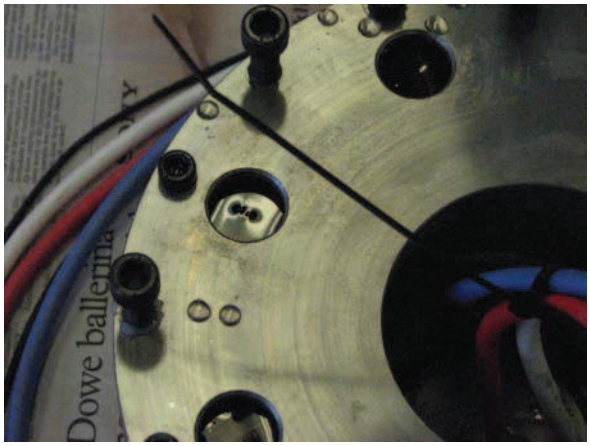

(c) Filling holes

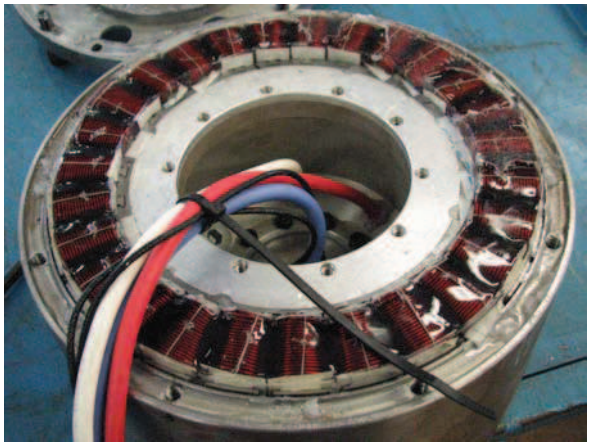

(d) Removing mould after curing

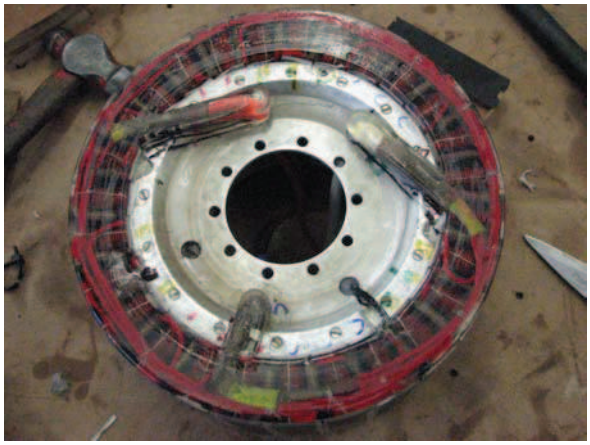

(e) Completely cured stator - front view

(f) Completely cured stator - side view

Figure 7.20: Stator winding epoxy process.

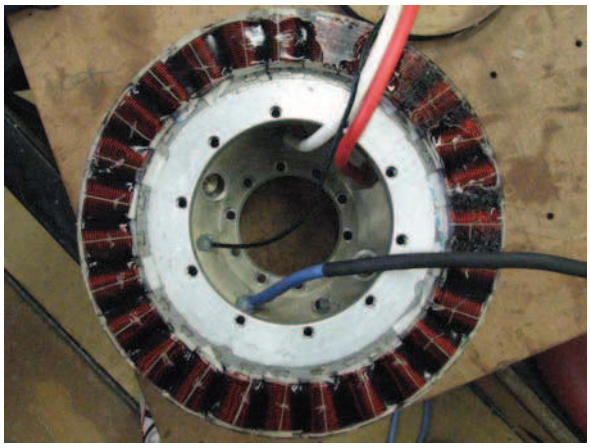

(a) Completely cured stator - bottom view

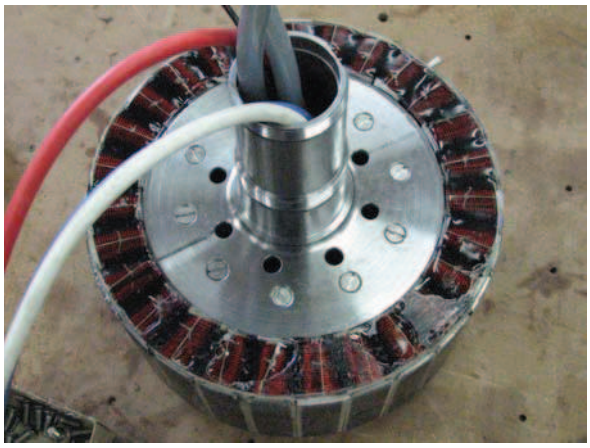

(b) Motor axle and cooling pipes installed

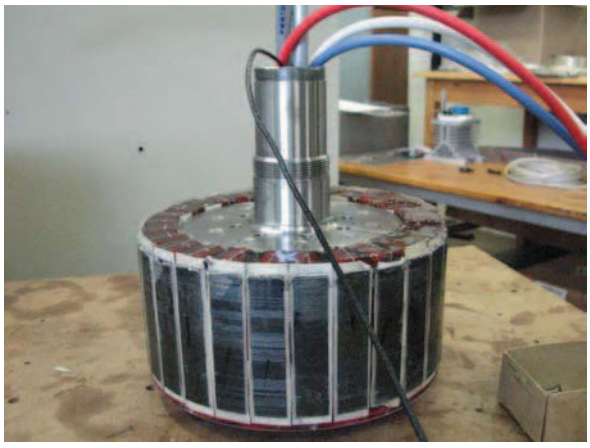

(c) Completed stator - side view

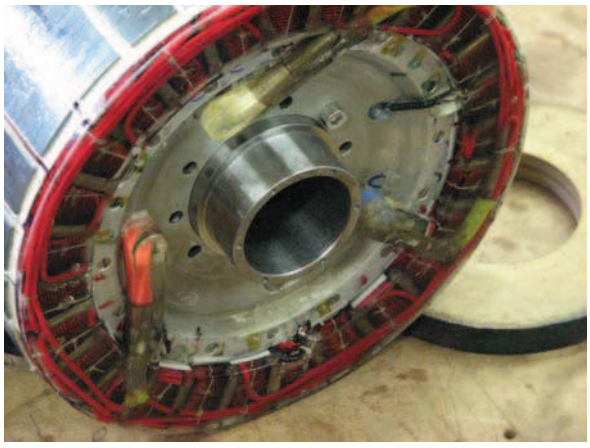

(d) Completed stator - front view

Figure 7.21: Completed stator.

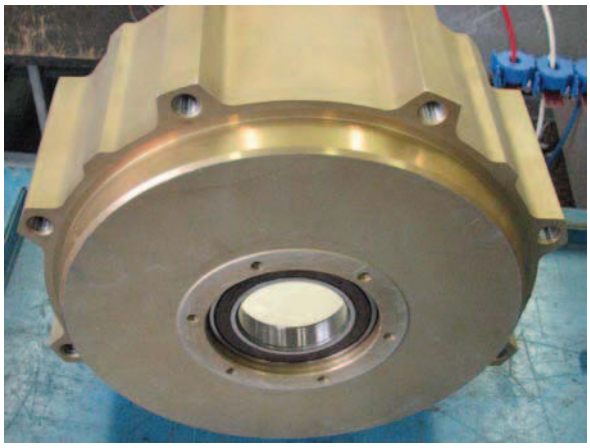

(a) Rotor outer shell

(b) Rotor lamination fitting

(c) Finished fitting the rotor laminations

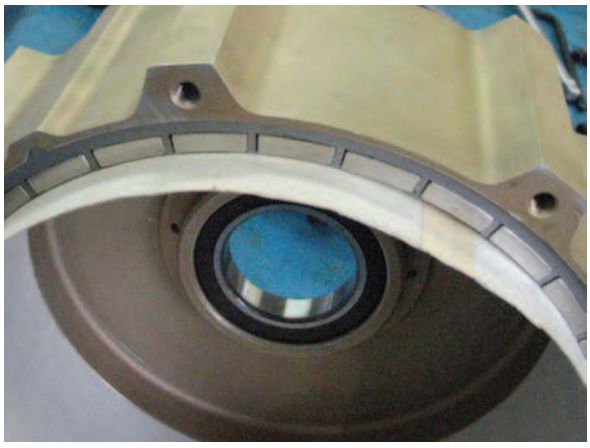

(d) Close-up of the magnets

Figure 7.22: Rotor assembly.

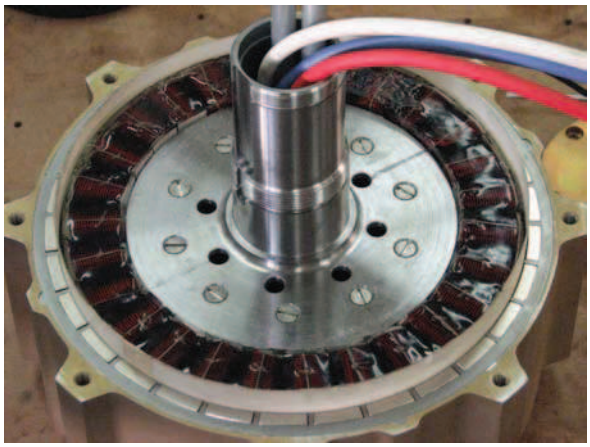

(a) Motor assembled without rear cover plate

(b) Resolver installed

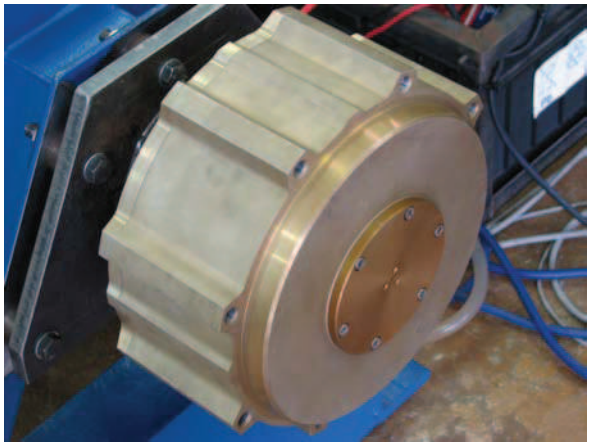

(c) Assembled motor - front view

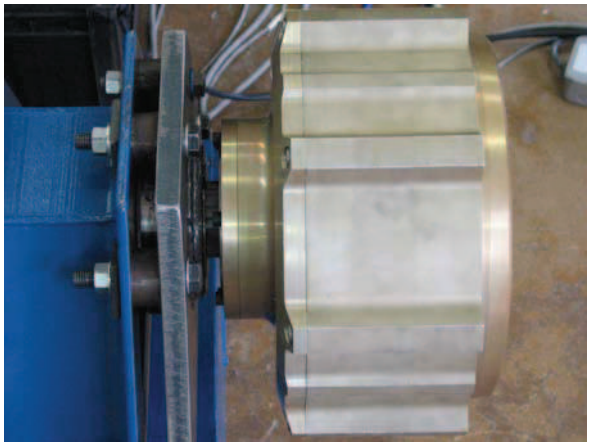

(d) Assembled motor - side view

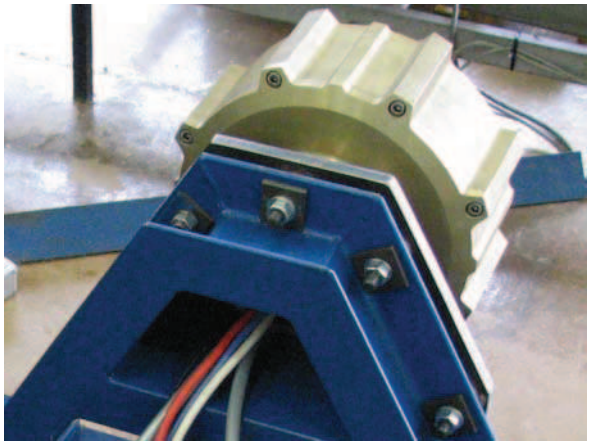

(e) Assembled motor - rear view

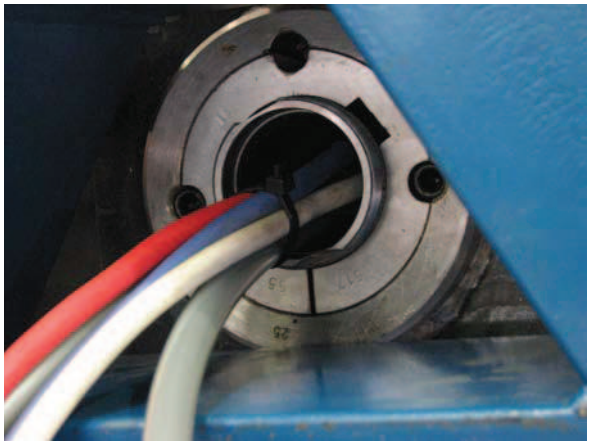

(f) Hollow axle with the cabling visible

Figure 7.23: Hub motor 2 assembled and ready for testing.

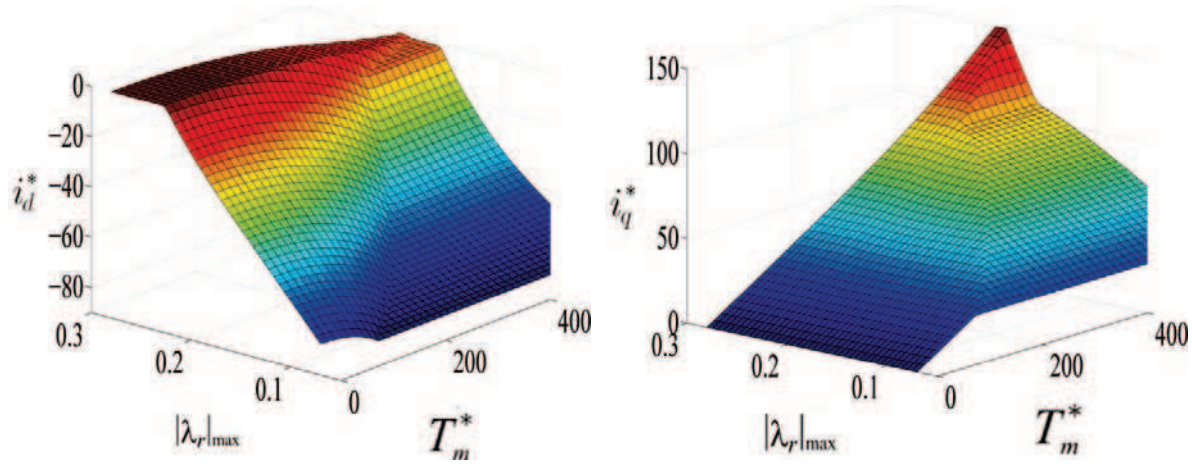

(a) HM2 i_d reference.

(b) HM2 i_q reference.

Figure 7.24: Torque control LUTs for hub motor 2.

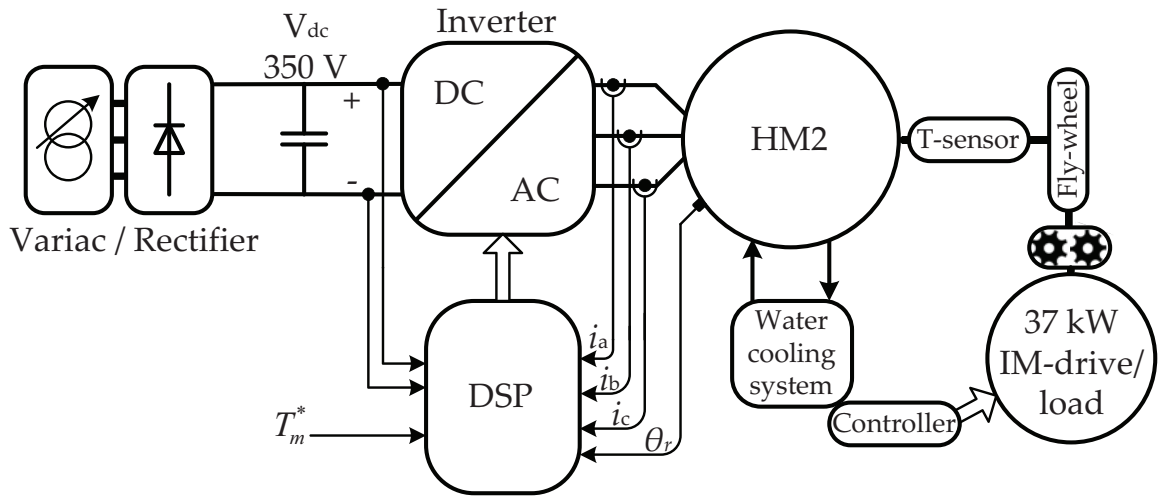

Figure 7.25: Test setup diagram for Hub motor 2.

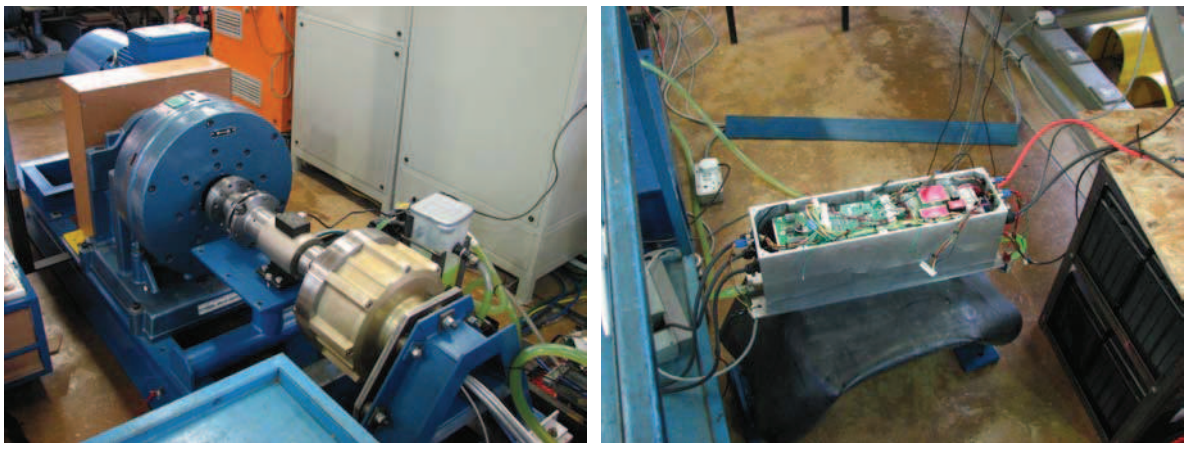

(a) Motor assembled and ready for testing

(b) Integrated DSP and Inverter

Figure 7.26: Hub motor 2 laboratory test setup.

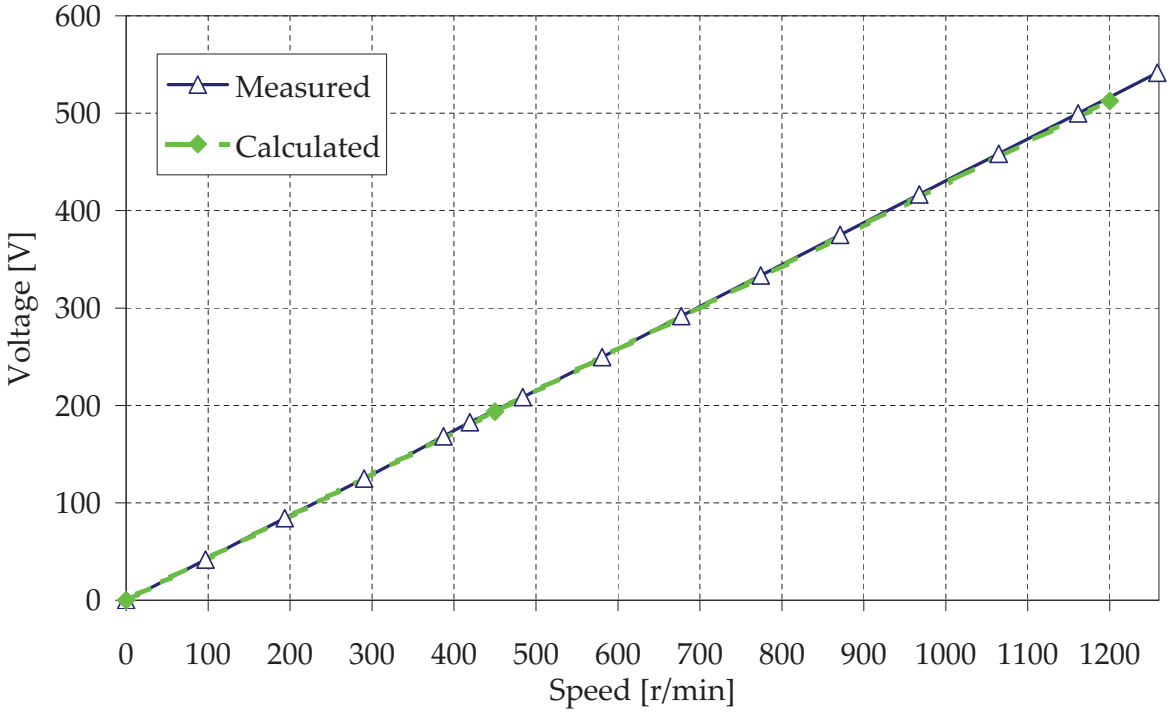

Figure 7.27: Measured open circuit voltage of hub motor 2.

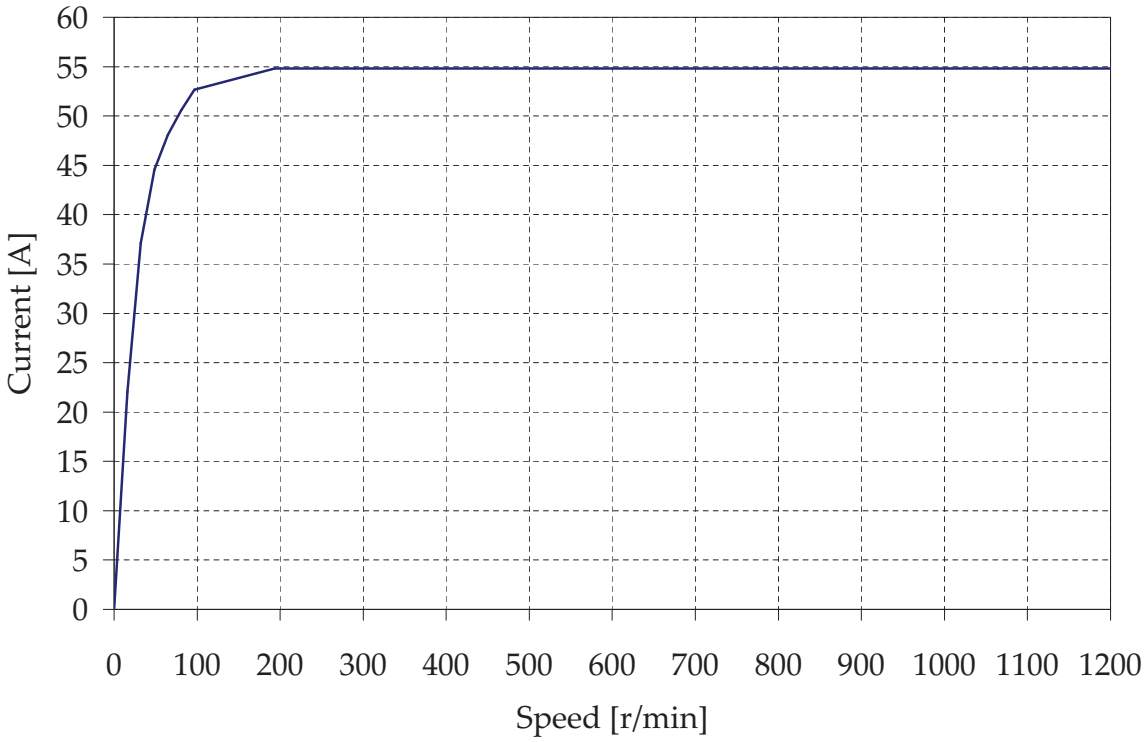

Figure 7.28: Measured current of HM2 when short circuited.

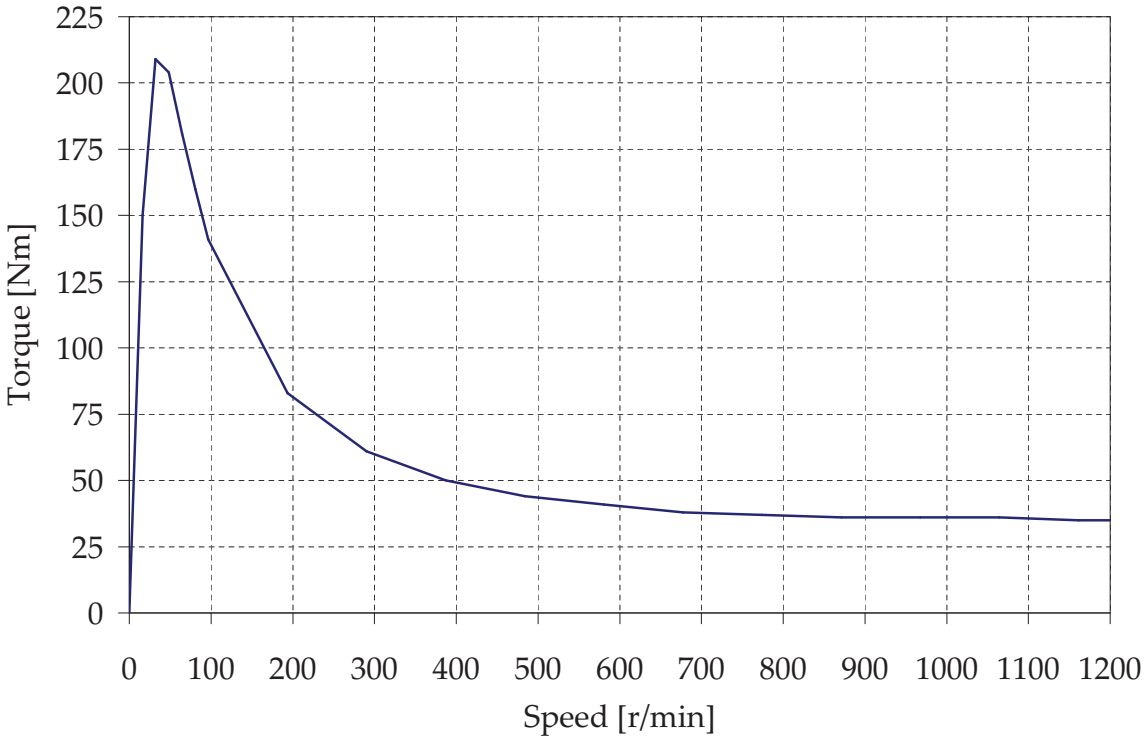

Figure 7.29: Measured torque of HM2 when short circuited (rated torque is 340 Nm).

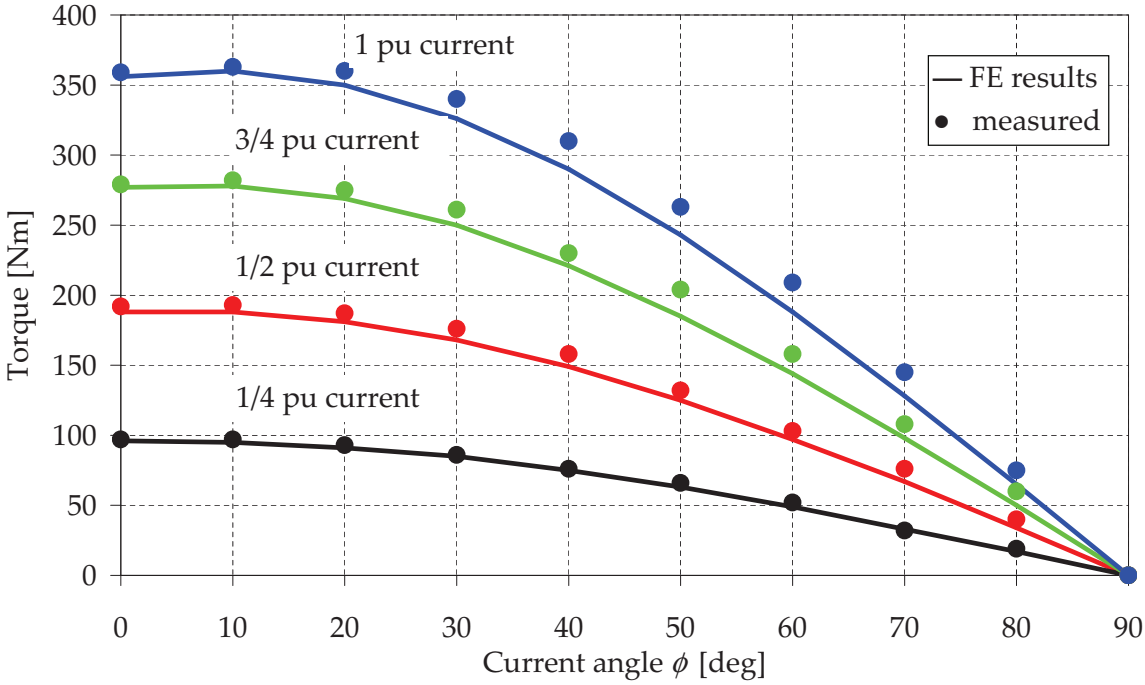

Figure 7.30: Measured and calculated torque vs. current angle of HM2.

CHAPTER 8

CONCLUSIONS AND RECOMMENDATIONS

The work presented in this dissertation is on the optimal design and control of radial flux PM machines with non-overlapping, concentrated-coils, for the use as hub drives in EVs.

In this chapter the aspects of the thesis which are considered to be original are highlighted. Attention is paid to some conclusions from the presented theory, machine design, machine control and manufacturing.

8.1 Harmonic analysis

A simple analytical method to predict (explain) the harmonic content of the MMF, originating from either the 3-phase stator windings or the surface mounted PMs on the rotor, is presented. As an expansion of this analytical method, it is applied to predict the harmonic content of the air gap permeance function. These methods are then further developed to predict the torque and torque ripple of a machine with large slot openings and surface mounted PMs. The analytical method can also be used in a first basic design, to investigate pole-slot combinations and to optimize machine parameters such as the tooth and magnet pitch, before using a more accurate FEA design tool.

8.2 Frequency losses

A different approach to calculate iron, eddy current and magnet losses is presented in this thesis. Instead of using direct FEA or analytical methods based on the flux density variation in the air gap, flux density variation data are extracted from a series of static FE solutions and combined with empirical loss calculations. The flux density is extracted through the machine model, which is advantageous specifically when the machine is under field weakening control and the flux paths change from normal operating conditions.

This method of loss calculation is not verified by either FEA or measurement. Although the correctness of this method is not confirmed, it is used for design comparison purposes, hence errors would be present in all the models. This method combined with a non-commercial FEA

package's static solution, is fast and it is expected to result in very competitive optimization computation times.

8.3 Optimal machine design

Different topologies for radial flux PM machines with non-overlapping concentrated coils are optimized and compared. It is confirmed that the rotor topology has the biggest influence on the CPSR, and that the stator slot shape has little impact on the average torque of the machine while greatly influencing the torque ripple.

It is shown that the torque per I^2R copper loss performance of concentrated-coil PM machines cannot solely be judged on the stator coil winding factor. The torque per active mass is also found to be the same for machines with open slot and semi-closed slot stators.

There is a tendency that machines with open slots have higher iron, magnet and stator eddy current losses than machines with semi-closed stator slots. From the modelled machines it is found that machines with good winding factors, typically have more than 20% lower losses and about 2% higher efficiency than machines with low winding factors.

An important general finding here is that open stator slot machines with rectangular preformed coils, and thus low manufacturing costs, perform better than what was expected based on the winding factors, and are certainly an option for the use as hub drives.

8.4 Optimal machine control

A torque control algorithm for PMSM drives, that works in the entire speed range and for a variable DC bus voltage, is proposed and demonstrated. The suggested torque control algorithm is based on a set of 2D LUTs that is automatically generated from FEA results. There are no approximations, with the correct current vector reference given in an instant by the DSP without any iteritive computations. This control algorithm can easily be implemented and should therefore be attractive for industrial drive applications.

8.5 Prototype construction and testing

The manufacturing and testing of two different radial flux PM hub drives are described and shown in detail in this thesis. This can be considered as a contribution to the engineering industry, as manufacturing and performance information on practical hub drives is lacking in the literature. The first hub motor has a low winding factor compared to the high winding factor of the second hub motor. Furthermore the stator designs varied from an open slot design,

using rectangular preformed coils, to a semi-closed slot design. The semi-closed slot design is adapted in a way that allows the use of preformed coils, a method that is demonstrated in this thesis to be viable. This method includes the fitting of a coil to a loose laminated tooth, and then the fitting of the tooth to the stator back yoke. This way of manufacturing reduces the cost of manufacturing the stator coils, and produces a machine with desirable attributes.

8.6 Recommendations

From the calculated and measured results in this thesis on PM hub drives the following recommendations are made for further study and investigation:

- The harmonic analysis tool presented in this thesis should be expanded to include machines with PM rotor designs other than those considered, namely surface mounted PM motors. Specifically PM rotors with embedded and interior PMs should be included in this work.
- The iron loss, magnet loss and eddy current loss calculation methods need to be compared with FEA and measured data to determine the correctness (or not) of the method.

Appendices

APPENDIX A

INDUCED VOLTAGES

This Appendix gives further derivation of the theory in Chapter 2.

A.1 Magnet coil voltage induced by the stator MMF

The flux density due to the stator MMF induces a voltage in the fictitious magnets coils. The calculation of the magnet coil induced voltage is shown in this section.

The magnet coil flux linkage can be derived from (2.38) as

$$\lambda_{rn} = \int_{-\theta_m/2}^{\theta_m/2} b_{rn} l r_g \frac{d\theta}{M_s} \tag{A.1}$$

$$= \int_{-\theta_m/2}^{\theta_m/2} B_{rn} \sin(\omega_{rn} t + n_s\theta) l \frac{d_g}{2M_s} d\theta \tag{A.2}$$

$$= \frac{B_{rn} l d_g}{2M_s} \int_{-\theta_m/2}^{\theta_m/2} \sin(\omega_{rn} t + n_s\theta) d\theta \tag{A.3}$$

$$= \frac{B_{rn} l d_g}{2M_s} \frac{-1}{n_s} \cos(\omega_{rn} t + n_s\theta) \Big|_{-\theta_m/2}^{\theta_m/2} \tag{A.4}$$

$$= \frac{B_{rn} l d_g}{2M_s} \frac{-2}{n_s} \sin\left(\frac{n_s\theta_m}{2}\right) \sin(\omega_{rn} t) \tag{A.5}$$

$$= \frac{-B_{rn} l d_g}{M_s n_s} k_{pmn} \sin(\omega_{rn} t), \tag{A.6}$$

with

$$k_{pmn} = \sin\left(\frac{n_s\theta_m}{2}\right). \tag{A.7}$$

The voltage in a single magnet coil is then given by

$$e_{mn} = \frac{-B_{rn} l d_g}{M_s n_s} k_{pmn} \omega_{rn} \cos(\omega_{rn} t), \tag{A.8}$$

and B_{rn} of (2.40) substituted, the voltage is

$$e_{mn} = \frac{-3\tau u N I \mu_0 l d_g}{\pi n_s^2 M_s g k_c} k_{wsn} k_{pmn} \omega_{rn} \cos(\omega_{rn} t). \tag{A.9}$$

With p magnets in a machine section; δ_{nr}, the n_s^{th} order phase displaced electrical angle between the n_s^{th} order magnet coil voltage phasors in a phase group, is given by

$$\delta_{nr} = \frac{2\pi|n_s|}{p} + \pi. \tag{A.10}$$

The amplitude of the n_s^{th} order induced magnet coil voltage of all the coils in series in a machine section is then given by

$$E_{mn} = \frac{3\tau u \mu_0 p l d_g N I}{\pi n_s^2 M_s g k_c} k_{wsn} k_{pmn} k_{dmn} |\omega_{rn}| \, . \tag{A.11}$$

A.2 Stator winding induced voltage

The flux density due to the rotor MMF induces a voltage in the stator windings. The calculation of the induced stator winding voltage is shown in this section.

The stator coil flux linkage can be derived from (2.49) as

$$\lambda_{sn} = N \int_{-\theta_s/2}^{\theta_s/2} b_{sn} l d_g \frac{d\theta}{M_s} \tag{A.12}$$

$$= N \int_{-\theta_s/2}^{\theta_s/2} B_{sn} \cos\left(\frac{2n_r\omega t}{p} + n_r\theta\right) \frac{l d_g}{M_s} d\theta \tag{A.13}$$

$$= \frac{N l d_g B_{sn}}{M_s} \int_{-\theta_s/2}^{\theta_s/2} \cos\left(\frac{2n_r\omega t}{p} + n_r\theta\right) d\theta \tag{A.14}$$

$$= \frac{N l d_g B_{sn}}{n_r M_s} \sin\left(\frac{2n_r\omega t}{p} + n_r\theta\right)\Bigg|_{-\theta_s/2}^{\theta_s/2} \tag{A.15}$$

$$= \frac{2N l d_g B_{sn}}{n_r M_s} k_{psn} \cos\left(\frac{2n_r\omega t}{p M_s}\right), \tag{A.16}$$

where the slot pitch factor, k_{psn}, is given by

$$k_{psn} = \sin\left(\frac{n_r\theta_s}{2}\right). \tag{A.17}$$

The induced phase voltage of the machine is then

$$e_{sn} = u k_{dsn} M_s \frac{d\lambda_{sn}}{dt} \tag{A.18}$$

$$= E_{sn} \sin\left(\frac{2n_r\omega t}{p M_s}\right), \tag{A.19}$$

with the amplitude E_{sn} of the induced phase voltage given by

$$E_{sn} = -k_{dsn} k_{psn} \frac{16 u \omega N l d_g B_{sn}}{p M_s}. \tag{A.20}$$

A.3 Magnet coil voltage induced by the stator slots

The stator slots cause a variation in the air gap permeance function. The variation in permeance results in a variation of flux density due to the rotor MMF and induce a voltage in the magnet coils. The calculation of the induced magnet coil voltage is shown in this section.

The flux linkage of a magnet coil can be expressed from (2.67) as

$$\lambda_{rn} = \int_{-\theta_m/2}^{\theta_m/2} B_g^*(t,\theta) l r_g \frac{d\theta}{pM_s} \tag{A.21}$$

$$= \frac{4pI_m\Delta S}{\pi^2} \int_{-\theta_m/2}^{\theta_m/2} \left[\sum_{n_r} \frac{k_{wmn_r}}{n_r} \cos(n_r\theta) \sum_{n_t} \frac{k_{ptn_t}}{n_t} \cos\left(\frac{2n_t\omega t}{pM_s} + n_t\theta\right) \right] l r_g \frac{d\theta}{pM_s} \tag{A.22}$$

$$= \frac{4I_m\Delta S l r_g}{\pi^2 M_s} \sum_{n_r} \frac{k_{wmn_r}}{n_r} \sum_{n_t} \frac{k_{ptn_t}}{n_t} \int_{-\theta_m/2}^{\theta_m/2} \left[\cos(n_r\theta) \cos\left(\frac{2n_t\omega t}{pM_s} + n_t\theta\right) \right] d\theta \tag{A.23}$$

$$= \frac{2I_m\Delta S l d_g}{\pi^2 M_s} \sum_{n_r} \frac{k_{wmn_r}}{n_r} \sum_{n_t} \frac{k_{ptn_t}}{n_t} \int_{-\theta_m/2}^{\theta_m/2} \left[\cos(n_r\theta) \cos\left(\frac{2n_t\omega t}{pM_s} + n_t\theta\right) \right] d\theta \tag{A.24}$$

$$= \frac{2I_m\Delta S l d_g}{\pi^2 M_s} \sum_{n_r} \frac{k_{wmn_r}}{n_r} \sum_{n_t} \frac{k_{ptn_t}}{n_t} \left[\frac{1}{n_r + n_t} \cos\left(\frac{2n_t\omega t}{pM_s} + (n_r + n_t)\theta\right) - \frac{1}{n_r - n_t} \cos\left(\frac{2n_t\omega t}{pM_s} - (n_r - n_t)\theta\right) \right] \Bigg|_{-\theta_m/2}^{\theta_m/2} \tag{A.25}$$

The voltage in a single magnet coil due to the movement of the stator slots relative to the magnets is then given by

$$e_{mn} = \frac{d\lambda_{rn}}{dt}$$

$$= \frac{-4I_m\Delta S l d_g \omega}{p\pi^2 M_s^2} \sum_{n_r} \frac{k_{wmn_r}}{n_r} \sum_{n_t} k_{ptn_t} \left[\left(\frac{1}{n_r + n_t}\right) \sin\left(\frac{(n_r + n_t)\theta_m}{2}\right) + \left(\frac{1}{n_r - n_t}\right) \sin\left(\frac{(n_r - n_t)\theta_m}{2}\right) \right] \sin\left(\frac{2n_t\omega t}{pM_s}\right) \tag{A.26}$$

Similar to (A.11) the amplitude of the n^{th} order induced magnet coil voltage of all the coils, in series, in a machine section is then given by

$$E_{mn} = \frac{4I_m\Delta S l d_g \omega}{\pi^2 M_s^2} \sum_{n_r} \frac{k_{wmn_r}}{n_r} \sum_{n_t} k_{ptn_t} \left[\left(\frac{1}{n_r + n_t}\right) \sin\left(\frac{(n_r + n_t)\theta_m}{2}\right) + \left(\frac{1}{n_r - n_t}\right) \sin\left(\frac{(n_r - n_t)\theta_m}{2}\right) \right]$$

$$\text{for } n_t \in \text{LCM}(p, n_t) \tag{A.27}$$

APPENDIX B

VEHICLE MODELING

B.1 EV performance

The required vehicle performance is used to derive the specifications for the electrical motor that will serve as the main drive for the EV. The vehicle specifications are given in Table B.1

Table B.1: Vehicle Specifications.

Mass	1500 kg	
Drive	All wheel drive	
Tires	195/50R15	
Max Speed	130 km/h	
Hill Climb	19%	0-20 km/h
	11%	20-40 km/h
	8%	40-80 km/h
	5.5%	80-110 km/h
	3%	110-130 km/h

B.1.1 EV modeling

For all EVs the prediction of the performance is of great importance. Computer simulations point out the influence that changes of a certain parameter have on the performance of the total EV drive system [74]. The performance of EVs can be classified by two parameters namely (i) the acceleration and (ii) the top speed of the EV. It is very important that any EV should have the necessary performance to allow it to blend safely with city traffic.

B.1.1.1 Tractive effort

Tractive effort is the force propelling the vehicle forward. This force is transmitted to the ground through the drive wheels. Consider the forces acting on a vehicle of mass m, proceeding at a velocity v, up a slope of angle ψ, as shown in Fig. B.1

The tractive effort, F_{te} has to accomplish the following:

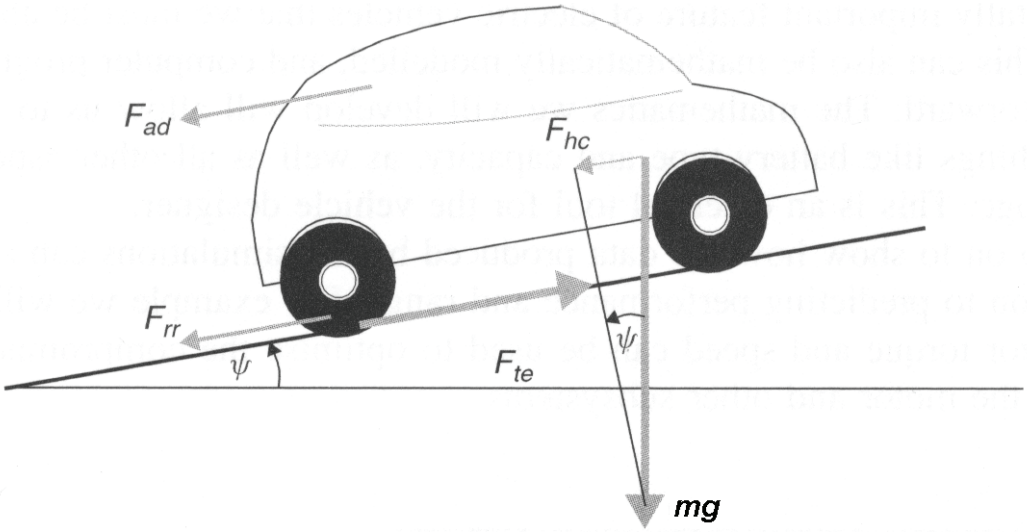

Figure B.1: Forces acting on a vehicle moving along a slope

- Overcome the rolling resistance;
- Overcome the aerodynamic drag;
- Provide the force needed to overcome the vehicle's weight component;
- Accelerate the vehicle.

To calculate the tractive effort required to accelerate the EV all the forces acting on the electric vehicle need to be calculated. These calculations will be discussed in the following sections.

B.1.1.2 Rolling resistance force

The friction between the vehicle tyre and the road causes a rolling resistance. A contributing factor is friction in the bearings and the transmission. The rolling resistance is approximately constant and depends only slightly on the vehicle speed. The rolling resistance is calculated by

$$F_{rr} = \mu_{rr} mg, \tag{B.1}$$

where μ_{rr} is the rolling resistance coefficient and g is the gravitational constant. The influencing factors effecting μ_{rr} are the tyre type and the tyre pressure.

B.1.1.3 Aerodynamic drag

The friction of the vehicle body moving through air causes aerodynamic drag. Aerodynamic drag is a function of the frontal area and the shape of the vehicle. This force component is

calculated by

$$F_{ad} = \frac{1}{2}\rho A C_d v^2, \tag{B.2}$$

where ρ is the density of air, A is the frontal area and v is the velocity. C_d is a constant called the drag coefficient.

B.1.1.4 Hill climbing force

The hill climbing force is the force needed to drive a vehicle up a slope. This is simply the component of the vehicle's weight acting along the slope as can be seen in Fig. B.1. The hill climbing force is calculated by

$$F_{hc} = mg\sin(\psi). \tag{B.3}$$

B.1.1.5 Acceleration force

Changing the speed of a vehicle requires a force to provide linear acceleration. From Newton's second law we find that this force is calculated by

$$F_{la} = ma. \tag{B.4}$$

There is another force that is required to make rotating objects turn faster; this is known as rotational acceleration expressed by

$$F_{wa} = I\frac{G^2}{\eta_g r^2}a. \tag{B.5}$$

Equation (B.5) is used to calculate the acceleration force F_{wa}. I is the moment of inertia of the motor's rotor, η_g is the gear system efficiency, G is the gear ratio of the system connecting the motor to the axle, and r is the tyre radius. For direct drive applications such hub drives for EVs, the gear ratio G is equal to one.

B.1.1.6 Total tractive effort

The total tractive effort is the combination of all the above forces as shown in Fig. B.1:

$$F_{te} = F_{rr} + F_{ad} + F_{hc} + F_{la} + F_{wa}. \tag{B.6}$$

F_{la} and F_{wa} are negative if the vehicle is slowing down, and F_{hc} is negative if it is going downhill.

B.1.1.7 Modelling vehicle acceleration

The acceleration of a car is one of the key performance indicators, though there is no standard measure used to indicate the performance. Typically the time to accelerate from standstill to 100 km/h of the vehicle is specified.

For a vehicle on level ground, with an air density 1.25 $kg.m^{-3}$, the total tractive effort becomes

$$F_{te} = \mu_{rr} + 0.625AC_d v^2 + ma + I\frac{G^2}{\eta_g r^2}a, \tag{B.7}$$

noting that

$$F_{te} = \frac{G}{r}T \qquad \text{and} \qquad a = \frac{dv}{dt}$$
$$\frac{G}{r}T = \mu_{rr} + 0.625AC_d v^2 + ma + \left(m + I\frac{G^2}{\eta_g r^2}\right)\frac{dv}{dt}. \tag{B.8}$$

This equation can be reduced to a first order differential equation to solve for the velocity v. Thus v can be found for any value of time, t, used.

B.1.1.8 Required torque and power calculations

The drive requirements per wheel can be obtained by using a quarter of the total vehicle requirements, assuming an all-wheel-drive vehicle. The car parameters used in all the calculations are given in Table B.2.

The torque required is calculated for vehicle speeds of 0-160 km/h and different slope inclines. Using the parameters given in Table B.2, the torque is calculated from (B.8) and is shown in Fig. B.2.

The power that is required for this vehicle is derived from the torque using (B.9), and is shown in Fig. B.3.

$$P = \omega T \tag{B.9}$$

where ω is the angular speed of the vehicle's wheels.

Table B.2: Vehicle parameters

Tyre Radius	0.3 m
Gear Ratio	1
Rolling Resistance Coefficient	0.0075
Total Mass	1500 kg
Frontal Area	1.8 m^2
Drag Coefficient	0.3
Air Density	1.25 $kg.m^{-3}$

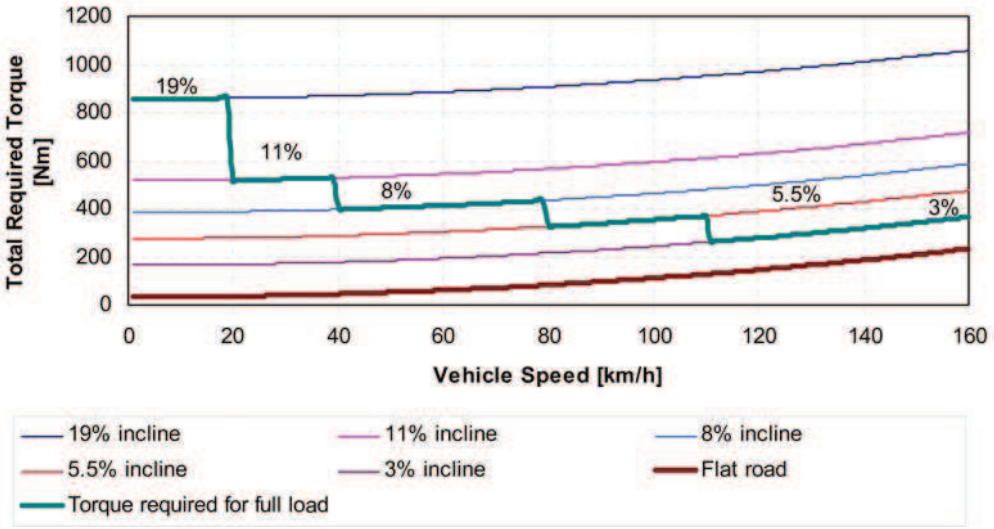

Figure B.2: Torque required to maintain a certain speed.

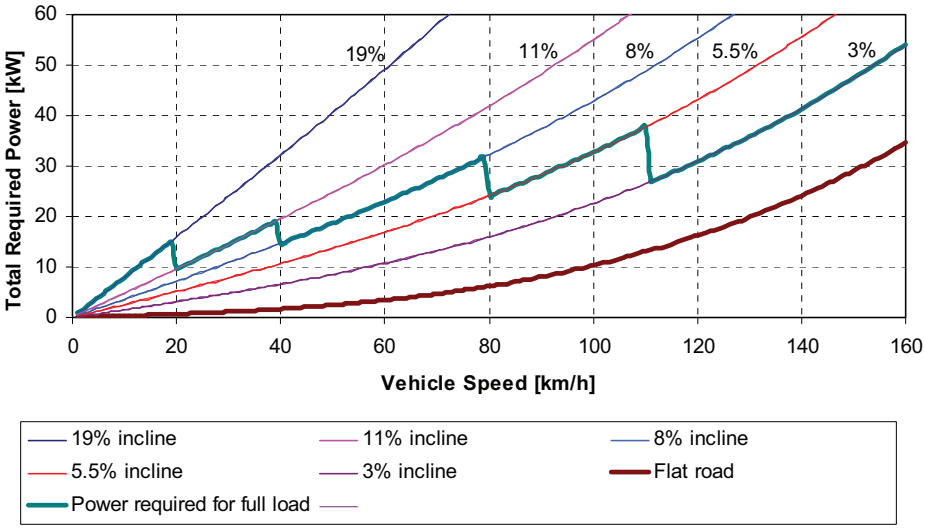

Figure B.3: Power required to maintain a certain speed.

APPENDIX C

VALUES FOR K AND k OF CHAPTER 3

This Appendix gives the tables with values of K and k used in Chapter 3, specifically in equation (3.16).

Table C.1: Values of K for short single-layer coils.

b/2a	K	b/2a	K	b/2a	K	b/2a	K
0.00	0.000000	0.25	0.365432	0.50	0.525510	0.75	0.623011
0.01	0.034960	0.26	0.373818	0.51	0.530310	0.76	0.626122
0.02	0.061098	0.27	0.381986	0.52	0.535018	0.77	0.629185
0.03	0.083907	0.28	0.389944	0.53	0.539637	0.78	0.632200
0.04	0.104562	0.29	0.397703	0.54	0.544170	0.79	0.635170
0.05	0.123615	0.30	0.405269	0.55	0.548620	0.80	0.638094
0.06	0.141395	0.31	0.412650	0.56	0.552988	0.81	0.640974
0.07	0.158119	0.32	0.419856	0.57	0.557278	0.82	0.643811
0.08	0.173942	0.33	0.426890	0.58	0.561491	0.83	0.646605
0.09	0.188980	0.34	0.433762	0.59	0.565628	0.84	0.649358
0.10	0.203324	0.35	0.440474	0.60	0.569691	0.85	0.652070
0.11	0.217044	0.36	0.447036	0.61	0.573683	0.86	0.654743
0.12	0.230200	0.37	0.453450	0.62	0.577606	0.87	0.657376
0.13	0.242842	0.38	0.459724	0.63	0.581462	0.88	0.659972
0.14	0.255011	0.39	0.465860	0.64	0.585252	0.89	0.662532
0.15	0.266744	0.40	0.471865	0.65	0.588976	0.90	0.665054
0.16	0.278070	0.41	0.477742	0.66	0.592638	0.91	0.667540
0.17	0.289019	0.42	0.483496	0.67	0.596239	0.92	0.669991
0.18	0.299614	0.43	0.489129	0.68	0.599780	0.93	0.672408
0.19	0.309876	0.44	0.494646	0.69	0.603263	0.94	0.674792
0.20	0.319825	0.45	0.500052	0.70	0.606689	0.95	0.677142
0.21	0.329479	0.46	0.505348	0.71	0.610060	0.96	0.679460
0.22	0.338852	0.47	0.510539	0.72	0.613376	0.97	0.681747
0.23	0.347960	0.48	0.515628	0.73	0.616639	0.98	0.684003
0.24	0.356816	0.49	0.520617	0.74	0.619850	0.99	0.686228
0.25	0.365432	0.50	0.525510	0.75	0.623011	1.00	0.688423

Table C.2: Values of *k* for thin, long coils.

c/b	c/2a											c/b
	0.00	0.05	0.10	0.15	0.20	0.25	0.30	0.35	0.40	0.45	0.50	
0.00	0.0000	0.0325	0.0633	0.0925	0.1200	0.1458	0.1700	0.1925	0.2133	0.2325	0.2500	0.00
0.05	0.0000	0.0316	0.0633	0.0911	0.1186	0.1445	0.1687	0.1913	0.2123	0.2317	0.2494	0.05
0.10	0.0000	0.0308	0.0621	0.0896	0.1170	0.1428	0.1671	0.1898	0.2109	0.2304	0.2484	0.10
0.15	0.0000	0.0300	0.0608	0.0879	0.1151	0.1409	0.1651	0.1879	0.2091	0.2288	0.2470	0.15
0.20	0.0000	0.0293	0.0594	0.0861	0.1131	0.1388	0.1630	0.1858	0.2071	0.2270	0.2453	0.20
0.25	0.0000	0.0286	0.0581	0.0843	0.1109	0.1365	0.1607	0.1835	0.2048	0.2248	0.2432	0.25
0.30	0.0000	0.0280	0.0569	0.0826	0.1085	0.1342	0.1583	0.1810	0.2024	0.2224	0.2410	0.30
0.35	0.0000	0.0274	0.0557	0.0810	0.1069	0.1319	0.1558	0.1785	0.1999	0.2199	0.2386	0.35
0.40	0.0000	0.0269	0.0546	0.0796	0.1051	0.1297	0.1533	0.1759	0.1973	0.2174	0.2361	0.40
0.45	0.0000	0.0264	0.0535	0.0782	0.1033	0.1276	0.1510	0.1732	0.1945	0.2146	0.2335	0.45
0.50	0.0000	0.0259	0.0525	0.0769	0.1016	0.1256	0.1487	0.1706	0.1916	0.2118	0.2308	0.50
0.55	0.0000	0.0254	0.0516	0.0755	0.0999	0.1236	0.1464	0.1682	0.1890	0.2091	0.2280	0.55
0.60	0.0000	0.0250	0.0507	0.0742	0.0982	0.1216	0.1442	0.1658	0.1866	0.2065	0.2252	0.60
0.65	0.0000	0.0246	0.0498	0.0730	0.0966	0.1197	0.1421	0.1635	0.1842	0.2039	0.2225	0.65
0.70	0.0000	0.0242	0.0490	0.0719	0.0952	0.1179	0.1400	0.1613	0.1818	0.2014	0.2199	0.70
0.75	0.0000	0.0238	0.0482	0.0708	0.0937	0.1161	0.1380	0.1591	0.1794	0.1988	0.2173	0.75
0.80	0.0000	0.0234	0.0474	0.0697	0.0923	0.1144	0.1360	0.1569	0.1770	0.1963	0.2147	0.80
0.85	0.0000	0.0230	0.0460	0.0687	0.0910	0.1128	0.1341	0.1548	0.1747	0.1939	0.2121	0.85
0.90	0.0000	0.0227	0.0453	0.0677	0.0897	0.1113	0.1323	0.1527	0.1725	0.1915	0.2096	0.90
0.95	0.0000	0.0224	0.0447	0.0667	0.0884	0.1097	0.1305	0.1507	0.1704	0.1892	0.2071	0.95
1.00	0.0000	0.0221	0.0441	0.0658	0.0872	0.1082	0.1288	0.1489	0.1683	0.1869	0.2047	1.00

Table C.3: Values of *k* for thin, long coils.

c/b	c/2a											c/b
	0.50	0.55	0.60	0.65	0.70	0.75	0.80	0.85	0.90	0.95	1.00	
0.00	0.2500	0.2658	0.2800	0.2925	0.3033	0.3125	0.3200	0.3258	0.3300	0.3325	0.3333	0.00
0.05	0.2494	0.2655	0.2800	0.2928	0.3040	0.3135	0.3213	0.3275	0.3321	0.3351	0.3363	0.05
0.10	0.2484	0.2648	0.2795	0.2926	0.3040	0.3138	0.3221	0.3287	0.3337	0.3371	0.3388	0.10
0.15	0.2470	0.2636	0.2786	0.2920	0.3037	0.3139	0.3225	0.3294	0.3349	0.3386	0.3408	0.15
0.20	0.2453	0.2621	0.2773	0.2910	0.3031	0.3136	0.3225	0.3298	0.3356	0.3397	0.3423	0.20
0.25	0.2432	0.2603	0.2758	0.2897	0.3021	0.3129	0.3221	0.3298	0.3359	0.3404	0.3434	0.25
0.30	0.2410	0.2582	0.2739	0.2881	0.3007	0.3118	0.3213	0.3294	0.3359	0.3408	0.3441	0.30
0.35	0.2386	0.2559	0.2718	0.2862	0.2991	0.3104	0.3202	0.3286	0.3355	0.3407	0.3445	0.35
0.40	0.2361	0.2535	0.2695	0.2841	0.2972	0.3088	0.3189	0.3276	0.3347	0.3403	0.3445	0.40
0.45	0.2335	0.2509	0.2671	0.2818	0.2951	0.3070	0.3173	0.3263	0.3337	0.3397	0.3442	0.45
0.50	0.2308	0.2483	0.2645	0.2794	0.2929	0.3050	0.3156	0.3248	0.3326	0.3389	0.3436	0.50
0.55	0.2280	0.2456	0.2619	0.2769	0.2906	0.3028	0.3137	0.3231	0.3311	0.3377	0.3428	0.55
0.60	0.2253	0.2428	0.2592	0.2743	0.2881	0.3005	0.3116	0.3213	0.3295	0.3363	0.3417	0.60
0.65	0.2225	0.2400	0.2564	0.2716	0.2856	0.2981	0.3093	0.3192	0.3277	0.3348	0.3404	0.65
0.70	0.2199	0.2373	0.2536	0.2689	0.2830	0.2957	0.3070	0.3171	0.3258	0.3331	0.3390	0.70
0.75	0.2173	0.2346	0.2509	0.2662	0.2804	0.2932	0.3046	0.3149	0.3238	0.3313	0.3375	0.75
0.80	0.2147	0.2320	0.2483	0.2636	0.2777	0.2906	0.3022	0.3126	0.3217	0.3294	0.3358	0.80
0.85	0.2121	0.2294	0.2456	0.2609	0.2750	0.2880	0.2998	0.3103	0.3195	0.3274	0.3340	0.85
0.90	0.2096	0.2268	0.2430	0.2582	0.2724	0.2855	0.2978	0.3079	0.3172	0.3253	0.3321	0.90
0.95	0.2071	0.2242	0.2404	0.2556	0.2698	0.2829	0.2949	0.3055	0.3149	0.3231	0.3301	0.95
1.00	0.2047	0.2217	0.2378	0.2530	0.2672	0.2804	0.2929	0.3031	0.3126	0.3209	0.3281	1.00

BIBLIOGRAPHY

[1] "Electric vehicle history," 2009, the Electric Auto Association. [Online]. Available: http://www.eaaev.org/History/index.html

[2] "History of electric vehicles 1834," 2006, max Energy Limited. [Online]. Available: http://www.speedace.info/electric_vehicle_history.htm

[3] "Electric vehicle," September 2010, wikipedia. [Online]. Available: http://en.wikipedia.org/wiki/Electric_vehicle

[4] J. Malan and M. Kamper, "Performance of a hybrid electric vehicle using reluctance synchronous machine technology," *Industry Applications, IEEE Transactions on*, vol. 37, no. 5, pp. 1319 – 1324, September 2001.

[5] W. Adams, "Electric motor," U.S. Patent 300,827, June 24, 1884.

[6] A. L. Parcelle, "Electro-motor traction-wheel," U.S. Patent 433,180, July 29, 1890.

[7] E. B. Parkhurst, "Electric motor," U.S. Patent 422,149, February 25, 1890.

[8] C. Theryc, "Wheel with electric motor hub for vehicles," French Patent 572,036, November 24, 1896.

[9] "Porsche history, milestones," 2010, porsche. [Online]. Available: http://www.porsche.com/usa/aboutporsche/porschehistory/milestones/

[10] J. Neff, "PML MINI QED boasts 640 in-wheel electric horsepower," October 2010. [Online]. Available: http://www.autoblog.com/2006/07/21/pml-s-mini-qed-boasts-640-in-wheel-electric-horsepower/

[11] "Peugeot-bb1," October 2010. [Online]. Available: http://www.bb1-peugeot.com/

[12] F. S. Van der Merwe, "The analysis of an electric machine with a smooth air-gap allowing for all winding MMF harmonics," Ph.D. dissertation, University of Stellenbosch, Stellenbosch, South Africa, 1975.

[13] F. Magnussen and C. Sadarangani, "Winding factors and joule losses of permanent magnet machines with concentrated windings," in *Electric Machines & Drives Conference (IEMDC '03), IEEE International*, vol. 1, Wisconsin, USA, June 2003, pp. 333 – 339.

[14] F. Libert and J. Soulard, "Investigation on pole-slot combinations for permanent-magnet machines with concentrated windings," in *Investigation on pole-slot combinations for permanent-magnet machines with concentrated windings*, Cracow, Poland, September 2004.

[15] S. Skaar, O. Krovel, and R. Nilsen, "Distribution, coil-span and winding factors for PM machines with concentrated windings," in *Electrical Machines (ICEM'06), 18th International Conference on*, Crete, Grece, September 2006.

[16] Z. Zhu, L. Wu, and Z. Xia, "An accurate subdomain model for magnetic field computation in slotted surface-mounted permanent-magnet machines," *Magnetics, IEEE Transactions on*, vol. 46, no. 4, pp. 1100 – 1115, April 2010.

[17] K. Boughrara, R. Ibtiouen, D. Z Andarko, O. Touhami, and A. Rezzoug, "Magnetic field analysis of external rotor permanent-magnet synchronous motors using conformal mapping," *Magnetics, IEEE Transactions on*, vol. 46, no. 9, pp. 3684 – 3693, September 2010.

[18] J. Zhang, M. Cheng, and W. Hua, "Calculation of cogging torque for stator interior permanent magnet machine," in *Electromagnetic Field Computation (CEFC'10), 14th Biennial IEEE Conference on*, Chicago, IL, May 2010, p. 1.

[19] L. Wu, Z. Zhu, D. Staton, M. Popescu, and D. Hawkins, "Combined complex permeance and sub-domain model for analytical predicting electromagnetic performance of surface-mounted PM machines," in *Power Electronics, Machines and Drives (PEMD'10), 5th IET International Conference on*, Brighton, UK, April 2010, pp. 1 –6.

[20] S. Ho, N. Chen, and W. Fu, "An optimal design method for the minimization of cogging torques of a permanent magnet motor using FEM and genetic algorithm," *Applied Superconductivity, IEEE Transactions on*, vol. 20, no. 3, pp. 861 –864, June 2010.

[21] W. Fei and P. Luk, "A new technique of cogging torque suppression in direct-drive permanent-magnet brushless machines," *Industry Applications, IEEE Transactions on*, vol. 46, no. 4, pp. 1332 –1340, July 2010.

[22] N. Chen, S. Ho, and W. Fu, "Optimization of permanent magnet surface shapes of electric motors for minimization of cogging torque using FEM," *Magnetics, IEEE Transactions on*, vol. 46, no. 6, pp. 2478 –2481, June 2010.

[23] T. Tudorache, L. Melcescu, and M. Popescu, "Methods for cogging torque reduction of directly driven PM wind generators," in *Optimization of Electrical and Electronic Equipment (OPTIM'10), 12th International Conference on*, Basov, Romania, May 2010, pp. 1161 –1166.

[24] C.-S. Liu, J.-C. Hwang, and C. Po-Cheng, "Design of permanent magnet synchronous motor with low cogging torque," in *Power Electronics Conference (IPEC '10), International*, Sapporo, Japan, June 2010, pp. 1083 –1087.

[25] N. Saito, R. Kijima, and S. Shimomura, "The design method to minimize torque ripple in interior permanent magnet synchronous motor with concentrated winding," in *Power Electronics Conference (IPEC'10), International*, Sapporo, Japan, June 2010, pp. 1293 – 1298.

[26] B. Stumberger, A. Hamler, and B. Hribernik, "Analysis of iron loss in interior permanent magnet synchronous motor over a wide-speed range of constant output power operation," *Magnetics, IEEE Transactions on*, vol. 36, no. 4, pp. 1846 – 1849, July 2000.

[27] H. Polinder and M. Hoeijmakers, "Eddy-current losses in the segmented surface-mounted magnets of a PM machine," *Electric Power Applications, IEE Proceedings*, vol. 146, no. 3, pp. 261 –266, May 1999.

[28] F. Deng, "An improved iron loss estimation for permanent magnet brushless machines," *Energy Conversion, IEEE Transactions on*, vol. 14, no. 4, pp. 1391 – 1395, December 1999.

[29] Y. Chin and J. Soulard, "Modeling of iron losses in permanent magnet synchronous motors with field weakening capability for electric vehicles," *International Journal of Automotive Technology*, vol. 4, no. 2, pp. 87 – 94, March 2003.

[30] D. Ionel, M. Popescu, M. McGilp, T. Miller, S. Dellinger, and R. Heideman, "Computation of core losses in electrical machines using improved models for laminated steel," *Industry Applications, IEEE Transactions on*, vol. 43, no. 6, pp. 1554 – 1564, November 2007.

[31] K. Atallah, D. Howe, P. Mellor, and D. Stone, "Rotor loss in permanent-magnet brushless AC machines," *Industry Applications, IEEE Transactions on*, vol. 36, no. 6, pp. 1612 – 1618, November 2000.

[32] K. Tseng and S. Wee, "Analysis of flux distribution and core losses in interior permanent magnet motor," *Energy Conversion, IEEE Transactions on*, vol. 14, no. 4, pp. 969 – 975, December 1999.

[33] M. Nakano, H. Kometani, and M. Kawamura, "A study on eddy-current losses in rotors of surface permanent-magnet synchronous machines," *Industry Applications, IEEE Transactions on*, vol. 42, no. 2, pp. 429 – 435, March 2006.

[34] I. Mayergoyz, "On rotational eddy current losses in steel laminations," *Magnetics, IEEE Transactions on*, vol. 34, no. 4, pp. 1228 – 1230, July 1998.

[35] Z. Zhu, Y. Chen, and D. Howe, "Iron loss in permanent-magnet brushless AC machines under maximum torque per ampere and flux weakening control," *Magnetics, IEEE Transactions on*, vol. 38, no. 5, pp. 3285 – 3287, September 2002.

[36] N. Bianchi, S. Bolognani, and E. Fornasiero, "A general approach to determine the rotor losses in three-phase fractional-slot PM machines," in *Electric Machines & Drives Conference (IEMDC '07), IEEE International*, vol. 1, Antalya, Turkey, May 2007, pp. 634 – 641.

[37] J. Lavers, P. Biringer, and H. Hollitscher, "Estimation of core losses when the flux waveform contains the fundamental plus a single odd harmonic component," *Magnetics, IEEE Transactions on*, vol. 13, no. 5, pp. 1128 – 1130, September 1977.

[38] ——, "A simple method of estimating the minor loop hysteresis loss in thin laminations," *Magnetics, IEEE Transactions on*, vol. 14, no. 5, pp. 386 – 388, September 1978.

[39] J. Lavers and P. Biringer, "Prediction of core losses for high flux densities and distorted flux waveforms," *Magnetics, IEEE Transactions on*, vol. 12, no. 6, pp. 1053 – 1055, November 1976.

[40] D. Patterson and R. Spee, "The design and development of an axial flux permanent magnet brushless DC motor for wheel drive in a solar powered vehicle," *Industry Applications, IEEE Transactions on*, vol. 31, no. 5, pp. 1054 – 1061, September 1995.

[41] P. Anpalahan and M. Lamperth, "Design of multi-stack axial flux permanent magnet generator for a hybrid electric vehicle," in *Vehicle Power and Propulsion Conference (VPPC '06), IEEE*, Windsor, UK, September 2006, pp. 1 – 4.

[42] M. Lamperth, A. Beaudet, and M. Jaensch, "Disc motors for automotive applications," in *Hybrid and Eco-Friendly Vehicle Conference (HEVC '08), IET*, Coventry, UK, December 2008, pp. 1 – 5.

[43] D. Patterson, "Contemporary finite element analysis techniques for permanent magnet brushless DC machines, with application to axial flux traction systems for electric vehicles," in *Power Electronic Drives and Energy Systems for Industrial Growth, International Conference on*, vol. 2, Perth, Australia, December 1998, pp. 880 – 885.

[44] C. Versele, Z. De Greve, F. Vallee, R. Hanuise, O. Deblecker, M. Delhaye, and J. Lobry, "Analytical design of an axial flux permanent magnet in-wheel synchronous motor for electric vehicle," in *Power Electronics and Applications (EPE '09), 13th European Conference on*, Barcelona, Spain, Septmeber 2009, pp. 1 – 9.

[45] N. Rahim, H. W. Ping, and M. Tadjuddin, "Design of an in-wheel axial flux brushless DC motor for electric vehicle," in *Strategic Technology, The 1st International Forum on*, Ulsan, South Korea, October 2006, pp. 16 –19.

[46] T. Chan, L.-T. Yan, and S.-Y. Fang, "In-wheel permanent-magnet brushless DC motor drive for an electric bicycle," *Energy Conversion, IEEE Transactions on*, vol. 17, no. 2, pp. 229 – 233, June 2002.

[47] H. Lovatt, V. Ramsden, and B. Mecrow, "Design of an in-wheel motor for a solar-powered electric vehicle," *Electric Power Applications, IEE Proceedings*, vol. 145, no. 5, pp. 402 – 408, September 1998.

[48] F. Caricchi, F. Capponi, F. Crescimbini, and L. Solero, "Experimental study on reducing cogging torque and no-load power loss in axial-flux permanent-magnet machines with slotted winding," *Industry Applications, IEEE Transactions on*, vol. 40, no. 4, pp. 1066 – 1075, July 2004.

[49] W. Fu and S. Ho, "A novel axial-flux electric machine for in-wheel gearless drive in plug-in hybrid electric vehicles," in *Electromagnetic Field Computation (CEFC'10), 14th Biennial IEEE Conference on*, Chicago, IL, May 2010, pp. 1 –1.

[50] S. Wu, L. Song, and S. Cui, "Study on improving the performance of permanent magnet wheel motor for the electric vehicle application," *Magnetics, IEEE Transactions on*, vol. 43, no. 1, pp. 438 –442, January 2007.

[51] Y. Honda, T. Nakamura, T. Higaki, and Y. Takeda, "Motor design considerations and test results of an interior permanent magnet synchronous motor for electric vehicles," in *Industry Applications Society Annual Meeting (IAS '97), IEEE*, vol. 1, New Orleans, LA, October 1997, pp. 75 – 82.

[52] S. Wu, L. Tian, and S. Cui, "A comparative study of the interior permanent magnet electrical machine's rotor configurations for a single shaft hybrid electric bus," in *Vehicle Power and Propulsion Conference (VPPC '08), IEEE*, Harbin, China, September 2008, pp. 1 –4.

[53] B. Singh and D. Goyal, "Computer aided design of permanent magnet brushless DC motor for hybrid electric vehicle application," in *Power Electronics, Drives and Energy Systems (PEDES'06), International Conference on*, New Delhi, India, December 2006, pp. 1 –6.

[54] H. A. Products, "Hybrid electric vehicle traction motor," 2004. [Online]. Available: http://www.hap.com/products/Motors/HEVTM/index.html

[55] Z. Dube, "Mitsubishi Lancer Evolution MIEV - all wheel drive using new type of in wheel motor," August 2005. [Online]. Available: http://www.speedsportlife.com/2005/08/24/mitsubishi-lancer-evolution-miev-all-wheel-drive-using-new-type-of-in-wheel-motor/

[56] ZEV, "The performance and value leader in electric vehicles," 2010. [Online]. Available: http://www.zelectricvehicle.com/15.html

[57] F. Magnussen, P. Thelin, and C. Sadarangani, "Performance evaluation of permanent magnet synchronous machines with concentrated and distributed windings including the effect of field-weakening," in *Power Electronics, Machines and Drives (PEMD'04). International Conference on*, vol. 2, Edinburgh, Scotland, March 2004, pp. 679 – 685.

[58] B. Stumberger, A. Hamler, M. Trlep, and M. Jesenik, "Analysis of interior permanent magnet synchronous motor designed for flux weakening operation," *Magnetics, IEEE Transactions on*, vol. 37, no. 5, pp. 3644 – 3647, September 2001.

[59] U. Schaible and B. Szabados, "Dynamic motor parameter identification for high speed flux weakening operation of brushless permanent magnet synchronous machines," *Energy Conversion, IEEE Transactions on*, vol. 14, no. 3, pp. 486 –492, September 1999.

[60] J. Shen, Z. Zhu, and D. Howe, "Sensorless flux-weakening control of permanent-magnet brushless machines using third harmonic back EMF," *Industry Applications, IEEE Transactions on*, vol. 40, no. 6, pp. 1629 – 1636, November 2004.

[61] T.-S. Kwon, S.-K. Sul, L. Alberti, and N. Bianchi, "Design and control of an axial-flux machine for a wide flux-weakening operation region," *Industry Applications, IEEE Transactions on*, vol. 45, no. 4, pp. 1258 – 1266, July 2009.

[62] A. El-Refaie, T. Jahns, P. McCleer, and J. McKeever, "Experimental verification of optimal flux weakening in surface PM machines using concentrated windings," *Industry Applications, IEEE Transactions on*, vol. 42, no. 2, pp. 443 – 453, March 2006.

[63] A. El-Refaie and T. Jahns, "Comparison of synchronous PM machine types for wide constant-power speed range operation," in *Industry Applications Society Annual Meeting (IAS '05), IEEE*, vol. 2, Hong Kong, October 2005, pp. 1015 – 1022.

[64] S. Morimoto, M. Sanada, and Y. Takeda, "Wide-speed operation of interior permanent magnet synchronous motors with high-performance current regulator," *Industry Applications, IEEE Transactions on*, vol. 30, no. 4, pp. 920 – 926, July 1994.

[65] B.-H. Bae, N. Patel, S. Schulz, and S.-K. Sul, "New field weakening technique for high saliency interior permanent magnet motor," in *Industry Applications Society 38th Annual Meeting (IAS'03), IEEE*, vol. 2, Salt Lake City, Utah, October 2003, pp. 898 – 905.

[66] C.-T. Pan and S.-M. Sue, "A linear maximum torque per ampere control for IPMSM drives over full-speed range," *Energy Conversion, IEEE Transactions on*, vol. 20, no. 2, pp. 359 – 366, June 2005.

[67] R. Kirlin, M. Bech, and A. Trzynadlowski, "Analysis of power and power spectral density in PWM inverters with randomized switching frequency," *Industrial Electronics, IEEE Transactions on*, vol. 49, no. 2, pp. 486 – 499, April 2002.

[68] N. Bianchi, M. Dai Prè, L. Alberti, and E. Fornasiero, "Theory and design of fractional-slot PM machines," in *Tutorial course notes 1st ed., IEEE Industry Applications Society*. CLEUP sc, September 2007, pp. 157 – 173.

[69] M. Kamper, A. Rix, D. Wills, and R.-J. Wang, "Formulation, finite-element modeling and winding factors of non-overlap winding permanent magnet machines," in *Electrical Machines (ICEM'08), 18th International Conference on*, Vilamoura, Portugal, September 2008, pp. 1 – 5.

[70] F. Grover, *Inductance calculations, working formulas, and tables*, ser. Self-inductance of circular coils of rectangular cross section. New York: Van Nostrand, 1947.

[71] A. Abdel-Razek, J. Coulomb, M. Feliachi, and S. J.C., "The calculation of electromagnetic torque in saturated electric machines within combined numerical and analytical solutions of the field equations," *Magnetics, IEEE Transactions on*, vol. 17, no. 6, November 1981.

[72] D. Ionel, M. Popescu, M. McGilp, T. Miller, S. Dellinger, and R. Heideman, "Computation of core losses in electrical machines using improved models for laminated steel," *Industry Applications, IEEE Transactions on*, vol. 43, no. 6, pp. 1554 –1564, November 2007.

[73] R.-J. Wang and M. Kamper, "Calculation of eddy current loss in axial field permanent-magnet machine with coreless stator," *Energy Conversion, IEEE Transactions on*, vol. 19, no. 3, pp. 532 – 538, September 2004.

[74] J. Larminie and J. Lowry, *Electric vehicle technology explained*, ser. Electric vehicle modelling. West Sussex, England: Jon Wiley & Sons, 2003.

[75] J. Cros, P. Viarouge, and C. Gelinas, "Design of PM brushless motors using iron-resin composites for automotive applications," in *Industry Applications Society Annual Meeting (IAS '98), IEEE*, vol. 1, St. Louis, MO, October 1998, pp. 5 – 11.

[76] A. Jack, B. Mecrow, P. Dickinson, D. Stephenson, J. Burdess, N. Fawcett, and J. Evans, "Permanent-magnet machines with powdered iron cores and prepressed windings," *Industry Applications, IEEE Transactions on*, vol. 36, no. 4, pp. 1077 – 1084, July 2000.

[77] N. Bianchi and S. Bolognani, "Design techniques for reducing the cogging torque in surface-mounted PM motors," *Industry Applications, IEEE Transactions on*, vol. 38, no. 5, pp. 1259 – 1265, September 2002.

[78] M. Yoneda, M. Shoji, Y. Kim, and H. Dohmeki, "Novel selection of the slot/pole ratio of the PMSM for auxiliary automobile," in *Industry Applications Society 41st Annual Meeting (IAS'06), IEEE*, vol. 1, Tampa, FL, October 2006, pp. 8 –13.

[79] J. Cros and P. Viarouge, "Synthesis of high-performance PM motors with concentrated windings," *Power Engineering Review, IEEE*, vol. 22, no. 4, pp. 74 – 74, April 2002.

[80] Z. Zhu, D. Ishak, D. Howe, and C. Jintao, "Unbalanced magnetic forces in permanent-magnet brushless machines with diametrically asymmetric phase windings," *Industry Applications, IEEE Transactions on*, vol. 43, no. 6, pp. 1544 – 1553, November 2007.

[81] F. Magnussen and H. Lendenmann, "Parasitic effects in PM machines with concentrated windings," *Industry Applications, IEEE Transactions on*, vol. 43, no. 5, pp. 1223 –1232, September 2007.

[82] C. Hwang, M. Wu, and S. Cheng, "Influence of pole and slot combinations on cogging torque in fractional slot PM motors," *Journal of Magnetism and Magnetic Materials*, vol. 304, no. 1, pp. 430 – 432, March 2006.

[83] Y. Perriard, P. Ragot, and M. Markovic, "Brushless DC motor optimization process - choice between standard or straight tooth shape," in *Industry Applications Society 41st Annual Meeting (IAS'06), IEEE*, vol. 4, Tampa, FL, 2006, pp. 1898 –1904.

[84] A. Rix, M. Kamper, and R.-J. Wang, "Torque ripple and flux density variation due to stator slot openning of a concentrated coil permanent magnet machine," in *Southern African Universities Power Engineering Conference (SAUPEC)*, Cape Town, South Africa, 2007.

[85] ——, "Design and performance evaluation of concentrated coil permanent magnet machines for in-wheel drives," in *Electric Machines & Drives Conference (IEMDC '07), IEEE International*, vol. 1, Antalya, Turkey, May 2007, pp. 770 – 775.

[86] M. Cistelecan and M. Popescu, "Study of the number of slots/pole combinations for low speed permanent magnet synchronous generators," in *Electric Machines Drives Conference (IEMDC '07), IEEE International*, vol. 2, Antalya, Turkey, May 2007, pp. 1616 – 1620.

[87] S. Williamson and J. Smith, "The application of minimisation algorithms in electrical engineering," *Physical Science, Measurement and Instrumentation, Management and Education - Reviews, IEE Proceedings A*, vol. 127, no. 8, pp. 528 –530, November 1980.

[88] M. Kamper, "Design optimisation of cageless flux barier rotor reluctance synchronous machine," Ph.D. dissertation, University of Stellenbosch, South Africa, December 1996.

[89] M. Powell, "An efficient method for finding the minimum of a function of several variables without calculating derivatives," *Computer Journal*, vol. 7, pp. 155 –162, 1964.

[90] H. Jussila, P. Salminen, M. Niemela, and J. Pyrhonen, "Guidelines for designing concentrated winding fractional slot permanent magnet machines," in *Power Engineering, Energy and Electrical Drives, International Conference on*, Setubal, Portugal, April 2007, pp. 191 – 194.

[91] A. Vagati, G. Pellegrino, and P. Guglielmi, "Comparison between SPM and IPM motor drives for EV application," in *Electrical Machines (ICEM'10), 19th International Conference on*, Rome , Italy, September 2010, pp. 1 – 6.

[92] H. De Kock, A. Rix, and M. Kamper, "Optimal torque control of interior permanent magnet synchronous machines in the full speed range," in *Electrical Machines (ICEM'08), 18th International Conference on*, Vilamoura, Portugal, Spetember 2008, pp. 1 – 6.

[93] M. Rahman, L. Zhong, and K. W. Lim, "A direct torque-controlled interior permanent magnet synchronous motor drive incorporating field weakening," *Industry Applications, IEEE Transactions on*, vol. 34, no. 6, pp. 1246 – 1253, November 1998.

[94] H.-D. Lee, S.-J. Kang, and S.-K. Sul, "Efficiency-optimized direct torque control of synchronous reluctance motor using feedback linearization," *Industrial Electronics, IEEE Transactions on*, vol. 46, no. 1, pp. 192 – 198, February 1999.

[95] L. Zhong, M. Rahman, W. Hu, K. Lim, and M. Rahman, "A direct torque controller for permanent magnet synchronous motor drives," *Energy Conversion, IEEE Transactions on*, vol. 14, no. 3, pp. 637 –642, September 1999.

[96] M. Haque, L. Zhong, and M. Rahman, "A sensorless initial rotor position estimation scheme for a direct torque controlled interior permanent magnet synchronous motor drive," *Power Electronics, IEEE Transactions on*, vol. 18, no. 6, pp. 1376 – 1383, November 2003.

[97] L. Tang, L. Zhong, M. Rahman, and Y. Hu, "A novel direct torque controlled interior permanent magnet synchronous machine drive with low ripple in flux and torque and fixed switching frequency," *Power Electronics, IEEE Transactions on*, vol. 19, no. 2, pp. 346 – 354, March 2004.

[98] M. Pacas and J. Weber, "Predictive direct torque control for the PM synchronous machine," *Industrial Electronics, IEEE Transactions on*, vol. 52, no. 5, pp. 1350 – 1356, October 2005.

[99] K. Gulez, A. Adam, and H. Pastaci, "A novel direct torque control algorithm for IPMSM with minimum harmonics and torque ripples," *Mechatronics, IEEE/ASME Transactions on*, vol. 12, no. 2, pp. 223 – 227, April 2007.

[100] Z. Xu and M. Rahman, "Direct torque and flux regulation of an IPM synchronous motor drive using variable structure control approach," *Power Electronics, IEEE Transactions on*, vol. 22, no. 6, pp. 2487 –2498, November 2007.

[101] S.-K. Chung, H.-S. Kim, C.-G. Kim, and M.-J. Youn, "A new instantaneous torque control of PM synchronous motor for high-performance direct-drive applications," *Power Electronics, IEEE Transactions on*, vol. 13, no. 3, pp. 388 – 400, May 1998.

[102] F.-J. Lin and R.-J. Wai, "A hybrid computed torque controller using fuzzy neural network for motor-quick-return servo mechanism," *Mechatronics, IEEE/ASME Transactions on*, vol. 6, no. 1, pp. 75 – 89, March 2001.

[103] R. Monajemy and R. Krishnan, "Control and dynamics of constant-power-loss-based operation of permanent-magnet synchronous motor drive system," *Industrial Electronics, IEEE Transactions on*, vol. 48, no. 4, pp. 839 – 844, August 2001.

[104] Y.-R. Mohamed, "A newly designed instantaneous-torque control of direct-drive PMSM servo actuator with improved torque estimation and control characteristics," *Industrial Electronics, IEEE Transactions on*, vol. 54, no. 5, pp. 2864 – 2873, October 2007.

[105] R. Morales-Caporal and M. Pacas, "A predictive torque control for the synchronous reluctance machine taking into account the magnetic cross saturation," *Industrial Electronics, IEEE Transactions on*, vol. 54, no. 2, pp. 1161 – 1167, April 2007.

[106] A. Consoli, G. Scarcella, G. Scelba, S. Sindoni, and A. Testa, "Steady-state and transient analysis of maximum torque per ampere control for IPMSMs," in *Industry Applications Society Annual Meeting (IAS '08), IEEE*, Edmonton, Alta, October 2008.

[107] H. De Kock and M. Kamper, "Dynamic control of the permanent magnet-assisted reluctance synchronous machine," *Electric Power Applications, IET*, vol. 1, no. 2, pp. 153 – 160, March 2007.